

Jostein Gjevre

# Power Systems for Deep Sea Mining Applications, With Focus on Stability

Master's thesis in Energy and Environmental Engineering  
Supervisor: Elisabetta Tedeschi  
June 2019

**NTNU**  
Norwegian University of Science and Technology  
Faculty of Information Technology and Electrical  
Engineering  
Department of Electric Power Engineering



Norwegian University of  
Science and Technology



Jostein Gjevre

# Power Systems for Deep Sea Mining Applications, With Focus on Stability

Master's thesis in Energy and Environmental Engineering  
Supervisor: Elisabetta Tedeschi  
June 2019

Norwegian University of Science and Technology  
Faculty of Information Technology and Electrical Engineering  
Department of Electric Power Engineering

 **NTNU**  
Norwegian University of  
Science and Technology



---

# Abstract

Due to the ever-increasing demand for minerals and the depletion of terrestrial mines, the eyes of the mining industry has begun to look towards the great depths of the ocean. The deep sea is expected to hide sites with massive deposits rich in rare minerals such as gold, silver, copper and cobalt. Some of the richest locations have been found in proximity to highly active volcanic and tectonic zones. Samples taken from these locations have indicated exceptionally high ore grades, exceeding what is found in most terrestrial mines. Along Mohn's ridge between Svalbard and Jan Mayen, numerous seafloor massive sulphur (SMS) deposits, related to active and extinct hydro-thermal vents, have been discovered. Among the discovered sites is Loki's Castle, at a depth of 2400 meters, recognized as one of the most promising locations for the extraction of minerals. At this point, there are few production systems developed for deep sea mining (DSM) applications. Hence, it is of great interest for the development of future systems to identify operational and design related issues for this kind of systems.

This thesis has through studies of existing concepts and research on the field of deep sea mining, developed a model for the electrical power system of a DSM production system. The model is developed with the intention of investigating the power system stability issues related to such an isolated system with converter-fed loads. A production system developed by the company Nautilus Minerals has formed the base of the study. Based on the literature research a DC distributed system with a centralized submersed power hub is proposed. The system is designed for a depth of 3500 meters, with the intention of operating in sites located in waters within Norwegian jurisdiction. A time-domain model and a linearized model for small signal analysis have been developed in the MATLAB/SIMULINK environment. The developed model configuration is a point-to-point DC-link supplying a variable speed drive connected to a large induction machine. The two models are used for systematic analyses of relevant test cases, with the intention of investigating the impact of the converter controllers and to reveal the stability limits of the system under different operating conditions. The results have shown that the strength of the power system of the supply vessel is critical for the stability limits of the system. When the on-board system has a short circuit ratio of 2, the power transfer capability has been identified to deteriorate to an extent where the system is incapable of satisfying the power requirement of the sub-sea system. Low-frequency oscillations have been detected related to the instability events, indicating a system that is easily excited even at nominal conditions.



---

# Sammendrag

Grunnet den stadig økende etterspørselen etter mineraler og den reduserte malmkvaliteten i landbaserte gruver, har gruveindustrien nå begynt å se mot mulighetene som skjuler seg på bunnen av de store havdyp. Kartleggingen av havbunnen har til nå vært begrenset og det forventes at det finnes områder med betydelige forekomster av mineraler med høyt innhold av sjeldne metaller som gull, sølv, kobber og kobolt. Noen av de mest mineralrike stedene har blitt funnet i nærheten av vulkansk aktive og tektoniske soner. Prøver tatt fra disse lokasjonene har indikert eksepsjonelt høy malmkvalitet, der mange overstiger det som er funnet i majoriteten av landbaserte gruver. Langs Atlanterhavsryggen mellom Jan Mayen og Svalbard er det oppdaget store mineralforekomster relatert til såkalte hydro-termiske skorsteiner. Blant de oppdagede lokasjonene har Lokeslottet, på 2400 meter dyp, blitt anerkjent som en av de mest lovende stedene for framtidig mineralutvinning. Per nå er det få produksjonssystemer som er utviklet for undersjøisk gruvedrift. Det er derfor av stor interesse for utviklingen av fremtidige systemer at operasjonelle og designrelaterte problemer for denne typen systemer blir identifisert.

Denne oppgaven har, gjennom studier av eksisterende konsepter og forskning innen feltet undersjøisk gruvedrift, foreslått en modell for det elektriske kraftsystemet knyttet til et undersjøisk gruvesystem. Modellen er utviklet med den hensikt å kunne undersøke stabilitetsproblemer knyttet til et isolert kraftsystem basert på kraftomformerteknologi. Produksjonssystemet utviklet av selskapet Nautilus Minerals har dannet grunnlaget for modellen. Basert på tilgjengelig forskning har et DC-distribuert system med en enkelt kraftforsyningskabel blitt foreslått. Systemet er designet for en dybde på 3500 meter, med sikte på å operere i farvann innenfor norsk jurisdiksjon. To separate modeller har blitt utviklet i MATLAB / SIMULINK, en modell i tidsdomenet og en linearisert modell for "small-signal" analyse. For å redusere kompleksiteten er systemet modellert som en "point-to-point" DC-link knyttet til en kraftinverterer som forsyner en stor induksjonsmaskin. De to modellene brukes til å utføre systematiske sanalyser for å få oversikt over hvordan tuningen av regulatorne påvirker systemets stabilitet og hvordan systemets stabilitetsgrenser påvirkes under forskjellige driftsforhold. Studien har vist at styrken til kraftforsyningen på forsyningsskipet har en sterk påvirkning på stabiliteten til systemet. Ved en kortslutningsytelsesrate på 2 har det blitt observert at overføringsevnen til systemet reduseres betydelig, til en grad der systemet ikke lenger er i stand til å dekke kraftbehovet til produksjonssystemet. Det har også blitt observert en rekke lavfrekvente svingninger under ustabile forhold, noe som indikerer et følsomt system, som lett blir eksitert selv ved nominell drift.





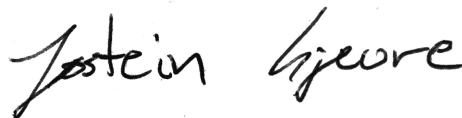
---

# Preface

This Master thesis is the concluding project of my Masters Degree at the Department of Electric Power Engineering at the Norwegian University of Science and Technology. The work has been conducted entirely during the spring semester in 2019 at NTNU in Trondheim, Norway.

The Master thesis is built on a specialization project written in the fall of 2018. The work conducted in this project was focused as a literature review on deep sea mining production concepts and technical requirement for this kind of systems. The writing of this thesis has been found both interesting and rewarding due to the many different fields of study it touches upon. Yet, due to the introduction of many new concepts and the complexity of dealing with the design aspects of an entire production system, the task has also been very challenging and time demanding. The major time consumer has however been the tuning and debugging of the time-domain model in SIMULINK, which has made this thesis seemingly hopeless at times.

I would like to express my gratitude to my main supervisor Prof. Elisabetta Tedeschi for her support and guidance during the development of this project. I would also like to thank Atousa Elahidoost for helping me with the linearized model, Santiago Sanchez Acevedo for supporting me with the development and debugging of the SIMULINK model and Raghendra Tiwari for being very helpful with the modelling of the induction machine and motor drive. Finally, I would also like to thank Lars Øyvind Moen at Nexans and ABB for respectively providing realistic data for the dc-link and the induction machine.



Trondheim, June 11 2019

Jostein Gjevre



# Table of Contents

<b>Abstract</b>	<b>i</b>
<b>Sammendrag</b>	<b>iii</b>
<b>Preface</b>	<b>v</b>
<b>Table of Contents</b>	<b>vii</b>
<b>List of Tables</b>	<b>x</b>
<b>List of Figures</b>	<b>xii</b>
<b>Nomenclature</b>	<b>xv</b>
<b>1 Introduction</b>	<b>1</b>
1.1 Objective and contribution . . . . .	1
1.2 Method . . . . .	2
1.3 Scope of the work and its limitation . . . . .	2
1.4 Structure of report . . . . .	3
<b>2 Background</b>	<b>4</b>
2.1 Motivation for deep-sea mining . . . . .	4
2.2 Environmental Concern . . . . .	6
2.3 Brief introduction to the development of SMS mining - Nautilus Minerals . . . . .	7
2.4 Deep sea mining within Norwegian jurisdiction . . . . .	7
<b>3 DSM production system</b>	<b>9</b>
3.1 The Nautilus Mineral's system . . . . .	9
3.1.1 Seabed system (SS) . . . . .	10
3.2 Underwater transportation system (UTS) . . . . .	12
3.2.1 Sub-sea Slurry Lift Pump (SSLP) . . . . .	12
3.3 Topside system . . . . .	12

---

<b>4</b>	<b>Power Systems for DSM</b>	<b>15</b>
4.1	Onboard power system . . . . .	15
4.2	Sub-sea power system . . . . .	16
4.2.1	Power system topologies . . . . .	16
4.3	Onboard loads . . . . .	21
4.3.1	SSLP . . . . .	21
4.4	Sub-sea loads . . . . .	21
4.5	Power requirement for operation in Norwegian waters . . . . .	22
4.6	System for further studies . . . . .	24
4.7	Selection of system ratings and parameters . . . . .	25
4.7.1	Onboard system . . . . .	25
4.7.2	Sizing of sub-sea supply cable . . . . .	25
4.8	Selection of asynchronous machine . . . . .	28
4.9	Simplification of sub-sea system . . . . .	28
<b>5</b>	<b>Stability definitions and analysis tools</b>	<b>30</b>
5.1	Conventional stability definitions . . . . .	30
5.1.1	Voltage stability . . . . .	31
5.2	Stability analysis tools . . . . .	32
5.2.1	Eigenvalue analysis . . . . .	33
5.3	Power system strength - Short circuit ratio . . . . .	36
5.3.1	X/R ratio . . . . .	37
5.4	Resonance frequency . . . . .	37
<b>6</b>	<b>System modelling</b>	<b>39</b>
6.1	Power system layout . . . . .	39
6.2	Average-value model . . . . .	39
6.3	Dynamics of topside system . . . . .	41
6.3.1	Mathematical modelling of TS . . . . .	41
6.4	Control of topside converter . . . . .	43
6.4.1	Proportional Integral Controller . . . . .	43
6.4.2	Phase-locked loop (PLL) . . . . .	44
6.4.3	Inner controller . . . . .	45
6.4.4	Outer controller . . . . .	48
6.5	Squirrel cage machine . . . . .	49
6.5.1	Power balance . . . . .	51
6.6	Motor drive - VSD . . . . .	51
6.6.1	Inner loop . . . . .	51

---

---

6.6.2	Outer loop . . . . .	53
6.7	Dynamics of DC link . . . . .	53
6.8	MATLAB/SIMULINK models . . . . .	54
<b>7</b>	<b>Stability analysis of DSM power system</b>	<b>55</b>
7.1	Preliminary study of the tuning of the system models . . . . .	55
7.2	Sensitivity analysis of the gain parameters . . . . .	61
7.2.1	Gains of VSC current controller . . . . .	61
7.2.2	Gains of DC voltage controller . . . . .	62
7.2.3	Gains of VSD current controller . . . . .	64
7.2.4	Speed controller . . . . .	65
7.2.5	Observations . . . . .	66
7.3	Analysis of the cable resonance . . . . .	68
7.4	Finite strength of onboard system . . . . .	69
7.4.1	SCR with an X/R ratio of 1 . . . . .	69
7.4.2	SCR with an X/R ratio of 0.2 . . . . .	70
7.4.3	SCR with an X/R ratio of 5 . . . . .	72
7.4.4	Observations . . . . .	73
7.5	System stability with PLL dynamics . . . . .	74
7.6	Study of maximum power transfer capability . . . . .	76
7.6.1	Observations . . . . .	79
7.7	Discussion . . . . .	80
<b>8</b>	<b>Conclusion and further work</b>	<b>82</b>
8.1	Concluding remarks . . . . .	82
8.2	Future work . . . . .	84
	<b>Bibliography</b>	<b>85</b>
	<b>Appendix</b>	<b>91</b>
A	Per-unit calculations . . . . .	91
B	ABC to dq transformation . . . . .	92
C	Dq0-transformation of VSC system equations . . . . .	95
D	Participation factor tables . . . . .	99
E	Time-domain simulations - Stable conditions . . . . .	109
F	Calculation for cable selection . . . . .	110
G	Data-sheet of power cable (provided by NEXANS) . . . . .	111
H	Data-sheet of induction machine (provided by ABB) . . . . .	114
I	Modelling specific notes . . . . .	115

---

# List of Tables

2.1	Expected stock increase for low-carbon technologies from year 2015 to year 2060 [8] . . . . .	5
4.1	Installed capacity for a design depth of 2500 meters (equal to the Solwara project)	22
4.2	Estimated values of installed capacity for a design depth of 3500 meters (based on estimates from Williksen [22]) . . . . .	23
4.3	Max. contemporary power of the sub-sea system [24] . . . . .	25
4.4	Rated values and electrical parameters for sub-sea supply cable . . . . .	27
4.5	Rated values and electrical parameters for squirrel cage machine provided by ABB . . . . .	29
7.1	Initial gain parameters obtained from tuning principles . . . . .	55
7.2	Comparison of the gain parameters of the well damped system and the time domain model . . . . .	59
D1	Participation factors of tuning principle obtained gains . . . . .	99
D2	Participation factors of moving poles at the extremities of the proportional gain $Kp_{c,c}$ . . . . .	100
D3	Participation factors of moving poles at the extremities of the proportional gain $Ki_{c,c}$ . . . . .	101
D4	Participation factors of moving poles at the extremities of the proportional gain $Kp_v$ . . . . .	102
D5	Participation factors of moving poles at the extremities of the integral gain $Ki_v$ .	102
D6	Participation factors of moving poles at the extremities of the proportional gain $Kp_{c,m}$ . . . . .	103
D7	Participation factors of moving poles at the extremities of the integral gain $Ki_{c,m}$	103
D8	Participation factors of moving poles at the extremities of the proportional gain $Kp_{sp}$ . . . . .	104
D9	Participation factors of moving poles at the extremities of the integral gain $Ki_{sp}$	104
D10	Participation factors of the moving poles at SCR with a X/R ratio of 1 . . . . .	105

---

D11	Participation factors of the moving poles at SCR with a X/R ratio of 0.2 . . . .	106
D12	Participation factors of moving poles at SCR with a X/R ratio of 5 . . . . .	107
D13	Participation factors corresponding to bandwidth $a_{pll} = 12$ . . . . .	108
I1	Parameters of additional components . . . . .	115
I2	Operating point of linearized model . . . . .	116

# List of Figures

2.1	Topographic view on the distribution of marine mineral deposits (modified from [15]) . . . . .	6
2.2	Location of Loki’s Castle . . . . .	8
3.1	Illustration of the production system developed by Nautilus Minerals (modified from [13]) . . . . .	10
3.2	Auxiliary miner [23] . . . . .	11
3.3	Bulk miner [23] . . . . .	11
3.4	Collection machine [23] . . . . .	11
3.5	3D illustration of the SSLP . . . . .	12
3.6	a) PSV with identified dewatering plant and accommodation block b) PSV and bulk barge (Nautilus Minerals) <sup>1</sup> . . . . .	14
4.1	VSDs installed topside . . . . .	17
4.2	Individual umbilicals for the respective SPTs with VSDs installed sub-sea . . . . .	17
4.3	Single SPH supplying all sub-sea loads . . . . .	18
4.4	Advantage of a static electric field [27] . . . . .	19
4.5	Behavior of a CPL [30] . . . . .	20
4.6	Proposed DSM power system for a design depths of 3500 meters . . . . .	24
4.7	Cross-section of three core sub-sea power cable [27] . . . . .	27
5.1	Pole placement influence on signal response [46] . . . . .	34
5.2	Pole placement influence on signal response [46] . . . . .	34
5.3	Pole placement influence on maximum overshoot [46] . . . . .	35
5.4	Acceptable pole placement region [46] . . . . .	35
5.5	Types of resonance circuits . . . . .	38
5.6	$\Pi$ model circuit diagram . . . . .	38
6.1	Schematic overview of the DSM power system) . . . . .	40
6.2	Conceptual scheme of an average-value model . . . . .	40
6.3	One line-diagram of onboard power system . . . . .	41



---

6.4	Block diagram of the control structure for the onboard VSC . . . . .	43
6.5	Block diagram of the control structure of the PLL . . . . .	44
6.6	Relationship between the magnitude of the $q$ component and the phase error . .	45
6.7	Block diagram of current controller . . . . .	46
6.8	Block diagram of simplified VCC structure . . . . .	46
6.9	Block diagram of DC voltage controller . . . . .	49
6.10	Block diagram of VSD . . . . .	52
6.11	Block diagram of current controller in the motor drive . . . . .	52
6.12	Block diagram of speed controller in the motor drive . . . . .	53
6.13	$\Pi$ equivalent of the dc cable . . . . .	54
7.1	Poles of system with gain parameters based on the tuning principles . . . . .	56
7.2	Poles of system with adjusted gains in the outer loops . . . . .	57
7.3	Poles of well damped system . . . . .	57
7.4	3-phase voltages of onboard grid and converter terminals . . . . .	58
7.5	Time-domain model - Stable conditions . . . . .	58
7.6	Pole placement with gains from time-domain model . . . . .	59
7.7	Pole trajectories - Current controller VSC . . . . .	61
7.8	Pole trajectories - DC voltage controller VSC . . . . .	62
7.9	DC voltage at a $Kp_v$ of 15 . . . . .	63
7.10	DC voltage at a $Ki_v$ of 900 . . . . .	63
7.11	Pole trajectories - Current controller VSD . . . . .	64
7.12	Pole trajectories - Speed controller VSD . . . . .	65
7.13	Voltage signal of DC-link with at a $Kp_{sp}$ of 35 . . . . .	66
7.14	$Ki_{sp}$ of 70 . . . . .	66
7.15	Impedance-frequency plot of the DC link . . . . .	68
7.16	Pole trajectories for change in SCR between 47 and 0.47 with an X/R ratio of 1	69
7.17	Voltage signals with a SCR of 3 . . . . .	70
7.18	Initial voltage oscillations with a SCR of 2.8 . . . . .	70
7.19	Pole trajectories for change in SCR between 40 and 1 at with an X/R ratio of 0.2	71
7.20	Voltage signals with a SCR of 2 . . . . .	71
7.21	Voltage signals with an SCR of 2 . . . . .	71
7.22	Pole trajectories for change in SCR between 50 and 0.1 at with an X/R ratio of 5	72
7.23	SCR 4.7 - DC voltage instability event . . . . .	73
7.24	SCR 4.7 - Voltage signal oscillations of 590Hz . . . . .	73
7.25	Pole plot of system with bandwidth $a_{PLL}$ ranging from 0.04 to 36 at a SCR of 2.5	74
7.26	Pole trajectories of $\Lambda_{pll}$ at different SCR . . . . .	75
7.27	Maximum power transfer capability of DC-link at a SCR of 10 . . . . .	76

---

---

7.28	Maximum power transfer capability of DC-link at a SCR of 5 . . . . .	77
7.29	Maximum power transfer capability of DC-link at a SCR of 2.5 . . . . .	77
7.31	Power signal excluding dynamics of DC-link . . . . .	78
7.33	Power signal excluding dynamics of drive and induction machine . . . . .	78
7.35	Power signal excluding dynamics of the onboard system and the VSC . . . . .	79
B1	Transformation of axes for vector control . . . . .	92
C1	Circuit diagram of a 2-level VSC . . . . .	95

---

---

# Nomenclature

## Abbreviations

*AM* Auxiliary machine

*AMOR* Arctic Mid-Ocean Ridge

*AVM* Average-value Model

*BM* Bulk machine

*CM* Collection machine

*CPL* Constant power load

*DSM* Deep Sea Mining

*EEZ* Economically exclusive zone

*HVDC* High Voltage Direct Current

*LARS* Launch and Recovery System

*PCC* Point of Common Coupling

*PLL* Phase-locked Loop

*PMN* Poly-metallic Manganese Nodules

*PNG* Papua New Guinea

*PSV* Production support vessel

*PV* Photovoltaics

*RALS* Riser and Lifting System

*RMS* Rounds per minute

*ROV* Proportional Integral Controller

---

*ROV* Remotely Operated Underwater Vehicle  
*RRF* Rotating reference frame  
*SCR* Short Circuit Ratio  
*SMS* Seafloor Massive Sulfides  
*SPH* Submersed Power Hub  
*SRF* Synchronous Reference Frame  
*SSLP* Sub-sea Slurry Lift Pump  
*TS* Topside System  
*UTS* Underwater Transportation System  
*VCC* Vector current control  
*VSC* Voltage Source Converter  
*VSD* Variable Speed Drive



# Chapter 1

## Introduction

### 1.1 Objective and contribution

This thesis aims to investigate different stability aspects of a power system for deep sea mining (DSM) applications in Norwegian territories. An introduction to DSM will be given, where the production system is explained and the design aspects of the power system will be discussed. The introductory discussion will be used to propose a power system topology for the development of an analytic model. A time-domain simulation model and a small signal linearized model will be developed for the purpose of stability analysis. The developed models will be used to conduct a stability analysis of a power system designed to operate in the Norwegian Sea. The objective of the stability analysis is to investigate how system components influence the system stability and to identify stability limits of the system under different operating conditions.

To the best of the author's knowledge, the following are the main contribution of this thesis:

- A review and consolidation of technical knowledge on the design aspects of power systems for DSM applications.
- A design proposal of a DSM power system for application at promising locations in the Norwegian Sea.
- The development of a SIMULINK time domain model and a linearized model of a DSM power system.
- The identification of stability related issues in a weak power system with converter fed loads.

## 1.2 Method

This thesis considers a mining site at depths similar to Loki's Castle located at Mohn's ridge in the Norwegian Sea. The production system applied is inspired by the system developed by the company Nautilus Minerals for the Solwara 1 project in the Bismarck Sea, outside Papua New Guinea. In order to perform a stability analysis of the power system related to the DSM production system, extensive literature research has been conducted. The research forms the base of the proposed power system topology, designed for an operational depth of 3500 meters. The proposed system is mathematically modelled as a point-to-point DC-link with an inverter fed sub-sea load, representing the sub-sea lifting pump. From the mathematical model, a time domain model and a linearized model are developed in the MATLAB/SIMULINK environment. The models are ultimately used to conduct a series of stability tests of the power system.

## 1.3 Scope of the work and its limitation

The scope of this thesis will be to investigate the power system stability aspects of a weak power system with converter fed loads, designed to supply a DSM production system in Norwegian waters. Relevant concepts and theory are to be discussed, yet the fundamental components of the power system will not be elaborated in detail as it is expected that the reader has a general understanding of power system components. The scope only covers the production system developed by the company Nautilus Minerals.

The scope of the modelling part will primarily comprise the power system supplying the sub-sea loads, meaning the model will not focus on the design of the system onboard the supply vessel. The sub-sea power system will be modelled as precisely as necessary in order to capture the dynamics of the system.

The scope of the stability analysis will be to determine the destabilizing effect of the controller gains as well as the strength of the onboard system and to identify the stability limitations during different operational conditions. The analysis is exclusively limited to the production situation of the system, hence the start-up performance of the system is not considered. The mechanical performance of the sub-sea loads are also considered to be beyond the scope of this study.

The geological and the economic aspects of DSM will only be briefly mentioned.



## 1.4 Structure of report

- **Chapter 2** gives a general introduction to the concept of DSM, including the drivers for a DSM industry, a brief historical overview, the associated environmental concerns and the possibilities for a DSM industry in Norwegian waters.
- **Chapter 3** elaborates in detail the production system developed by the company Nautilus Minerals.
- **Chapter 4** describes the requirements and discusses the design aspects of the DSM power system. The chapter also proposes a power system topology and discusses the selection of system ratings and parameters.
- **Chapter 5** presents the definitions of power system stability and describes the most relevant theory related to the stability analysis.
- **Chapter 6** describes the layout and provides the mathematical modelling of the dynamics of the proposed system, as well as the tuning of the controllers of the converters.
- **Chapter 7** includes the results and the discussion of the stability analysis.
- **Chapter 8** presents the concluding remarks and proposed future work.

# Chapter 2

## Background

This chapter aims to clarify the motivation behind the development of a deep sea mining (DSM) industry and to point out some of the concerns associated with this development. Additionally, the history of the leading DSM company is presented and the potential for DSM activity in Norwegian waters is discussed. The content of this chapter is based on the preliminary work presented in [1].

### 2.1 Motivation for deep-sea mining

The global economy is growing at a rapid pace and is projected to more than double by the year 2050 [2, 3]. Additionally, the increase in global population, together with a general improvement of the global standard of living, is expected to generate a heavy demand growth for natural resources [4]. Particularly for minerals and metals, due to their indispensable role as commodities in most high-tech and low-carbon technologies. Alongside the rise in the global standard of living, climate change is increasingly recognized as a severe global problem. Over the last decade, there has been a remarkable development of sustainable infrastructure and technologies, which is predicted to increase significantly in numbers also in the foreseeable future. A prediction of the stock increase towards the year 2060 is presented in table 2.1. These technologies are however very mineral and metal-intensive, e.g in wind turbine manufacturing the demand for copper is between 1100-3000 kg/MW [5] and an electric car could harbour 10–20kg of cobalt [6]. Hence a transition to a low carbon society will potentially have a significant impact on metal and mineral markets. The global demand for minerals, such as copper, lithium, nickel and cobalt is estimated to ten or hundredfold within this century [7].

In the past decades, there has already been a substantial increase in the demand for minerals, primarily as a result of the impressive development in many of the Asian countries, where China has been the predominant contributor, standing for around half of the global demand [9].

**Table 2.1:** Expected stock increase for low-carbon technologies from year 2015 to year 2060 [8]

	Stock in society (2015) in millions	Stock in society (2060) in millions	Stock increase
Personal vehicles: Battery electric	1.5	1300	87000%
Personal vehicles: Hybrid, plug-in hybrid and fuel cells	14	710	5000%
Electric bikes	460	1600	300%
Buses: Battery el., hybrid, plug-in hybrid and fuel cell	0	31	N/A
Cars: Battery el., hybrid, plug in hybrid and fuel cell	0	130	N/A
Wind power (GW)	430	4200	1000%
Solar photovoltaic (GW)	220	6700	3000%
Solar thermal (GW)	21	1300	6000%

In order to meet the demand, the extraction of minerals has to increase correspondingly. As the extraction intensifies, the ore grades tend to gradually decline, which results in an increased production of waste rock and more extensive open-pit mining [10]. Consequently causing the energy consumption of the activity to increase with a higher rate than the production rate [11]. As the production gets more energy intensive the cost of production rises, which again affects the prices in the mineral market. The depletion of terrestrial mines and the increase in demand encourage exploration in deeper and more remote locations, where the deep sea floor is recognized to be among the most promising frontiers for discovering large scale deposits. However, no commercial operation in the deep sea has been commissioned yet.

Since the majority of the ocean floor is mapped to a maximum resolution of 5km [12], the deep sea is expected to hide locations with massive mineral deposits. Promising locations have been discovered in proximity to areas with high tectonic and volcanic activity. Samples obtained from these sites have indicated deposits of exceptionally high ore grades, exceeding the ore gradients found in most terrestrial deposits [13]. There are mainly three categories of minerals that are found to be of commercial interest (figure 2.1).

- **Cobalt-rich ferromanganese crusts** are normally located around seamounts, ridges and other sites where sea currents have cleaned the ocean floor of sediments. Typically, they are found at depths of 400-4000m. The crust largely consists of cobalt (Co). However, other rare minerals such as vanadium (V), molybdenum (Mo), platinum (Pt) and tellurium (Te) also occurs [14].
- **Poly-metallic Manganese nodules (PMN)** occur in most oceans of the world. The nodules are small rocks (typically 5-10 cm in diameter), which can be found at almost any depth. However, the highest concentration occurs at abyssal plains at depths of 4000-6000m. The nodules typically consist of manganese (Mn), copper (Cu), nickel (Ni) and cobalt (Co) [13].

- **Seafloor massive sulfides (SMS)** originate from hydrothermal vents in tectonically active or volcanic zones, at depths varying from 1500-5000m. The characteristic metals are zinc (Zn), lead (Pb), copper (Cu), gold (Au) and silver (Ag) [13]. Due to its presence in the Norwegian waters, extraction of SMS deposits forms the basis of this thesis.

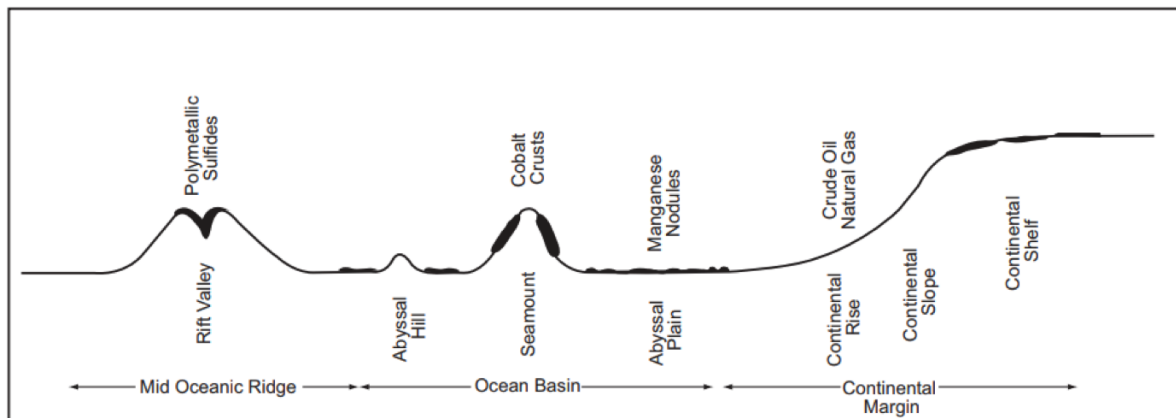


**Figure 2.1:** Topographic view on the distribution of marine mineral deposits (modified from [15])

## 2.2 Environmental Concern

Alongside the commercial interest for deep-sea mining, there is a concern among researchers regarding the substantial environmental risks related to such an activity, both above and below sea level. A great number of the sites identified for deep-sea mining are home to fragile and unique ecosystems, with an extraordinary diverse form of life. So far there is a very limited amount of research on deep-sea ecosystems, and even less on how they support other ecosystems [16]. Some sea-bed disturbance studies have been conducted to indicate the environmental impacts of mining activities. A comprehensive research program, known as the MIDAS program was completed in 2016, after 3 years of investigation. The study showed that the life forms were unable to fully recover, even several decades after the disturbance [17]. According to [18], the recolonization time may vary from a couple of decades to centuries, due to the slow recovery rate of deep-sea life forms. For the most unique sites, the impact might even be irreversible. The mining operation may also be in conflict with the fishing industry and firms seeking marine genetic resources for pharmaceutical purposes [18]. The lack of baseline knowledge makes it hard to predict the long term effects of deep-sea mining. Thus, a precautionary approach is needed to preserve environmental assets and to avoid severe or irreversible consequences.

## **2.3 Brief introduction to the development of SMS mining - Nautilus Minerals**

In the mid-1980's hydrothermal vents were discovered at the convergent plate margins <sup>1</sup> in the Bismarck Sea outside Papua New Guinea (PNG). The findings initiated numerous research projects, and in November 1997 the first commercial licenses for exploration of SMS deposits was granted to the Nautilus Minerals Corporation [19]. The company conducted a comprehensive research program in the following years. The program revealed in total seventeen SMS deposits as well as two sulphate deposits, which constitute what is known as the Solwara project. In January 2011, Nautilus Minerals was granted a mining lease for the Solwara 1 deposit, which is located at 1600 meters depth about 30 km from the mainland of PNG. Since then the company has been working towards the commissioning a fully operating production system. The project is scheduled to be in commercial operation before the end of the third quarter (Q3) of 2019 [20]. Except for Nautilus Minerals, the Diamond Fields International is the only company who has been granted permission for commercialized DSM operation of SMS deposits. They intend to exploit the Atlantis II basin in the Red Sea, which is acknowledged as the biggest identified SMS deposit in the world. However, Nautilus Minerals is by far the company closest to commercial operation [17].

## **2.4 Deep sea mining within Norwegian jurisdiction**

The category of minerals that is of most relevance for mining in Norwegian waters is SMS deposits. Exploration along the Arctic Mid-Ocean Ridge (AMOR) has revealed numerous locations with hydrothermal vents. A number of these sites are located on Mohn's ridge between Svalbard and Jan Mayen, where many are located within the Norwegian economically exclusive zone (EEZ). One of the most promising sites is known as Loki's Castle (figure 2.2), with active hydrothermal vents located at a water depth of 2400 meters. The site has a 200 meter wide and 20-30 meter thick SMS deposit, estimated to contain 56 600 t of zinc, 51 100 t of copper, 86 t of silver and 1.72 t of gold. [13].

Despite major economic and technological uncertainties, the potential for deep-sea mining operation within Norwegian waters has been recognized as promising and has resulted in growing research activity. So far there has mainly been purely conceptualized research conducted on DSM operation at selected locations (Loki's Castle). However, expeditions have also been conducted. Vessels equipped with ROVs <sup>2</sup> have been taking geological and biological samples in

---

<sup>1</sup>Collision zone between an oceanic and a continental tectonic plate

<sup>2</sup>Remotely Operated Underwater Vehicle

order to assess the economic and environmental aspects of DSM activity in Norwegian waters. NTNU is an important contributor to this field of study and aims to be among the leading research institutions on DSM. Large companies, such as Equinor, Kongsberg Maritime and TechnipFMC are also involved in the research and development towards DSM operation within Norwegian jurisdiction [21].



**Figure 2.2:** Location of Loki's Castle

# Chapter 3

## DSM production system

In this chapter, the different components of the production system developed by Nautilus Minerals are described. The content of this chapter is also based on the preliminary work presented in [1].

### 3.1 The Nautilus Mineral's system

The production system developed by Nautilus Minerals is specifically designed for the extraction of SMS deposits and can be split into three different sections. First of all the deposits need to be dis-aggregated and collected from the seafloor. This is achieved by using remotely operated seafloor production tools (SPTs). The second section conveys the slurry of dis-aggregated minerals and water to the surface through a vertical riser. In order to propel the slurry to the surface, the vertical riser is equipped with a massive lift pump. When it reaches the surface the slurry is processed in a dewatering plant, before it is stored on the production support vessel (PSV) or onto a separate barge carrier. The sections described are referred to as the seabed system (SS), the underwater transportation system (UTS) and the topside system (TS). The production system will primarily operate at 1600 meters depth. However, the system is designed for an operational depth of 2500 meters [22]. A similar production system is likely to be suitable for DSM operation within Norwegian jurisdiction.

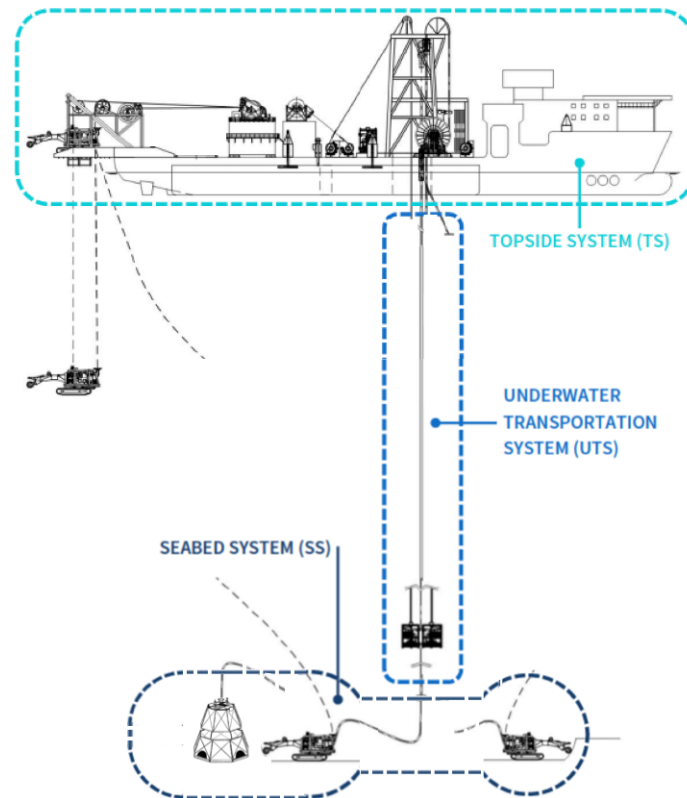


**Figure 3.1:** Illustration of the production system developed by Nautilus Minerals (modified from [13])

### 3.1.1 Seabed system (SS)

The seabed system is primarily performing two tasks, the dis-aggregation and the collection of SMS deposits. Based on the highly demanding conditions, such as the extremely high ambient pressure, low temperature and the rugged terrain at the ocean floor, Nautilus Minerals has developed a system consisting of three distinct mining machines, dedicated to perform specific tasks. The solution is inspired by terrestrial mining, where they have experienced that there is a need for a flexible tool to prepare the mining site before the bulk production system is introduced [19]. The production tools are manufactured by the UK based company, Soil Machine Dynamics. In the following section, the three seafloor production tools (SPTs) are briefly described.

#### **Auxiliary miner (AM)**

The first machine deployed to the mining site is the auxiliary miner, with the purpose of preparing the site for further operation. This includes clearing the landing area for the remaining machines, as well as preparing the surrounding area for bulk production. The AM is equipped with a versatile arm as well as a slurry pump, making it capable of supporting the bulk production at difficult locations [19]. An illustration of the AM can be seen in figure 3.2.



**Bulk miner (BM)**

Whenever a landing area is cleared by the AM, the bulk miner is deployed. The machine generates the main supply of ore slurry by using a large cylindrical cutting drum to cut and grind the ore surface. The mining tool is capable of digging a trench with a depth of four meters. In order to transfer the ore to a stockpile, the BM is equipped with a set of slurry pumps similar to the one found in the AM [19]. A picture of the BM is shown in 3.3.

**Collection machine (CM)**

The collection machine is dedicated to feed the vertical riser with ore from the stockpile generated by the AM and BM. The collection of ore is performed with the help of a long arm equipped with a rotating cutting crown (depicted in figure 3.4), ensuring consistent material flow to the surface. As illustrated in figure 3.1, the CM is the only machine directly connected to the vertical riser system. It can be noted that figure 3.1 illustrates the use of a stockpile hood, located next to the collection machine. The intention with the stockpiling hood is to aggregate the ore slurry received from the AM and the BM and to minimize the plume dispersion from the mining activity.

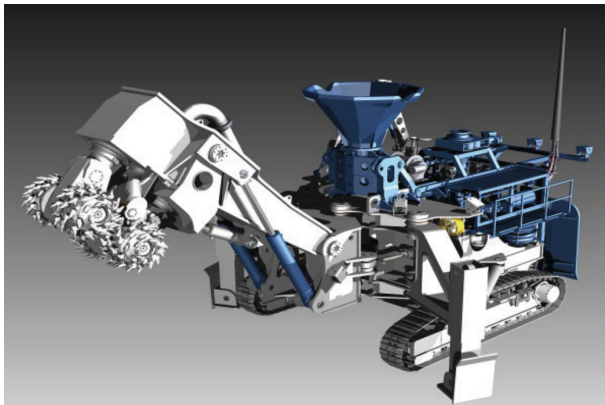


**Figure 3.2:** Auxiliary miner [23]

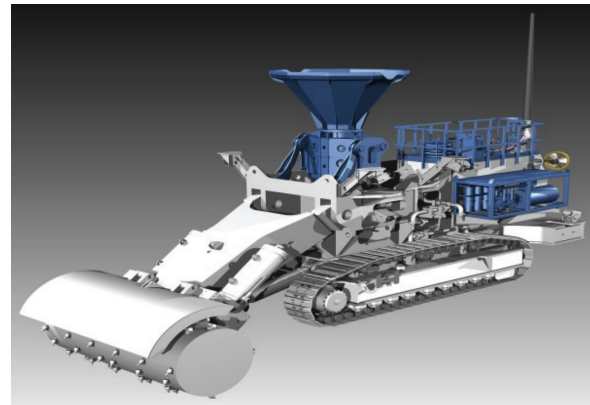


**Figure 3.3:** Bulk miner [23]

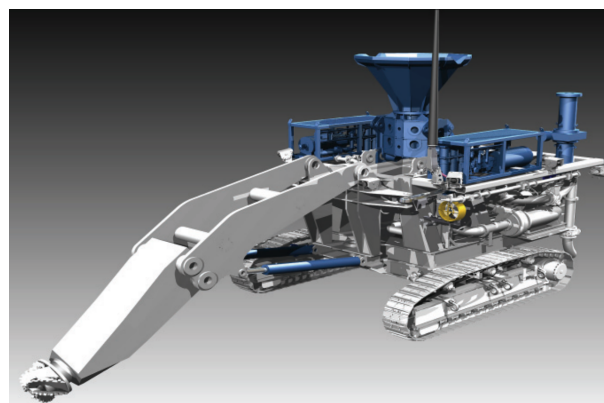


**Figure 3.4:** Collection machine [23]

## 3.2 Underwater transportation system (UTS)

The UTS essentially consists of two components, the sub-sea slurry lift pump (SSLP) and the riser and lifting system (RALS). The RALS is essentially the pipeline connecting the production system to the surface. Together they transport the dis-aggregated minerals to the support vessel.

### 3.2.1 Sub-sea Slurry Lift Pump (SSLP)

The SSLP provides the required pressure to lift the slurry to the surface in one single operation. The pump is suspended fifty meters above the seabed and consists of eight massive positive displacement pumps [24]. Initially, the SSLP was designed with electrically driven pumps. However, due to risk and complexity related to the use of high-voltage in deep-sea environments, the SSLP was decided to be hydraulically powered by a set of centrifugal pumps located at the topside [13]. An illustration of the SSLP is given in figure 3.5.

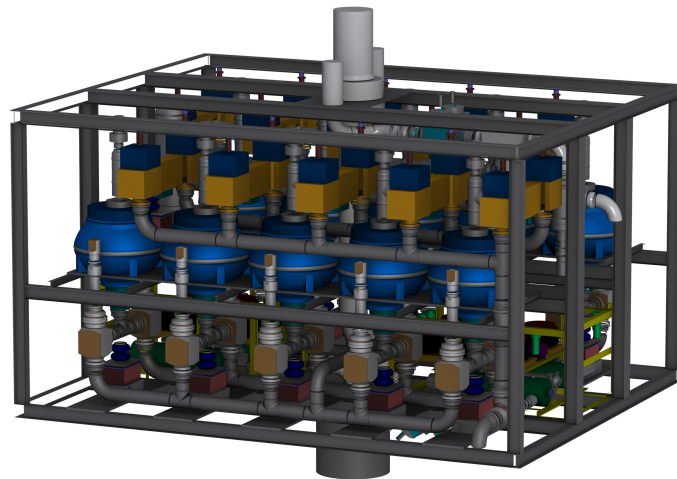


**Figure 3.5:** 3D illustration of the SSLP

## 3.3 Topside system

The topside system comprises the production support vessel (PSV). The vessel is categorized as a mobile offshore drilling unit, with additional features from cargo and special purpose ships, capable of accommodating about 200 personnel [20].

The PSV has generally two main tasks, the generation of power for both topside and sub-sea loads, as well as process the ore slurry received from the UTS. Onboard the slurry is conveyed

to a refinery, which essentially is a dewatering plant. Here the excess water is extracted to make sure the ore is not degraded by oxidation. The ore is then stored locally on the ship and loaded off onto a separate bulk barge whenever necessary (figure 3.6). Furthermore, the bulk barges are shipped to an onshore process facility for further refinement [20].

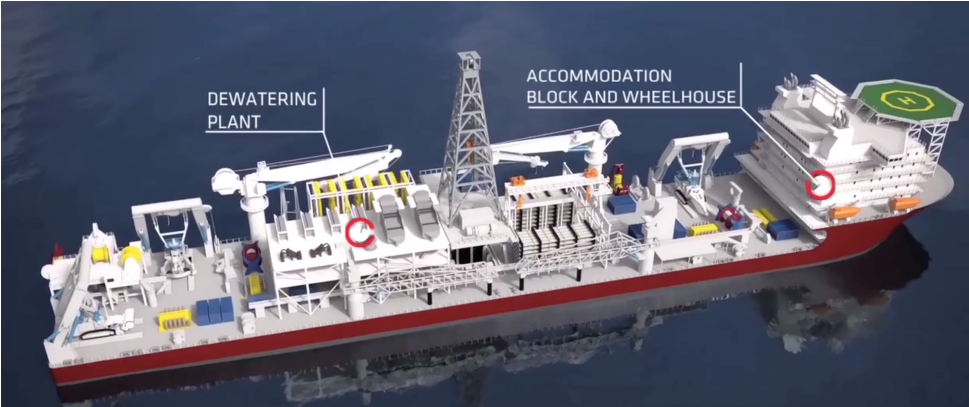
In order to ensure safe operation and to reduce potential strain on the UTS, it is essential that the vessel is able to maintain its geographical location. Thus, the vessel is equipped with a dynamic positioning (DP) system, enabling precise manoeuvring in the order of meters from the desired location. The DP is achieved by controlling five azimuth thrusters and two bow thrusters[13], which aggregated constitutes the main power consumption of the vessel. The power consumption is depending on the roughness of the local weather conditions. The cost of DP is not of great concern for the Solwara project, due to calm conditions in the Bismarck Sea [19]. However, in the more inhospitable waters in the Norwegian Sea, this will likely be a major concern.

Moreover, the vessel is equipped with a launch and recovery system (LARS) for the SPTs. In addition to the lowering and raising of the seabed production system, the LARS also provides on deck storage and maintenance facilities. As illustrated in figure 3.1, the LARS is also the connection point for the umbilicals providing power, as well as communication and control signals, to the respective SPTs. Yet, the RALS is primarily operating pre- and post-production and is therefore not considered as a part of the production system.

In order to supply the required power for both topside and sub-sea operation, the vessel is equipped with six diesel generators, which aggregated deliver 30 MW of power. In order to achieve a level of redundancy, the machines are separated into compartments, each containing two machines [13].

---

<sup>1</sup>Screen-shots from <https://vimeo.com/57181759> April 3 2019



(a)



(b)

**Figure 3.6:** a) PSV with identified dewatering plant and accommodation block b) PSV and bulk barge (Nautilus Minerals)<sup>1</sup>

# Chapter 4

## Power Systems for DSM

In this chapter, the power system associated with the production system discussed in chapter 3 is introduced. Moreover, different design considerations of the power system are discussed, based on the studies conducted in [24], [25] and [22]. The purpose is to determine the most promising topology for operation in Norwegian waters. In order to assess different design aspects, the power system is divided into an onboard and a sub-sea section. The selection of ratings and parameters of the system is also discussed. The chapter is partly inspired by the preliminary work conducted in [1].

### 4.1 Onboard power system

The most common choice of power distribution for onboard power systems is AC. Yet, the DC networks have started to gain more interest due to the development of power electronics. In particular for support vessels, DC is recognized to have certain advantages in comparison to AC distribution. A DC distribution will eliminate challenges such as three-phase imbalances, the need for synchronization and inrush currents in transformers. Still, the main motivation for using an onboard DC network is that it allows the electrical generators to operate unrestricted by the frequency of the system. When operating freely the operation of the generators can be optimized even at loading levels lower than 50%, which means significant fuel savings can be achieved. Moreover, DC distribution also provides benefits such as weight and space savings and accommodates the use of different power and fuel sources (batteries, fuel cells). However, a DC network increases the complexity of the power system due to the switching and the non-linear behaviour of the converters [26].

## 4.2 Sub-sea power system

The sub-sea power system is defined to comprise the converters, umbilicals (dynamic power cables) and the variable speed drives (VSD) powering the loads deployed to the seabed. As discussed by Fared and Tedeschi in paper [24] and Williksen in [22] there are a number of alternatives for the power system configuration. The respective SPTs can be connected to the PSV with individual umbilicals or powered by one or several submersed power hubs (SPH), connected to the PSV via more solid power cables. In mining for SMS deposits, the operation is quite stationary, similar to operation found in terrestrial open cut mines. The operation of the SPTs will remain in the same location over a significant period of time, e.g in the case of Loki's Castle, which is only 200 meters wide [13]. Hence, the system does not require a large level of mobility, which makes the alternative of an SPH more sensible. An increased cross-section of a power cable will provide higher efficiency and moreover reduce the voltage drop in the cable. Yet, these improvements create mechanical challenges. As the size of the cable increases the weight increases, intensifying the vertical tension on the cable. Additionally, the cable will be exposed to an increased horizontal drag due to the increased profile of the cable [25].

### 4.2.1 Power system topologies

The choice of power system topology is essentially between AC and DC distribution and the number of individual power cables. In the papers by Fard and Tedeschi [24, 25] three different distribution options are investigated, namely standard frequency AC, non-standard frequencies AC and DC. They are primarily evaluated based on their efficiency and compactness.

#### AC distribution

AC distribution is the dominating distribution platform for offshore and onboard installations. Moreover, most of the loads deployed to the seabed in a DSM production system is either synchronous machines or induction motors (for pumps, propulsion and mining tools). Thus, AC distribution is a reasonable alternative to consider. In [24] three different AC configurations have been assessed with a voltage level of 6 kV. For a design depth of 2500 meters, the rated power of the motor loads ranges between 0.36 MW and 1.0 MW (table 4.1).

The first topology suggests to install all the variable speed drives (VSDs) on board the PSV and feed the various motor loads via individual umbilicals (figure 4.1). The configuration simplifies the complexity of components deployed to the seafloor, which might improve the reliability of the system. However, there is a power loss of 10% and a voltage drop of 12% associated with this configuration [24]. Moreover, when considering the cost of having numerous separate umbilicals and the much-needed space the VSDs will occupy onboard, the configuration is con-

sidered to be inappropriate.

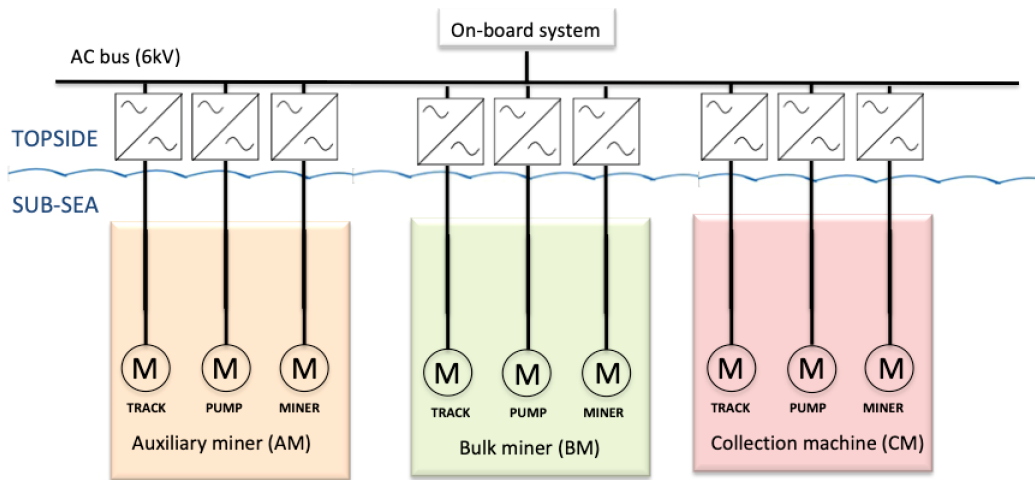


**Figure 4.1:** VSDs installed topside

The second topology is the one selected for the Solwara 1 project. It suggests installing the VSDs on the respective SPTs at the seafloor, reducing the number of individual umbilicals to three (figure 4.2). Consequently, aggregating the motor loads to represent the respective SPTs. An estimate of the rated power of the respective SPTs is defined as the "Total load" in table 4.1. It is shown that the topology greatly enhances the voltage level and reduces the power loss by approximately 50%, compared to the topology with converters installed on the PSV [24]. Furthermore, by locating the VSDs on the SPTs the startup performance of the motors is improved significantly. Williksen documented that the replacement of the VSDs is reducing the start-up time of the motors by 50% [22].

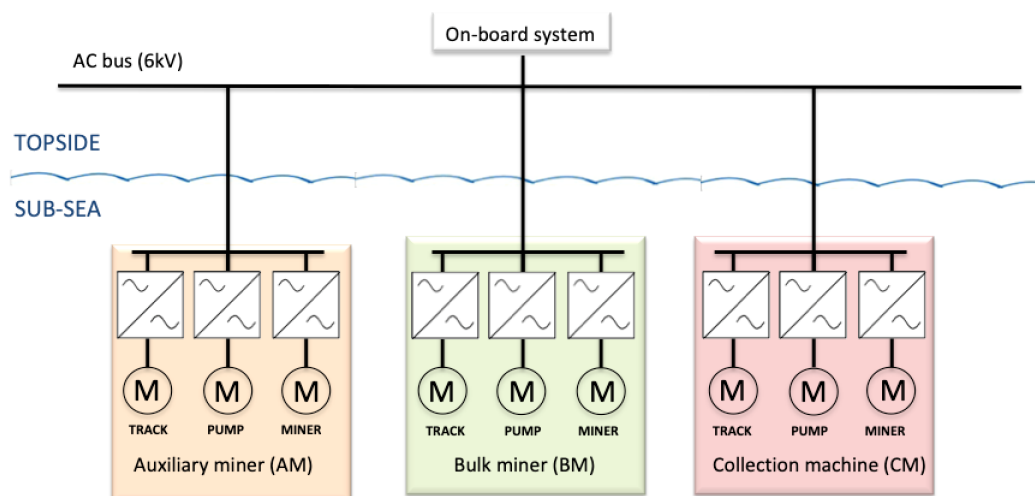


**Figure 4.2:** Individual umbilicals for the respective SPTs with VSDs installed sub-sea

The third topology suggests supplying all loads through a single centralized SPH (figure 4.3), which will reduce the voltage drop and the power loss even further. Based on the estimates in table 4.1, the aggregated load of the production system is at 7.8 MW. Due to the high loading level from the point of view of the supply cables, a voltage level of 13kV is considered to be suitable. With this configuration, the voltage drop will be at 2% and the power loss will be as low as 1% [24]. Yet, the topology requires large transformers, which might violate space and weight restrictions. In addition, the reactive power demand associated with the transformers needs to be compensated.

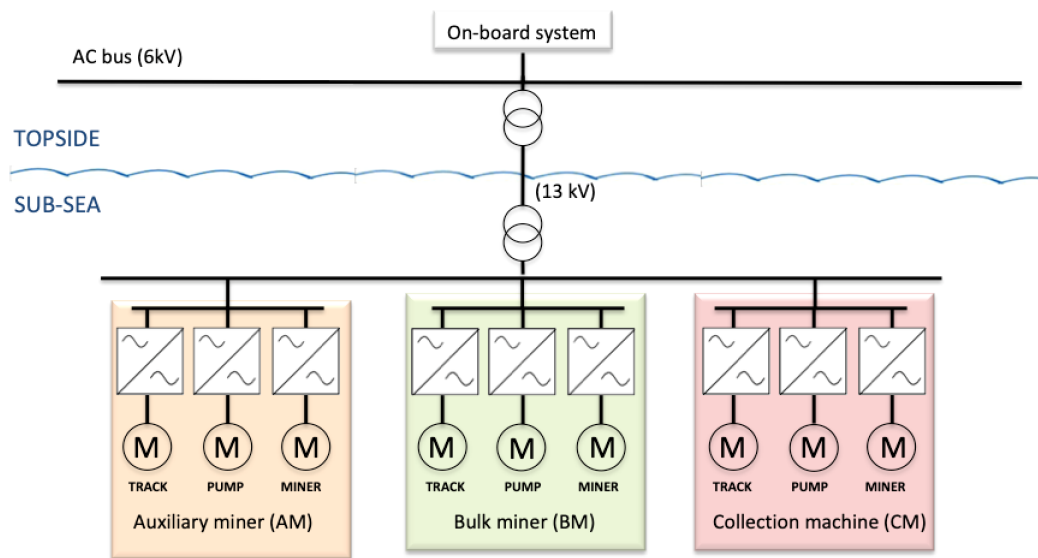


**Figure 4.3:** Single SPH supplying all sub-sea loads

### Non-standard frequency AC

Fard and Tedeschi have also investigated the use of non-standard frequency AC, where a low-frequency AC (LFAC) of 16.67 Hz and a high-frequency AC (HFAC) of 400 Hz as a distribution alternative have been evaluated [24]. HFAC makes it possible to reduce the weight of the system transformers and allows smaller passive components. However, it also introduces an increased reactive power demand in the cables, which results in more significant voltage drops. Additionally, a number of high-frequency transformers are needed. Hence, HFAC will not be considered. The LFAC has very promising characteristics for long distance distribution. Yet, a major drawback is the size of the required transformers. As weight and space are of uppermost importance both in the SS and the TS, LFAC is therefore not recommended for a DSM system.

### DC distribution

DC based distribution solutions have gained increased interest due to the improvement of converter technologies. DC cables have a lower resistance compared to an equivalent AC cable due



to the elimination of proximity effect and skin effect. Consequently resulting in higher power transfer capability of the cable. Moreover, because of the constant electric field, the voltage level can be increased or the insulation level can be reduced accordingly. Furthermore, an AC cable will need three conductors, while a DC cable will only need two. A DC cable will therefore have significant weight and space advantages compared to an AC cable satisfying the same power requirements. In figure 4.4 the advantage of the static electric field is illustrated. By increasing the voltage level, the power transfer capabilities will be improved even further.

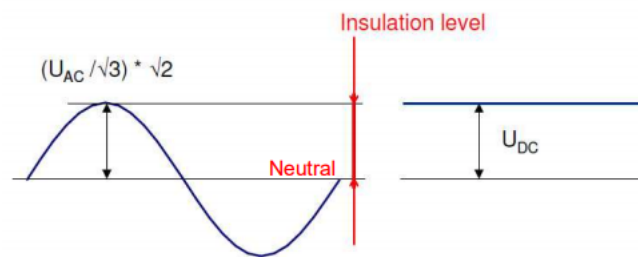


**Figure 4.4:** Advantage of a static electric field [27]

A DC based system will also allow a reduction of the number of components required at the seafloor. The frequency converters (comprising both a rectifier and an inverter) required in a AC based system can be replaced by simpler DC/AC inverters. However, a major drawback of using a DC based solution is the issues related to detection and clearing of faults. There are still major challenges associated with switch-gears for MVDC applications. Hence, the DC based solutions await the development of solid-state circuit breakers in order to challenge the AC based solutions [28].

In terms of the DC-link there are essentially two relevant configurations, either a monopolar or a bipolar link. The monopolar link returns the current through ground (sea water), which means it requires only a single conductor to operate. However, free return might result in severe corrosion and undesirable environmental impacts. A bipolar link has two conductors, which means no return through ground. A major advantage of the bipolar configuration is the provided redundancy. When a fault occurs at one of the conductors, the remaining conductors can act as a monopolar link [29]. Moreover, the power rating required of each conductor is half of the rating of the monopolar conductor [27], which closes the gap in cost and weight between the two alternatives. Based on its merits, a bipolar link is considered to be the most appropriate choice for a DC based DSM power system.

### Power converter technology

Power converter technology is essential to achieve the desired performance of any DC based system. For offshore and sub-sea applications the voltage source converter (VSC) is the preferred choice of converter technology. Unlike the line-commutated current source converter (LCC), the VSC is capable of turning its switches both on and off. The fundamental advantage of the VSC is the ability it has to self-commutate, which means it is capable of supplying passive loads and performing black starts. A pulse width modulation (PWM) is the conventional technique to generate the desired switching sequences. The drawback of the VSC is primarily the harmonics and the power losses associated with the high switching frequencies. From a physical perspective, VSC technology is the only reasonable alternative for light offshore installations, due to its compact construction.

Power converters are typically seen as constant power loads from the supply side. The behaviour is a result of the tight regulation of current and voltage performed by the converters. An example is a DC/AC inverter operating as a variable speed drive (VSD) of an induction motor. If there is an increase in torque the machine will draw a larger current. To maintain power, the DC voltage is forced to decrease. The behaviour of a CPL is given in figure 4.5. The behaviour can also be explained in terms of the incremental change in impedance during a load change. The initial impedance of a CPL is positive. Yet, there is a negative incremental change in impedance. CPLs are thus recognized as a source of instability [30].

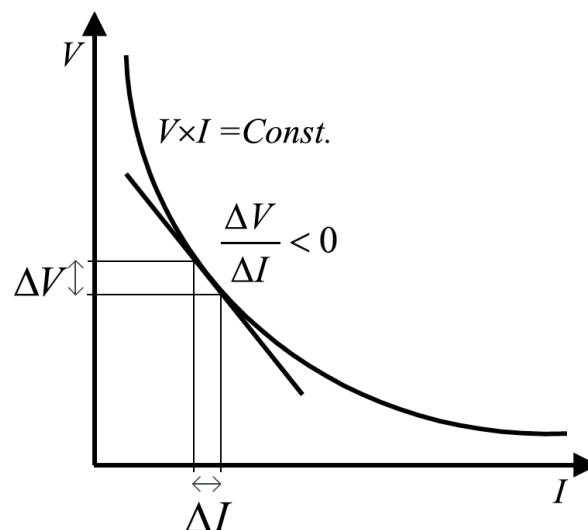


Figure 4.5: Behavior of a CPL [30]

## 4.3 Onboard loads

There are primarily four loads related to the operation onboard the PSV, the DP system, the pumps driving the SSLP, auxiliary systems (e.g. the dewatering plant) and the load related to the housing of the crew. Yet, the SSLP is the only load considered to be a part of the excavation system.

### 4.3.1 SSLP

In the system developed by Nautilus Minerals, the SSLP is driven hydraulically from a number of multi-stage centrifugal pumps located at the surface. Due to the negligible power required for the control of the valves in the SSLP, the unit is therefore considered to be a part of the onboard power system. For the Solwara project pumps with a rating of 1600hp (equal to 1.2 MW) are used, which results in a total power demand of 7.2 MW [19]. A hydraulically fed SSLP lessen the advantage of a centralized SPH because of the low total demand of the sub-sea power system. Hence, three separate feeders are considered to be the most suitable option for this configuration. However, operation below the depth of the Solwara project will increase the power demand of the SSLP [31]. Operation in depths equal to the location of Loki's castle might require the power supply of the SSLP to be revised. An electrically fed SSLP is proposed as an option by Fard and Tedeschi, motivated by the improved efficiency and the elimination of mechanical losses in the hydraulic feeding tubes [24]. With an electrically fed SSLP, the aggregated total installed sub-sea capacity is increased to 13.5 MW (design depth of 2500 meters). Such a significant rise of the sub-sea power demand motivates the use of a centralized SPH, due to the high power losses associated with the use of four individual cables.

## 4.4 Sub-sea loads

The sub-sea loads comprise the SPTs described in chapter 3 (AM, BM and CM). The power demand of the respective SPT is an aggregation of a number of minor loads, being the mining tools, track belts, pumps and auxiliary loads (e.g lights, cameras and navigation). The auxiliary loads are considered to be small and assumed to be negligible. Similarly to the SSLP, the SPTs can either be powered by an electro-hydraulic or an all-electrical solution. Due to the high efficiency, improved machine performance and reduced maintenance costs, an all-electric solution is the preferred option.

The power consumption of the respective excavation loads, with their corresponding minor loads, is given in in table 4.1. The loads are based on values presented by Williksen and Nautilus Minerals for a design depth of 2500 meters [22, 20].

**Table 4.1:** Installed capacity for a design depth of 2500 meters (equal to the Solwara project)

	<b>Component</b>	<b># of units</b>	<b>Installed Power (per unit)</b>	<b>Total Power Installed</b>
Generation	Diesel-Generators	6	5.0 MW	30 MW
DP	Azimuth thrusters	5	3.25 MW	20.25 MW
	Bow thrusters	2	2 MW	
Other on-board loads	Dewatering plant	1	1.5 MW	2.5 MW
	Accommodation ++	1	1 MW	
AM	Centrifugal Pump	1	0.8 MW	2.0 MW
	Mining Tool	1	0.6 MW	
	Track Drive	1	0.6 MW	
BM	Centrifugal Pump	1	0.75 MW	2.5 MW
	Mining Tool	1	1.0 MW	
	Track Drive	1	0.75 MW	
CM	Centrifugal Pump	1	0.9 MW	1.8 MW
	Mining Tool	1	0.36 MW	
	Track Drive	1	0.54 MW	
SSLP	Triplex Pump	6	1.2 MW	7.2 MW

## 4.5 Power requirement for operation in Norwegian waters

Even though the process of dis-aggregating minerals from the seafloor is quite similar to a terrestrial mine, the environment of the deep sea makes a significant difference. Tests conducted by Technip indicate that the cutting force required to dis-aggregate minerals is highly dependent on the water depth [32]. At depths of 2 km, the required cutting force is estimated to be 3.5 times the force needed in atmospheric conditions. An increase in depth will therefore result in a significant increase in the power demand of the excavation system. The following section is based on the estimations performed by Williksen in [22].

The vent site of Loki's Castle is located at about 2400 meters depth. In order to have an equal safety margin as Nautilus Minerals, the system should be designed for a depth of 3500 meters. The loads affected by the increased depth the mining tools and track drives of the SPTs, the SSLP pumps and the DP system. The power requirement of the centrifugal pumps on the SPTs is considered to be independent of the ambient pressure. This is based on the assumption that there is no change in height or distance from the SPTs to the stockpile and from the seafloor to the SSLP.

In order to estimate the increased power consumption of the mining tools, a linear relationship between power and depth is used, resulting in an increased power demand of 30%. This is considered to be a fair assumption based on the studies conducted by Technip and Spagnoli et al. in [32, 33]. The installed power of the track drive is assumed to increase with 50%. This

is based on an expectation that the size and weight of the SPTs will increase as the ambient pressure increases. A larger machine will cause more drag and a heavier machine will increase the gravity forces working on the machine. The increased weight is assumed to be a result of the increased capacity of the mining tool as well as other structural reinforcements.

At this depth, the pumps driving the SSLP will need to thrust the ore an additional 1000 vertical meters. According to Yu and Espinasse [31] the required power to transport the ore from 2500 meter depth is less than 6 MW. Assuming a linear relationship between the depth and the power requirement, the estimated power requirement for 3500 meter depth is about 7.8 MW. Also assuming an operation level of 80%, the required installed power is about 9.6 MW, corresponding to eight triplex pumps of the kind used at 2500 meters.

Due to the weather conditions in the Norwegian Sea, it is also likely that the power demand of the DP is significantly increased. An increase in thruster capacity of 25% has been proposed [22]. In order to handle the massive increase in load, a 40% increase of installed generation is also considered as necessary. The estimated values for a design depth of 3500 meters is presented in table 4.2.

**Table 4.2:** Estimated values of installed capacity for a design depth of 3500 meters (based on estimates from Williksen [22])

	<b>Component</b>	<b># of units</b>	<b>Installed power (per unit)</b>	<b>Total Power Installed</b>
Generation	Diesel-Generators	6	7 MW	42 MW
DP	Azimuth thrusters	5	4.0 MW	25 MW
	Bow thrusters	2	2.5 MW	
Other on-board loads	Dewatering plant	1	1.5 MW	2.5 MW
	Acomodation ++	1	1 MW	
AM	Centrifugal Pump	1	0.8 MW	2.5 MW
	Mining Tool	1	0.8 MW	
	Track Drive	1	0.9 MW	
BM	Centrifugal Pump	1	0.7 MW	3.1 MW
	Mining Tool	1	1.3 MW	
	Track Drive	1	1.1 MW	
CM	Centrifugal Pump	1	0.9 MW	2.2 MW
	Mining Tool	1	0.5 MW	
	Track Drive	1	0.8 MW	
SSLP	Triplex Pump	8	1.2 MW	9.6 MW

## 4.6 System for further studies

The most promising configuration of the DSM power system clearly depends on the operational depth. Based on the choices made by Nautilus Minerals, the most promising configuration for a DSM power system down to a design depth of 2500 meters is considered to be a three umbilical configuration with a hydraulically fed SSLP. However, the increased power requirements associated with operation at greater depths increase the incentives for a centralized SPH. Based on the depth of Loki's Castle (design depth of 3500 meters), an all-electric SSLP and a centralized SPH is considered to be the most suitable configuration. Regarding the type of distribution platform, the improvement and maturing of DC related technology will likely make DC distribution the preferred alternative for sub-sea production systems in the future. Thus, DC is chosen as a suitable distribution platform for the DSM power system. The proposed system is illustrated in figure 4.6.

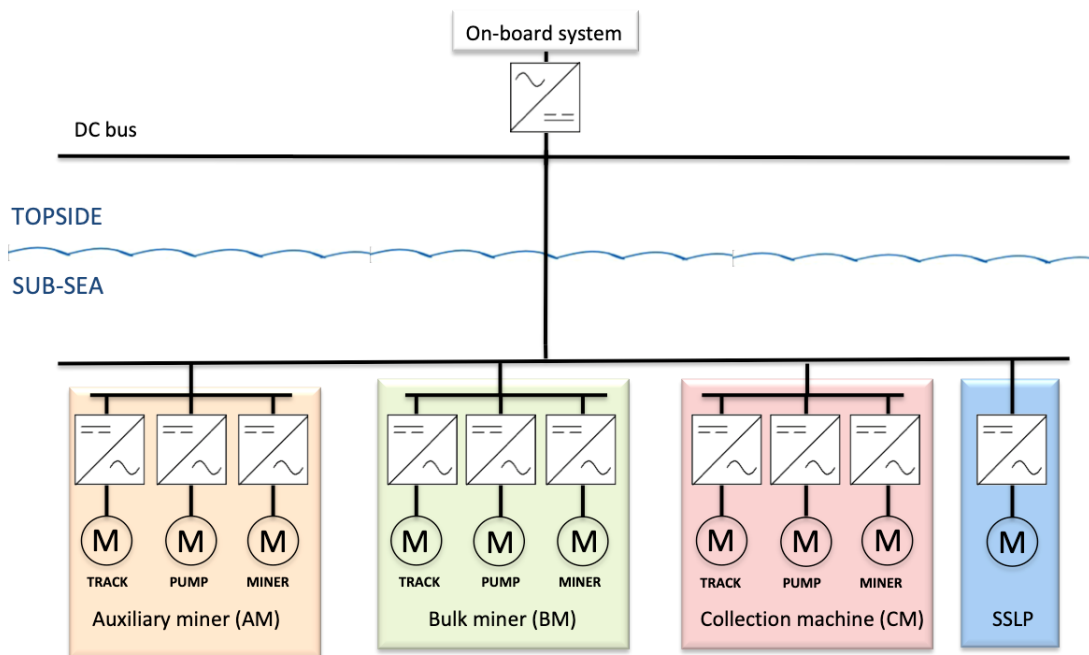


**Figure 4.6:** Proposed DSM power system for a design depths of 3500 meters

The sizing of the system components will be based on the max contemporary power estimations proposed by Fard and Tedeschi in [24]. As indicated in table 4.3, the worst operational scenario of the SPTs will require about 64% of the installed power. This can be justified by considering that the main loads of the machine do not operate simultaneously. The maximum loading will occur when the SPTs are standing still [24]. Both the mining tools and the pumps will be operating at maximum loading, however, the track drive will essentially be switched off. The SSLP is assumed to be consistently operating at rated power.

**Table 4.3:** Max. contemporary power of the sub-sea system [24]

	<b>Component</b>	<b>Worst operational scenario</b>	<b>Max. Contemporary Power</b>
AM	Centrifugal Pump	0.8 MW	1.6 MW
	Mining Tool	0.8 MW	
	Track Drive	0 MW	
BM	Centrifugal Pump	0.7 MW	2.0 MW
	Mining Tool	1.3 MW	
	Track Drive	0 MW	
CM	Centrifugal Pump	0.9 MW	1.4 MW
	Mining Tool	0.5 MW	
	Track Drive	0 MW	
SSLP	Triplex Pump	7.8 MW	7.8 MW

## 4.7 Selection of system ratings and parameters

In the following section, the selection of system ratings and parameters is discussed for the onboard system, the supply cable and the sub-sea load respectively.

### 4.7.1 Onboard system

The ratings of the onboard system are based on the Norsok standard [34]. The standard contains provisions regarding the design of electrical systems and selection of electrical equipment for all offshore units related to the Norwegian petroleum industry. According to the standard, an offshore unit with a total installed power capacity exceeding 20MW should use a three-phase voltage level of 11kV. Hence, a voltage level of 11kV is selected for the onboard system.

### 4.7.2 Sizing of sub-sea supply cable

The max contemporary power demand is considered to be the initial condition in the design process of the sub-sea supply cable, as this also governs the mechanical requirements [35]. From an electrical perspective, the voltage and the current levels are the two essential design aspects. The voltage level should be selected to ensure that the temperature limitation is satisfied as well as to fulfil any voltage drop criterion. Moreover, the voltage level determines the insulation requirements of the cable. An AC cable, with a certain insulation level, re-purposed as a DC cable can increase its voltage capacity with 47% [36]. Thus, the main electrical design concern for the DC cable is considered to be the current limitation related to the thermal properties of the cable. In order to avoid overheating, which increases the ageing of the cable significantly [35], the current needs to comply with a certain maximum current rating. Typically this can be achieved by increasing the voltage rating of the cable, effectively reducing the current in the cable for a given power transfer. Assuming a similar power demand, an increase in voltage will

also allow a smaller cross-section, which again reduces the overall weight of the cable. Yet, the max voltage is limited by the voltage levels of the connected AC systems. The AC/DC voltage ratio, also known as the modulation index<sup>1</sup>, should be within a reasonable range. Since weight and space restrictions are major concerns, an AC/DC voltage difference requiring any additional components, such as step-up transformers or DC/DC converters, should be avoided. A modulation index above 0.7 is considered as desirable.

Since most sub-sea cables are usually custom made for its purpose, there is very limited access to exact technical specifications. The cable parameters for this study have been selected from a set of technical data-sheets provided by Nexans<sup>2</sup>. The data-sheets describe cables of three distinct voltage levels, 10kV, 20kV and 30kV, for a medium voltage (MV) sub-sea power cable with integrated fibre optics, as depicted in figure 4.7. The cables are designed for three-phase AC power and are commonly used for sub-sea applications due to their compact design [37]. Despite designed for AC applications the cables can be re-purposed for DC applications [36]. In a bipolar configuration, the cable will operate two of the cores at  $\pm V_{dc}/2$  and the third as a connected neutral or a grounded neutral. The third core will contribute to additional weight, however, the redundancy will also improve the reliability of the cable. As described in section 4.2.1 the DC voltage can be increased significantly without violating the insulation of the cable. According to Burstein et al.[36], a three core cable operating as a bipolar DC-link will have a rated DC voltage of,

$$V_{n,dc} = \sqrt{6}V_{n,ph} \quad (4.1)$$

where  $V_{n,dc}$  is the rated DC voltage and  $V_{n,ph}$  is the nominal phase voltage.

In the first step of the selection process, the cables are assessed with respect to the max current rating. In addition to the absence of skin and proximity effect, the cooling provided by the surrounding seawater is considered to be very effective [37]. Thus, the max DC current rating is assumed to be 20% larger than the given AC rating. From the calculations presented in appendix 4.7.2 it becomes evident that the smallest cable of 10kV is not sufficient in order to supply the max contemporary power demand. However, both 20kV and 30kV are below the DC current limit. Considering that the rated voltage of the onboard system is 11kV, the 30kV option is disregarded due to the large modulation index. A large modulation index might require the introduction of additional DC-DC converters in the DC-link, which steps up and down the voltage. In order to achieve a reasonable modulation index, it is therefore desirable to reduce the voltage level as much as possible without violating the max current limit. The next step in the calculations shows that the rated voltage of the cable can be reduced to approximately

---

<sup>1</sup>The relationship between the peak-to-peak AC phase voltage and the DC voltage

<sup>2</sup>The data-sheets can be located in appendix G



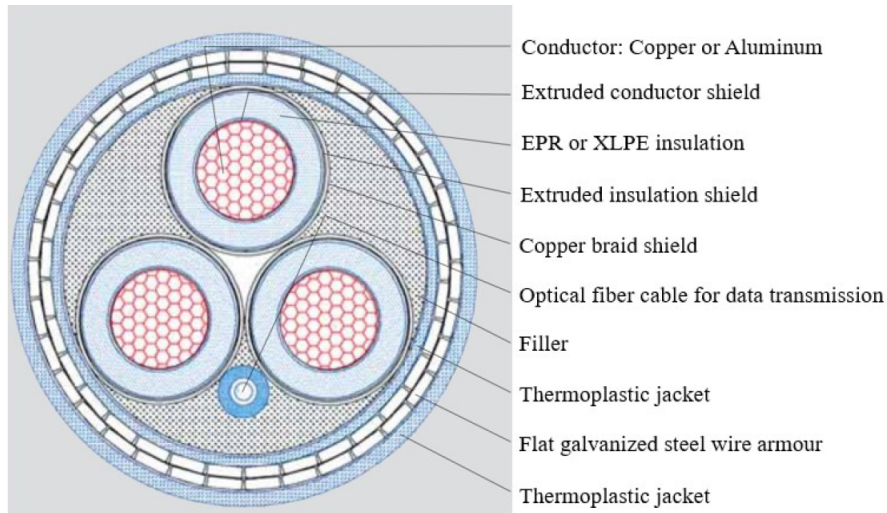


**Figure 4.7:** Cross-section of three core sub-sea power cable [27]

15kV. At this voltage level, the modulation index at the topside converter is at 0.85. Yet, sub-sea multiphase pump and compressor motors are typically designed for a rated voltage of 6kV [38], resulting in a modulation index of the drive at only 0.46. According to [39] there have been successful tests of induction machines for sub-sea applications at voltage levels of 11kV and 13.8kV. By introducing a machine with one of these ratings, the modulation index will be greatly improved and will no longer be considered as an issue. The low modulation index is however considered to be acceptable in order to use the realistic parameters of an induction machine received from ABB. The selected rated values and electrical parameters for the power cable are given in table 4.4.

**Table 4.4:** Rated values and electrical parameters for sub-sea supply cable

Cross section (mm <sup>2</sup> ):	300
Rated power (MW):	12.8
Rated AC voltage (kV):	15.0
Rated DC voltage (kV):	21.2
Max DC current (A):	600
DC resistance pr. conductor (ohms/km):	0.06
Capacitance pr. conductor ( $\mu$ F/km):	0.355
Inductance pr. conductor (mH/km):	0.327
Weight in water (kg/m):	20.4

The mechanical considerations are not explored in depth. Yet, there are a couple of design considerations that should be mentioned. In order for the cable to withstand the immense vertical tension, the cable needs to be wrapped in armour with galvanized steel [37, 35]. The armouring should have a helix formation wrapped in opposite directions. The bi-directional wrapping will not only improve the mechanical protection of the cable, but will also prevent the cable to rotate and twist as a coil spring. Considering a depth of 2400 meters, a cable of

about 3.5 km is considered as adequate. The safety margin is necessary to handle the additional length associated with the motion induced by the sea currents.

## 4.8 Selection of asynchronous machine

The asynchronous machine is the dominant type of machine used in commercial and industrial settings, constituting over 90% of all electrical machines [40]. There are mainly two types of machines, the induction machine, and the double-fed asynchronous machine. However, the former type is the most common. As the induction machine eliminates the need for brushes, slip rings and commutators, it achieves a simple and robust design. This results in low cost and high dependability, which makes it a popular choice for a variety of applications (e.g. pumps and compressors). The induction machine consists of a stationary part and a rotating part, known as the stator and the rotor. The stator of the machine consists of a three-phase winding, while the rotor is made up by windings or short-circuited conductive bars. The type with conductive bars is often referred to as squirrel cage construction, due to its similar appearance. The squirrel cage machine is the type of machine used in this study.

## 4.9 Simplification of sub-sea system

In order to determine the stability on a system level, the dynamics of the sub-sea loads need to be taken into account. Due to the complex composition of different loads, the dynamics of all distinct loads are hard to capture. Thus, the load dynamics are considered to be adequately represented by the most dominant load. Since most of the loads related to the SPVs are relatively small (0.5-1.3 MW), the most dominant load is by far the eight displacement pumps forming the SSLP (7.8 MW). The individual pumps are assumed to have similar operating characteristics, thus an aggregation of these loads is made. The representation compromises the fidelity to a certain extent but is considered to be sufficient to capture the dynamics of the SSLP.

Specific data for machines of this size designed for sub-sea applications are not easily accessible. However, the electrical parameters are likely not to change significantly whether it is designed for terrestrial or sub-sea environments. Therefore, a parameter set for a machine of 9MW designed for operation in atmospheric conditions is selected for this purpose. The machine is one of ABB's A-series of engineered motors, which is strictly customized and tuned for the customers' needs. Thus, it should be noted that the machine parameters might deviate some from a typical machine designed for displacement pump applications. The ratings and parameters of the selected machine are given in table 4.5. The full data-sheet is provided in

appendix H.

**Table 4.5:** Rated values and electrical parameters for squirrel cage machine provided by ABB

Motor type:	Squirrel cage Motor	Stator resistance ( $\Omega$ ):	0,01887
Rated output (MW):	9	Stator reactance ( $\Omega$ ):	0,6271
Power factor:	0,92	Rotor resistance ( $\Omega$ ):	0,01866
Voltage (kV):	6	Rotor reactance ( $\Omega$ ):	0,3748
Frequenzy (Hz):	50	Magnetizing reactance ( $\Omega$ ):	24,82
Speed (rpm):	1492		
Current (A):	969		
Rated torque (Nm):	57607		

# Chapter 5

## Stability definitions and analysis tools

The objective of this chapter is to introduce the conventional definitions of power system stability and to address the most relevant theory related to the modelling and analysis of the proposed system.

### 5.1 Conventional stability definitions

The general definition of stability in a power system is equal to any other dynamic systems. A system is stable if it is able to return to its original state or able to reach a new equilibrium, without compromising the integrity of the system, after being exposed to a small or large disturbance. There are primarily three fundamental categories of power system stability [41].

- Rotor angle stability
- Frequency stability
- Voltage stability

Rotor angle stability is defined as the ability of a synchronous machine to regain synchronism after a disturbance. This is mainly depending on the torque balance in the machine. When subjected to a disturbance the balance between the electromagnetic torque and the mechanical torque is perturbed. Unbalance in the torque creates oscillations and makes the machine to accelerate and decelerate.

Frequency stability is referring to the ability to regain the nominal frequency after being subjected to a perturbation. The stability of the frequency depends on the balance between the production and consumption of power in a system. An excursion in frequency can lead to tripping of protection relays and is often a result of inadequate power reserves.

Voltage stability is defined as the ability to maintain voltage levels within acceptable limits after being exposed to a disturbance. The voltage stability is often associated with the reactive power consumption in distribution lines and feeders, causing voltage drops in the system. Whenever the voltage profile in the system is unacceptably low, the situation is often defined as a voltage collapse.

All three classifications presented above are relevant for a conventional AC interconnected power systems. As presented in chapter 4, the DSM power system is a small isolated power system with only a single generating unit. Moreover, the scope of the study is primarily on the power system related to the sub-sea system. Hence, the rotor angle stability and the frequency stability associated with the on-board system are disregarded. The voltage stability is therefore considered to be the main concern within the scope of this study.

### 5.1.1 Voltage stability

Voltage stability can furthermore be classified with respect to the magnitude of the disturbing signal, namely,

- Large signal stability
- Small signal stability

Large signal stability relates to the ability to maintain the voltage when objected to severe disturbances, such as loss of generation or circuit contingencies. Apart from the dynamic characteristics of the system, the ability to maintain the voltage is mainly determined by the protection equipment and the controllers in the system. Events of this character are normally highly non-linear and commonly analyzed in the time domain.

Small signal stability is associated with incremental changes in the system, such as small load changes. Often linearized models are used to assess this kind of stability problems. The models can provide an overview of the destabilizing effects of the respective parts of the system. Yet, the linearized models are only valid within a certain linear range around the selected linearization point, non-linear effects are hence not considered. In order to obtain a sufficient picture of the system, it is therefore recommended to use both a linearized and a non-linear model in a complementing way [41].

A destabilizing event can be categorized based on its duration in time [42].

- Short term events

- Long term events

The long terms events refer to a time frame of a couple of minutes to tens of minutes. The events are typically a response associated with slow acting equipment (e.g thermostatically controlled loads or when there is an outage of critical components in the system).

The short term is typically related to the faster dynamics of loads, such as electronically controlled loads and converters. The time frame of such events is typically in the order of seconds.

The proposed DSM power system will likely be exposed to both large and small disturbances. Yet, the scope of this thesis will primarily focus on the small signal stability aspects. For the proposed DSM power system, the short time frame is of greatest interest, as it captures the dynamics of the converters and the fast acting equipment located sub-sea. The time frame is able to reflect the issues related to poor tuning of the controllers, which is among the main interest of this thesis. It can be noted that the dynamics present in the range of milliseconds is disregarded.

## 5.2 Stability analysis tools

The analysis tools for stability analysis purposes should be able to adequately capture the dynamics of the system in order to identify instabilities in a given system. Based on the preliminary work conducted in [1], an eigenvalue-based analysis of a state space model has been considered as appropriate for system analysis. This is supported by the analysis performed in [43] and [30], where an eigenvalue-based analysis of a state space model has been used for the analysis of a point-to-point HVDC link and a multi-terminal VSC-HVDC system. The two studies have shown that the state space analysis and linearized models provide a good description of the system stability, which indicates that the non-linearities introduced by the converters are normally small. An eigenvalue based approach is also mentioned by [44] to be beneficial in order to analyze the interaction between control loops in the HVDC terminals, as well as for the tuning of the controllers. The eigenvalue analysis method is considered to be a powerful tool to assess the stability of a system and to identify the components and parameters that have a destabilizing effect on the system. The DSM power system is of similar complexity and structure as a point-to-point HVDC. However, due to the non-linearities of an HVDC system, a complementary analysis a non-linear time domain simulation is recommended by [45]. Both an eigenvalue-based small signal analysis and a time-domain model developed in a SIMULINK environment is selected for the stability analysis of the proposed DSM system.

### 5.2.1 Eigenvalue analysis

The eigenvalue analysis is an analytic method to evaluate the stability of a dynamic system in the frequency domain. The analysis is suitable for small-signal analysis, as it assumes the system to be working within the linear range of a certain working point. By computing the eigenvalues and the eigenvectors of the state space matrix  $A$ <sup>1</sup>, insight in the system behaviour during different operating conditions can be obtained. Eigenvalues of  $A$  are given by the expression 5.1.

$$[A - \lambda I]\phi = 0 \quad (5.1)$$

where  $\lambda$  is the eigenvalue and  $\phi$  is the right eigenvector. A similar expression can be obtained with the left eigenvector  $\chi$ , given in 5.2

$$\chi[A - \lambda I] = 0 \quad (5.2)$$

The eigenvalues are typically referred to as system poles and can be interpreted as a representation of the dynamic behaviour of the system. By plotting the poles into a complex plane, where  $\sigma$  is the real part and  $j\omega$  is the imaginary part, the system instability can be determined. The system is considered to be unstable if any  $\sigma$  is positive, which means the pole(s) are located in the right-hand plane. The stability limit is therefore defined at  $\sigma = 0$ . Poles moving towards the imaginary axis will make the signal closer to instability, while movement deeper into the left-hand plane indicates a more stable system [46].

The pole placement in the left-hand plane is most easily interpreted by considering a second order system. Figure 5.1 shows three responses of a second order system and their corresponding pole placements. For the rightmost pole pair, the response can be observed as oscillatory and slow. As the real part becomes more negative, the system response becomes quicker and the signal settles faster, which mitigates the oscillations in the signal. It can be noted that since the imaginary part is kept fixed, the frequency of the response is unchanged.

---

<sup>1</sup>State space matrix  $A$  is equal to the Jacobian matrix of the dynamic system

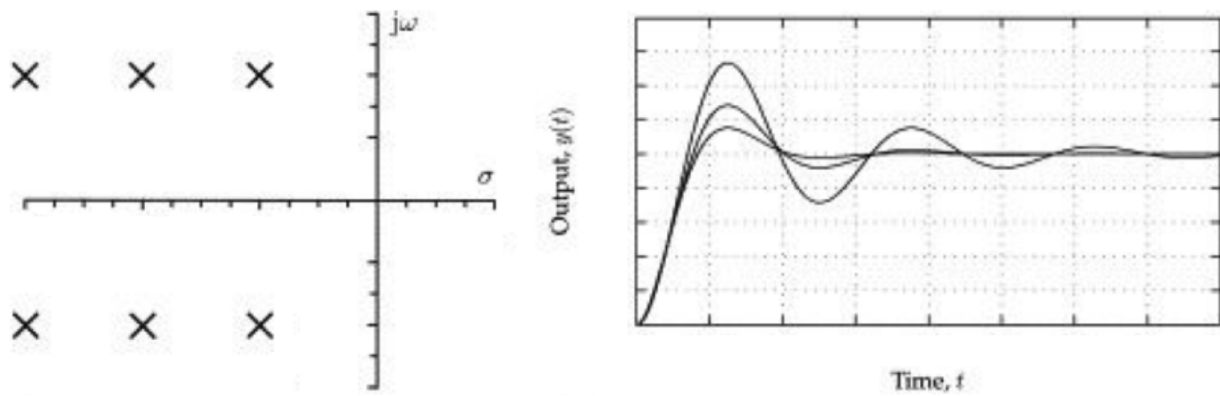


**Figure 5.1:** Pole placement influence on signal response [46]

The imaginary part  $j\omega$  determines the oscillating frequency of the response signal. As illustrated in figure 5.2, a larger imaginary part will result in a more oscillating signal. Also, note that a fixed  $\sigma$  results in the same settling time for all three cases.

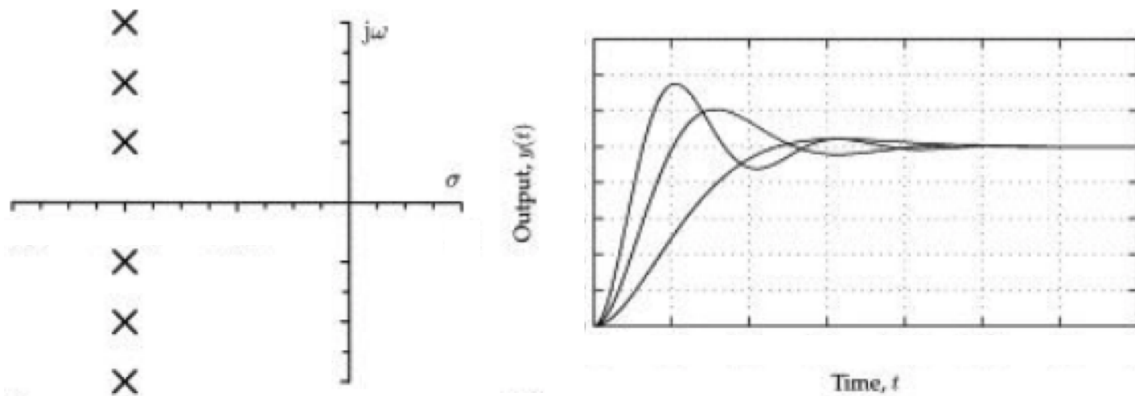


**Figure 5.2:** Pole placement influence on signal response [46]

For higher order systems all poles will influence the system. Yet, there is often a number of dominant poles having the greatest impact on the system response. The dominant poles are the poles located closest to the imaginary axis.

### Damping ratio

The damping ratio is a useful parameter when assessing the stability of a system because it quantifies the percentage overshoot of a signal response. The maximum overshoot of the signal corresponds to a certain damping ratio. This relationship is illustrated in 5.3, where the dotted lines indicate the damping ratio.

Considering an eigenvalue in complex format,  $\sigma \pm j\omega$ , the damping ratio  $\zeta$  and the initial frequency  $f_0$  can be computed according to the expression given in 5.3.



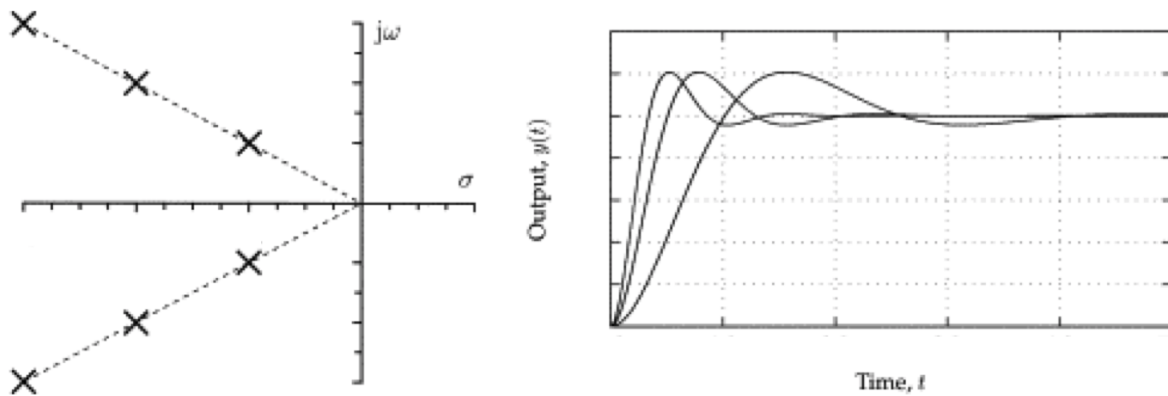


**Figure 5.3:** Pole placement influence on maximum overshoot [46]

$$\zeta = \frac{-\sigma}{\sqrt{\sigma^2 + \omega^2}}, \quad f_0 = \frac{\omega}{2\pi} \quad (5.3)$$

The choice of damping ratio is usually a trade-off between the maximum overshoot and the responsiveness of the system. A low damping ratio results in improved responsiveness, which is favourable to a certain extent. Yet, this will also amplify the peak overshoot of the signal response. The trade-off has no clear optimum and depends on the system application. However, a damping ratio between 0.4 and 0.7 is considered as providing adequate system performance for the general system. This corresponds to a maximum percentage of overshoot in the range between 25% and 5% [46]. For a second order system specifically, Shinnars [47] proposes an optimal damping ratio of 0.7. The damping ratio of 0.7 is obtained by minimizing the product of the time integral before the overshoot occurs, and the magnitude of the overshoot. Based on a specified damping ratio an acceptable region can be established, as illustrated in figure 5.4.

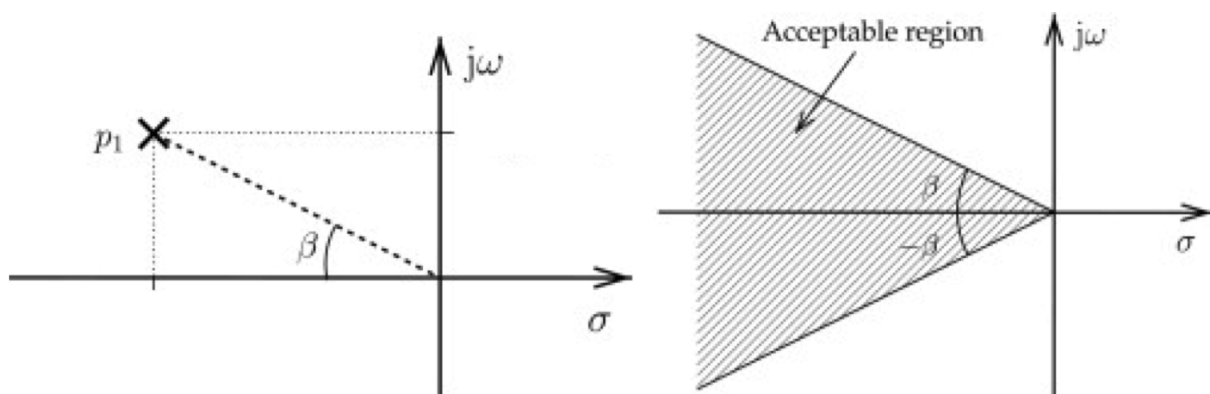


**Figure 5.4:** Acceptable pole placement region [46]

**Participation factors**

Participation factors (PF) are obtained by combining the left and the right eigenvector as given in 5.4,

$$P = [P_1 \ P_2 \ P_3 \ \dots \ P_n] \quad , \quad P_i = \begin{bmatrix} P_{1i} \\ P_{2i} \\ \cdot \\ \cdot \\ P_{ni} \end{bmatrix} = \begin{bmatrix} \phi_{1i}\chi_{i1} \\ \phi_{2i}\chi_{i2} \\ \cdot \\ \cdot \\ \phi_{ni}\chi_{in} \end{bmatrix} \quad (5.4)$$

where  $\phi_{ki}$  refers to the k-th state and the i-th mode of the right eigenvector and  $\chi_{ik}$  refers to the k-th state and the i-th mode of the left eigenvector [48].

The PFs can be interpreted as the relative contribution of a system state to a system pole, or of a system pole to a system state. The PFs are used because they provide a valuable tool in determining which part of the system is contributing to the different poles.

**5.3 Power system strength - Short circuit ratio**

The strength of a power system is recognized as an important aspect to consider when performing a power system stability analysis. The strength of a system is often characterized by the short circuit ratio (SCR) [49], which in an AC/DC system is the ratio between the short circuit power at the AC side versus the rated DC power injected or absorbed. It is important to note that the SCR is only a measure of the strength at a specific point in the system, meaning each system bus will have different SCRs. Conventionally the SCR is determined by the expression,

$$SCR = \frac{S_{sc}}{P_b} \quad (5.5)$$

where  $S_{sc}$  is defined as the power of a three-phase short circuit seen at the short circuit of the grid and  $P_b$  is the nominal power at the DC side. By defining the grid as a Thevenin equivalent the  $S_{sc}$  can be obtained by dividing the square of the nominal bus voltage by the Thevenin impedance.

$$S_{sc} = \frac{V_{bus}^2}{Z_{th}} \quad (5.6)$$

Assuming that the nominal power of the DC side and the voltage at the specified bus is at 1 pu, the SCR can be defined as the inverse of the Thevenin impedance in per unit,

$$SCR = \frac{1}{z_{th}} \quad (5.7)$$

The SCR can be interpreted as the ability to maintain voltage stability in response to disturbances or a metric representation of the voltage stiffness of a system. Equation 5.6 indicates that the SCR depends on the Thevenin equivalent impedance. As the equivalent impedance rises the SCR is reduced, implying a system more susceptible to voltage instabilities. The onboard system on the PSV is small and has a limited amount of short circuit capacity. Thus, it is likely to be characterized as weak. According to [50], a power system is considered as weak if the SCR is lower than 3. Note that this limit is defined for a small land-based grid, yet it is assumed to be applicable also for large onboard systems. Moreover, a power system is considered as strong if the SCR exceeds 5, and is considered as extremely weak when below 1.5.

### 5.3.1 X/R ratio

The relationship between the equivalent inductance and resistance observed from a certain point of common coupling (PCC) is known as the X/R ratio. Utility power systems are typically dominated by the generators, transformers and transmission lines being highly inductive, thus the X/R ratio is generally large. Contrarily, the X/R ratio in a distribution system the X/R ratio is generally much lower than for a transmission system, due to the lower cross-section area of the conductors and the relatively high resistance in the transformers. The X/R ratio for overhead distribution lines are typically slightly larger than one, while slightly smaller than one for underground cables [51]. The onboard system of the PSV is significantly more compact than a typical distribution system. Hence, its characteristics are considered to be closer to an underground cable. An X/R ratio of one therefore seems reasonable for the onboard system.

## 5.4 Resonance frequency

Resonance frequencies occur when the average stored energy in the capacitive elements and the inductive elements of a circuit is equal. At resonance the inductive and capacitive element cancel each other, resulting in a purely real impedance in the circuit. The resonance frequency of RLC circuit can be defined as,

$$f_0 = \frac{1}{2\pi\sqrt{LC}} \quad (5.8)$$

As illustrated in figure 5.5, there are primarily two categories of resonant circuits. Either the circuit components  $R$ ,  $L$  and  $C$  are in series or they have a parallel configuration.

Figure 5.6 shows the circuit diagram of a lumped  $\Pi$  equivalent. The circuit is a combination of the two types of resonance circuits. However, from the viewpoint of the source, the equivalent impedance  $Z_{in}$  is observed as a parallel circuit. In a resonating parallel circuit, a circulating

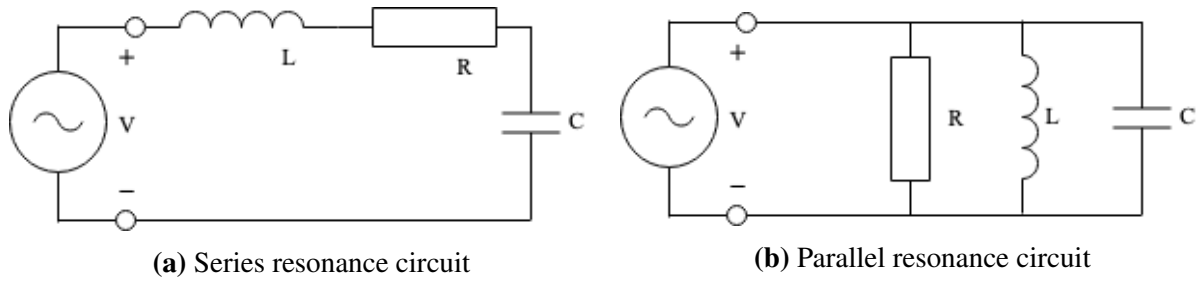


**Figure 5.5:** Types of resonance circuits

current will be generated between the reactive components, creating current resonance in the system. Moreover, the reactive branches will behave like open circuits, making  $Z_{in}$  equal to  $R$ . At resonance, the impedance of the system is therefore at its maximum, creating a highly resistive system with a low current. It should be noted that due to the more complex configuration of the  $\Pi$  model, there will also be some current flowing through the reactive components. For a lumped  $\Pi$  model, the resonance frequency can be defined as,

$$f_0 = \frac{1}{2\pi \sqrt{L \frac{C}{2}}} \quad (5.9)$$

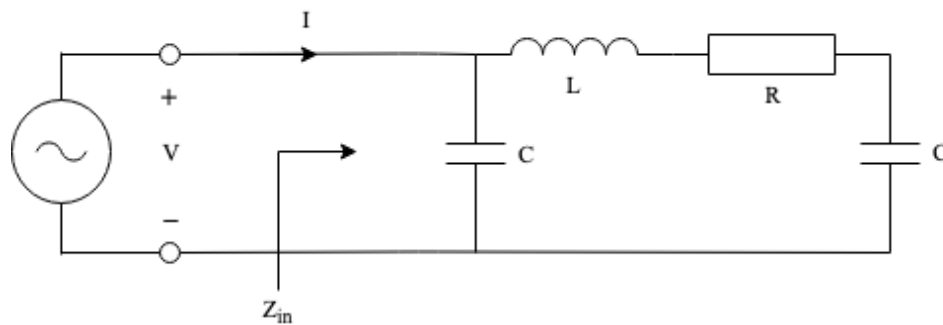


**Figure 5.6:**  $\Pi$  model circuit diagram

# Chapter 6

## System modelling

This chapter aims to describe the layout and provide the mathematical modelling of the dynamics of the proposed system given in chapter 4, with the final objective of giving the framework for the development of the analysis tools (linearized model and time-domain model). Moreover, the control system structure is explained with a brief introduction to the tuning methods. Note that the system will be given as a per unit system, based on the relations given in appendix A.

### 6.1 Power system layout

From the discussion in chapter 4 it was proposed that the most suitable DSM power system topology is a DC based system with a centralized SPH. From a modelling perspective, the power system can be represented as a two terminal medium-voltage DC (MVDC) system (figure 6.1). The onboard system is modelled as a Thevenin equivalent with the synchronous generator representing the aggregated onboard generation and a series impedance defining the strength of the onboard system. Furthermore, a DC voltage controlling VSC is located onboard, forming the topside terminal of the DC-link. In the other end, the sub-sea terminal is connected to a variable speed drive (VSD) supplying a squirrel cage induction motor. The DC-link connecting the two terminals is modelled as a  $\pi$ -equivalent. Due to the limited amount of datasheets, the analysis will be based on a load level corresponding to the SSLP. This is by far the biggest load and is considered to give an adequate indication of the system stability, at least for preliminary investigations.

### 6.2 Average-value model

In order to represent the genuine dynamics of the converters, a detailed switching model can be used. However, this type of model is discontinuous and thus makes it difficult to use in combination with a small-signal analysis. These obstacles have resulted in extensive use of so-called

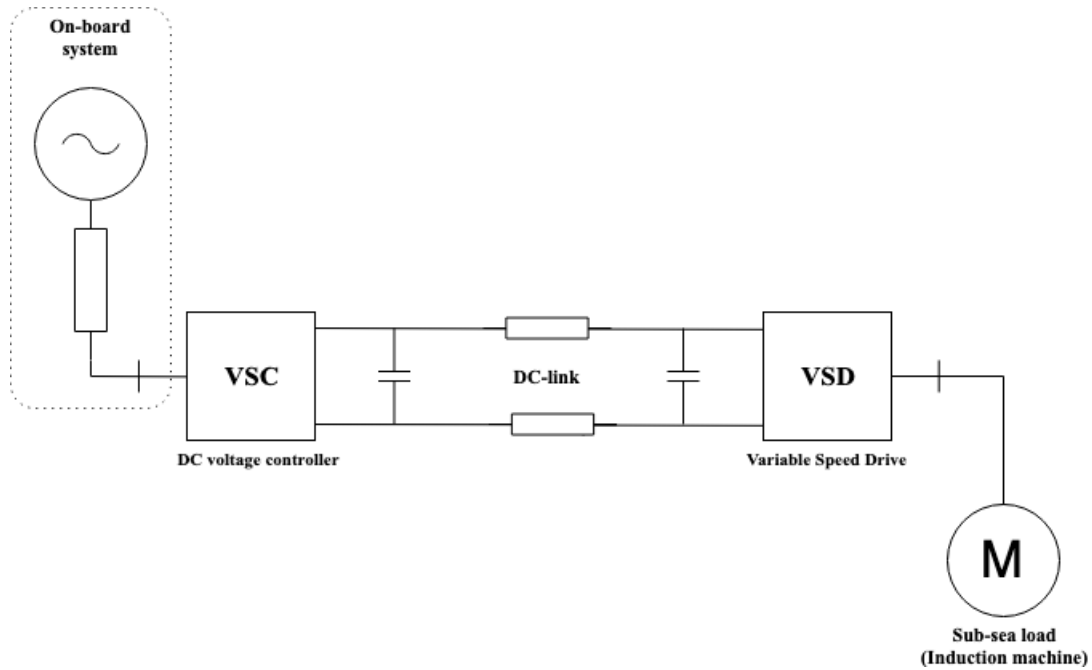


**Figure 6.1:** Schematic overview of the DSM power system)

dynamic average-value models (AVMs). The AVM is essentially neglecting the dynamics of the switching by using the average value of a prototypical time interval. By utilizing an AVM the signals become continuous, which is useful in a small-signal analysis in the frequency domain because it simplifies the modelling of transfer functions. The AVM has been successfully used to model e.g. naval electrical systems and wind energy systems where the machines are connected to a grid via converters [52]. A drawback with the AVM is obviously that it ignores any harmonic distortion, which might be of importance for the power quality [53]. Figure 6.2 shows a conceptual scheme of an average-value modelled VSC, where three controllable voltage sources are representing the AC terminal and a controllable current source is representing the DC terminal. The AVM is considered to be reasonable for a system-level analysis with a time frame in the order of seconds.

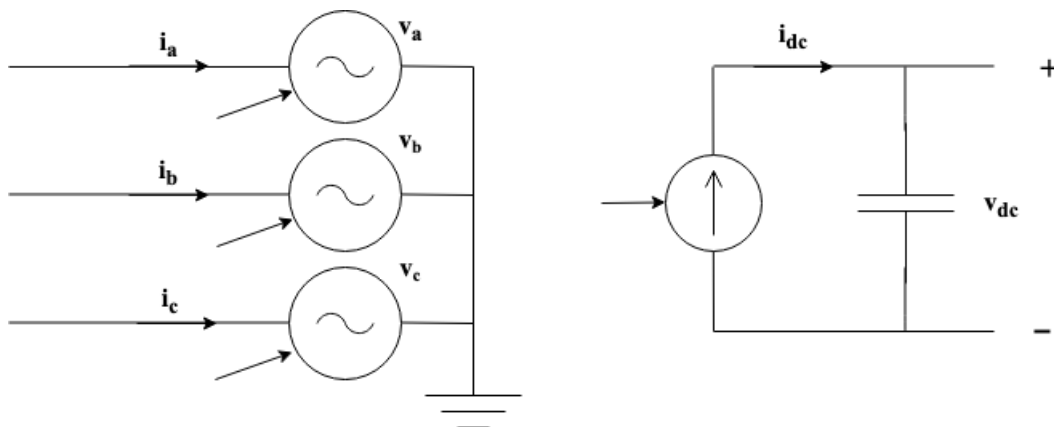


**Figure 6.2:** Conceptual scheme of an average-value model

## 6.3 Dynamics of topside system

The dynamics of the topside system can be derived from the schematic in figure 6.3. The onboard system is modelled as a Thevenin equivalent with a voltage source  $v_g$  and an inner resistance and inductance of  $R_g$  and  $L_g$ . The connection point of the topside VS is defined as the grid voltage  $V_g$ , which refers to the voltage measured by  $C_{cm}$ . At the AC side of the VSC, the resistance and the phase reactor of is modelled as  $R_c$  and  $L_c$ , while the terminal voltage is referred to as  $v_{ct}$ . At the DC side of the converter, the voltage over the smoothing capacitor  $C_c$  is defined as  $v_{dc}$ . The current flowing out from the DC terminal of the VSC is referred to as  $i_{c,dc}$ , while  $i_{c,c}$  is defined as the current flowing through the smoothing capacitor. The resulting current flowing into the link is named  $i_{dc,link}$ .

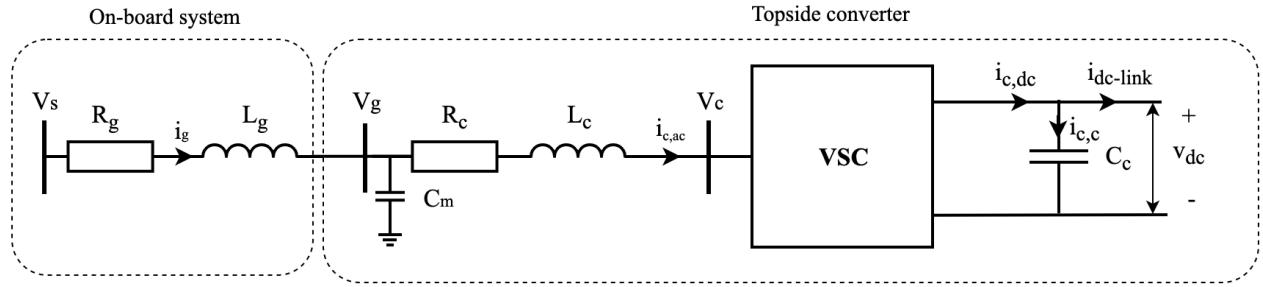


**Figure 6.3:** One line-diagram of onboard power system

### 6.3.1 Mathematical modelling of TS

In the following section, the expressions will be expressed in the direct-quadrature-zero (dq0) reference frame. The full transformation from the abc reference frame to the dq0 reference frame is presented in appendix C.

#### Dynamics of AC side

The dynamic equations of the AC topside system in the dq0 reference frame are expressed as,

$$L_g \cdot \frac{di_g^d}{dt} = -R_g \cdot i_g^d + \omega_s \cdot L_g \cdot i_g^q + v_s^d - v_g^d \quad (6.1)$$

$$L_g \cdot \frac{di_g^q}{dt} = -R_g \cdot i_g^q - \omega_s \cdot L_g \cdot i_g^d + v_s^q - v_g^q \quad (6.2)$$

$$L_c \cdot \frac{di_{c,ac}^d}{dt} = -R_c \cdot i_{c,ac}^d + \omega_s \cdot L_c \cdot i_{c,ac}^q + v_g^d - v_c^d \quad (6.3)$$

$$L_c \cdot \frac{di_{c,ac}^q}{dt} = -R_c \cdot i_{c,ac}^q - \omega_s \cdot L_c \cdot i_{i,ac}^d + v_g^q - v_c^q \quad (6.4)$$

$$C_{cm} \cdot \frac{dv_g^d}{dt} = -i_{c,ac}^d + i_g^d + \omega_s \cdot v_g^q \quad (6.5)$$

$$C_{cm} \cdot \frac{dv_g^q}{dt} = -i_{c,ac}^q + i_g^q - \omega_s \cdot v_g^d \quad (6.6)$$

### Power balance

Since the converters are modelled as an AVM, the switching losses of the converters are disregarded. Based on this assumption and the assumption that the VSC is a constant power device, the power balance can be expressed as,

$$P = \frac{3}{2}(v_{ct}^d \cdot i_{c,ac}^d + v_{ct}^q \cdot i_{c,ac}^q) = v_{dc} i_{c,dc} \quad (6.7)$$

The scaling factor of  $\frac{3}{2}$  is used to achieve an amplitude invariant transformation. However, since this analysis is performed in per unit, the scaling factor can be disregarded.

The d-component of the voltage is chosen to be aligned with the voltage vector and the q-component to be leading with 90 degrees. A 90 degrees phase shift results in  $v_{ct,q} = 0$ . The power balance can therefore simply be expressed as,

$$P = v_{ct}^d \cdot i_{c,ac}^d \quad (6.8)$$

From expression 6.8 it becomes clear that the active power can be controlled by controlling the d-component of the current.

### Dynamics of DC side

The dynamics of the DC side can be obtained expressing the current flowing through the smoothing capacitor,

$$i_{c,c} = C_c \cdot \frac{dv_{dc}}{dt} = i_{c,ac}^d \cdot d_d + i_{c,ac}^q \cdot d_q - i_{dc,link} \quad (6.9)$$

where  $d_{dq}$  is the duty ratio, which is defined as the relationship  $\frac{v_{ct}}{v_{dc}}$ . With the assumption of  $v_{ct}^q = 0$ , the resulting expression for the dynamics of the DC side becomes,

$$i_{c,c} = C_c \cdot \frac{dv_{dc}}{dt} = \frac{v_{ct}^d}{v_{dc}} \cdot i_{c,ac}^d - i_{dc,link} \quad (6.10)$$



## 6.4 Control of topside converter

A common control structure for a grid-connected VSC is a dual-loop vector controller. The structure utilizes the dq0 transformation to map the 3-phase quantities into the so-called rotating reference frame, making it possible to control the active and reactive power flow independently. The dual-loop structure refers to an inner and an outer loop, where the inner loop usually is a current controller. The purpose of the outer loop is to provide the current reference signal to the inner loop. For the onboard VSC, the reference for the active component of the current will be provided by a DC voltage controller. The reactive component of the current can be controlled by a reactive power controller. However, it is assumed that the reactive power of the topside is supplied by the onboard generation, hence an outer control loop for the reactive component of the current is disregarded.

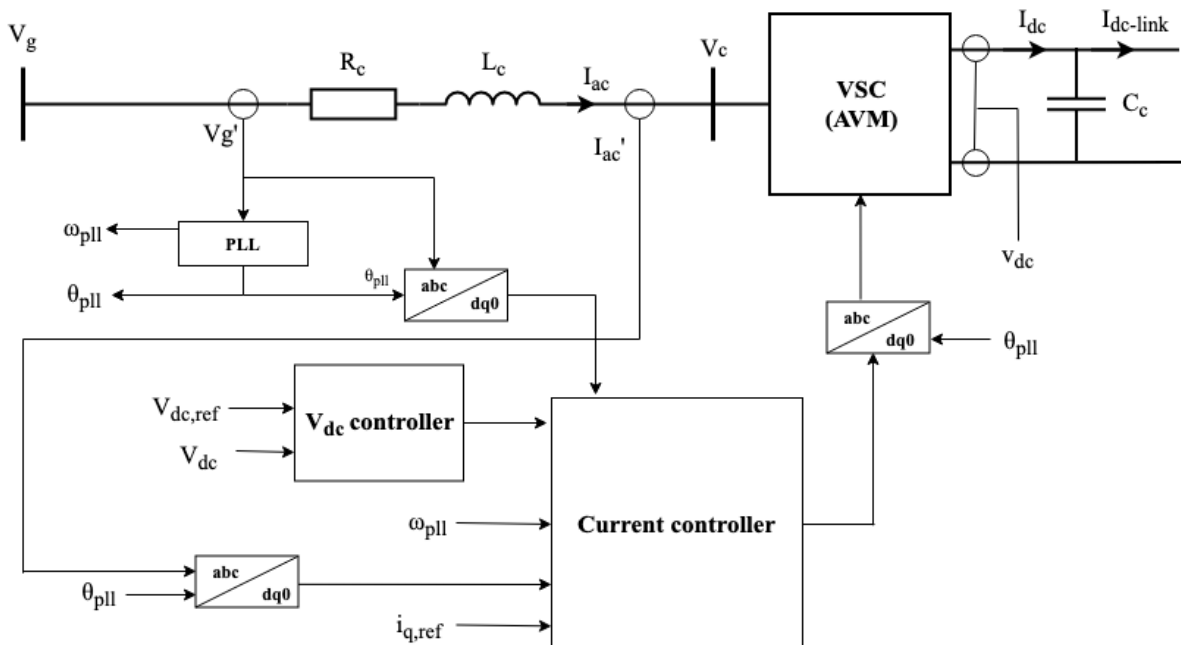


Figure 6.4: Block diagram of the control structure for the onboard VSC

### 6.4.1 Proportional Integral Controller

The PI controller is the preferred type of controller for VSC applications, mainly because of the simple and efficient operation it provides in tracking reference signals. The tracking is achieved by having a proportional and integral gain. The proportional gain ( $K_p$ ) dictates how fast the signal will approach the reference, while the integral gain  $K_i$  operates slower and aims to eliminate any steady-state errors. In the Laplace domain, the PI controller can be represented as,

$$H_{PI}(S) = K_p + \frac{K_i}{s} = K_p \left( \frac{1 + \tau_i s}{\tau_i s} \right) \quad (6.11)$$

where  $\tau_i$  is the time constant defined as the relationship between the gains integral gain and the proportional gain  $\frac{K_p}{K_i}$ . It should be noted that in small signal terms the integrating term in the PI controller creates an additional state in the system.

### 6.4.2 Phase-locked loop (PLL)

In order to perform the transformation from a stationary three-phase frame, a reference angle  $\theta$  is required. Typically, the reference angle is chosen to be the angle of phase  $a$  of the grid voltage. Since the angle is not directly measurable, the angle is estimated using a phase-locked loop (PLL). The phase locking is achieved by adjusting the direct axis reference voltage ( $V_{g,d}$ ) to zero, making the PLL track the phase angle of the voltage vector. As presented in figure 6.5 the tracking is performed by a PI controller. The correction signal  $\Delta\omega$  of the PI controller is added to the nominal angular speed of the grid  $\omega_{g,0}$ . Finally, the resulting angular velocity is integrated to obtain the angle  $\theta$ .

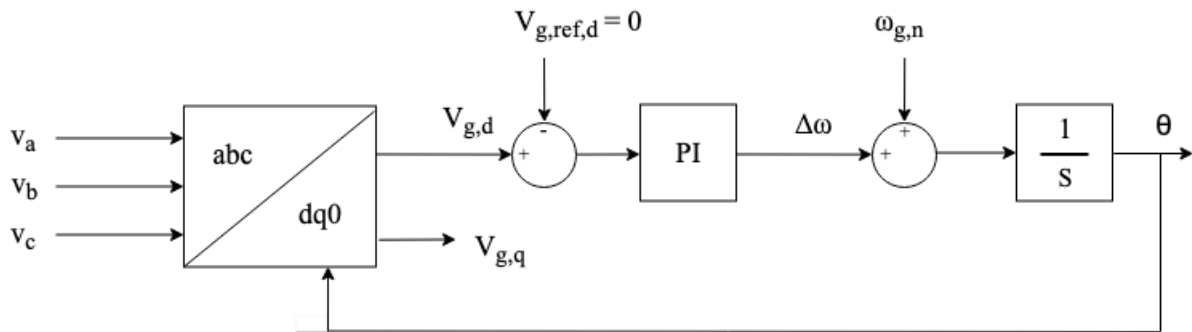


**Figure 6.5:** Block diagram of the control structure of the PLL

The PLL has basically the dynamics of a PI controller and can therefore be expressed as,

$$\frac{d\xi_{pll}}{dt} = v_g^d \quad (6.12)$$

where  $\xi_{pll}$  is the state that counts for the integration part of the PI. The output of the PI then becomes,

$$\omega_{PLL} = \frac{d\theta_{pll}}{dt} = K_{p,pll} \cdot v_g^d + K_{i,pll} \cdot \xi_{pll} \quad (6.13)$$

For the purpose of a small-signal analysis the term  $v_g^d$  can be used as the input error  $\Delta v_g^d$  [30]. This assumption is based on the close relationship between the magnitude of the q-component and the phase error between the grid angle and the  $\theta_{pll}$ . If the d-axis is not in perfect alignment

with the voltage vector  $\underline{v}_g$ ,  $v_g^q$  will deviate from zero.

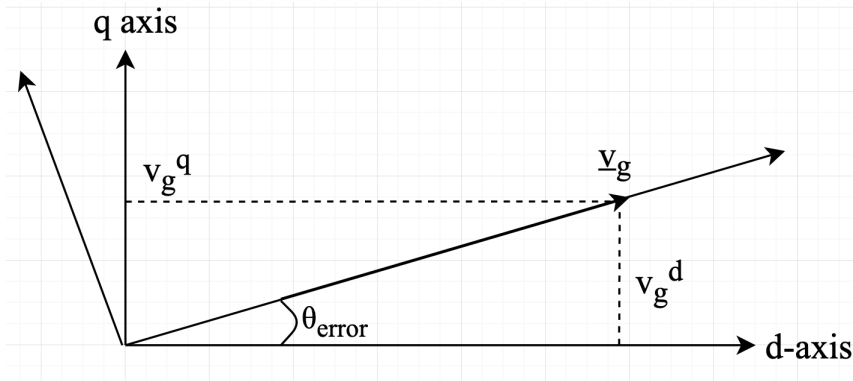


**Figure 6.6:** Relationship between the magnitude of the  $q$  component and the phase error

The tuning of the PLL parameters  $K_{p,pll}$  and  $K_{i,pll}$  can be calculated as suggested in [30],

$$K_{p,pll} = 2a_{pll} \quad , \quad K_{i,pll} = a_{pll}^2 \quad (6.14)$$

where  $a_{pll}$  is the bandwidth of the PLL. The choice of bandwidth is a trade-off between the responsiveness of the PLL and how well it is able to reject noise. A typical value of bandwidth for PLL purposes is 5Hz [30].

### 6.4.3 Inner controller

The inner control loop controls the d and q-component of the current and is thus referred to as the current controller. Its objective is to track the current reference received from the outer control loop. This is achieved by using a vector current control (VCC) method, which finds the amplitude and phase of the terminal voltage corresponding to the desired magnitude and phase of the current flowing through the phase reactor of the VSC. The control method is based on a model inversion structure, which means it inverts the dynamic equation in such a way that the output of the expression is the controllable variable. In the case of the current controller, expression 6.3 and 6.4 are inverted. The two expressions are strongly coupled by the term  $L_c \omega i_{c,ac}$ . As it is desirable to decouple the two expressions, the respective  $L_c \omega i_{c,ac}$  terms are treated as a disturbance and are feed-forwarded. In similar fashion the grid voltage  $v_g$  is also regarded as a disturbance and feed-forwarded, as illustrated in 6.7.

The feed-forward approach eliminates the  $L_c \omega i_{c,ac}$  and  $v_g$  terms from the dynamic expressions. The resulting expression now only contains the dynamics of current  $i_{c,ac}$ , which can be controlled by a PI controller. The full converter system can thus be simplified into the block diagram described in figure 6.8.

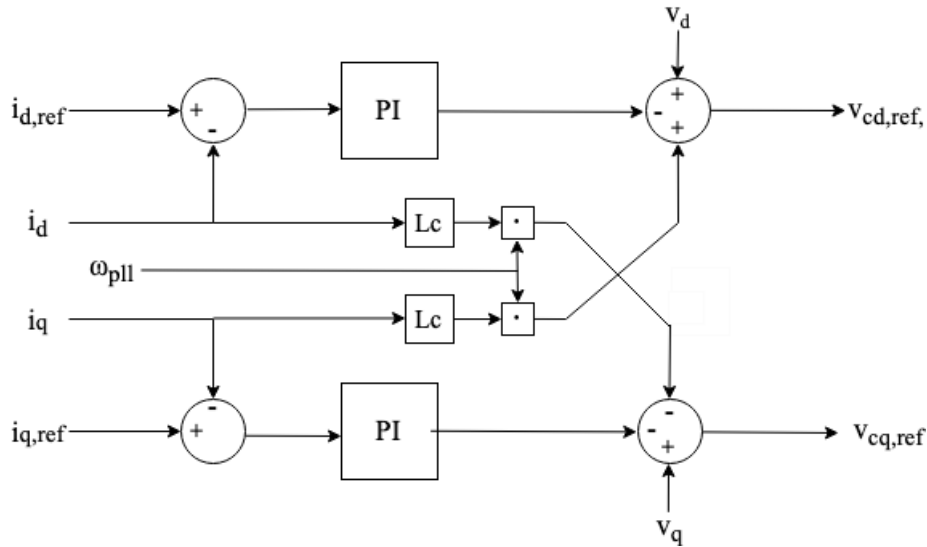


**Figure 6.7:** Block diagram of current controller

The converter is modelled as a delay, with a time constant of  $\tau_c = 1.5\tau_{switch}$ , which is an aggregation of the average delay of the PWM, the delay related to the computation time and the A/D-D/A<sup>1</sup> conversion. Even though the system is modelled as an average model, a switching frequency has to be determined in order to utilize the tuning techniques. Typically the switching frequency ( $f_{sw}$ ) is ranging from 5 to 16 kHz depending on the application. For the topside converter, a  $f_{sw}$  of 10kHz is selected, based on the model presented by Acevedo in [54]. It should be noted that the switching losses might be significant at such high frequencies, however this aspect is not considered as crucial for stability analysis. The  $f_{sw}$  for the drive is selected to be lower. A switching frequency of 5kHz is considered as suitable for general purpose drives [55]. The electrical system is modelled with a time constant  $\tau_{sys} = \frac{L_c}{R_c}$ . The layout in figure 6.8 will make the basis for the tuning of the inner controller.

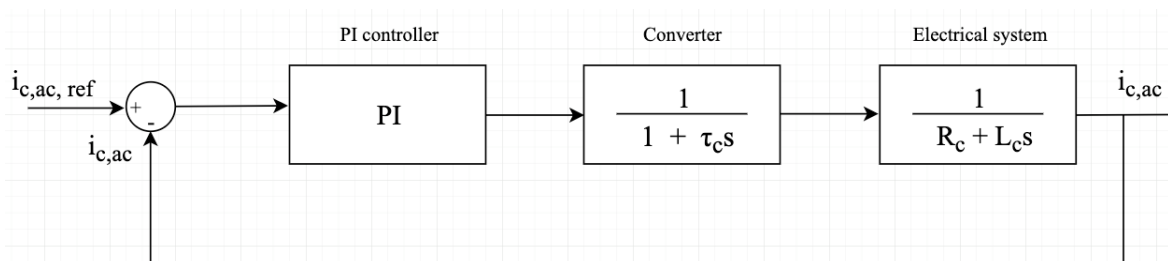


**Figure 6.8:** Block diagram of simplified VCC structure

<sup>1</sup>Analogue/Digital-Digital/Analogue

### Tuning of inner controller

The inner control loop is tuned according to the modulus optimum technique, as it provides a non-oscillatory and fast-tracking of a given reference [56]. The aim of the technique is to create a closed-loop system which maintains a gain of one for a frequencies range that is as wide as possible [57]. This is accomplished by cancelling the most dominant pole of the system. Based on figure 6.8, the open loop transfer function can be given as,

$$G_{c,ol}(s) = K_{pc} \frac{1 + \tau_i s}{\tau_i s} \frac{1}{R_c} \frac{1}{1 + \tau_c s} \frac{1}{1 + s\tau_{sys}} \quad (6.15)$$

The most dominant pole of the system is recognized as the pole of the electrical system. Hence,  $\tau_i$  is defined as,

$$\tau_i = \tau_{sys} = \frac{L_c}{R_c} \quad (6.16)$$

which simplifies the open loop transfer function to,

$$G_{c,ol}(s) = \frac{K_{pc}}{R_c \tau_i s} \frac{1}{1 + \tau_c s} \quad (6.17)$$

Based on the open-loop transfer function 6.17 the transfer function of the closed-loop system can be given as the second order expression,

$$G_{c,cl}(s) = \frac{\frac{K_{pc}}{R_c \tau_i T_c}}{s^2 + \frac{1}{T_c} s + \frac{K_{pc}}{R_c \tau_i T_c}} \quad (6.18)$$

The tuning of the controller aims to ensure a closed loop system with a gain of one. Therefore, the gain parameter is obtained based on the condition  $|G_{c,cl}(s)| = 1$ . Based on this condition the gain parameter is defined as,

$$K_{pc} = \frac{\tau_i R_c}{2T_c} \quad (6.19)$$

The integral gain of is given by the relationship  $K_{ic} = \tau_i K_{pc}^2$ .

---

<sup>2</sup>Further elaboration on the tuning of the inner controller can be found in [56]

### 6.4.4 Outer controller

As previously mentioned the outer control loop is operating as a DC voltage controller. As described in figure 6.9, the voltage controller is essentially a PI controller, which compensates for any deviations from the DC reference voltage. A model inversion structure is also applied for the voltage controller, based on expression 6.10. However, the expression is non-linear and needs to be linearized before being implemented as the base for the control structure. The linearization is performed around the operating point  $v_{dc,ref}$ , which results in expression,

$$C_c \frac{d\Delta v_{dc}}{dt} = \frac{v_{c,0}^d}{v_{dc,ref}} \Delta i_{c,ac}^d \quad (6.20)$$

By transforming the expression into the Laplace domain, the expression can be rearranged into,

$$\frac{V_{dc}(s)}{I_{c,ac}^d} = \frac{v_{c,0}^d}{v_{dc,ref}} \frac{1}{C_c s} \quad (6.21)$$

where  $v_{c,0}$  is the steady state terminal voltage of the VSC.

As presented in expression 6.18 the current controller can be represented as a second order system. However, for tuning purposes of the voltage controller is normally simplified by approximating a first order system. The approximation is made by requiring the original second order system and the first order system to have equal time integrals after a step input [56]. Hence, the closed loop transfer function of the current controller can be given as,

$$G_{c,cl}(s) = \frac{\frac{K_{pv}}{R_c \tau_i \tau_c}}{s^2 + \frac{1}{\tau_c} s + \frac{K_{pv}}{R_c \tau_i \tau_c}} \cong \frac{1}{1 + \tau_{eq} s} \quad (6.22)$$

where  $\tau_{eq}$  is defined as  $2\tau_c$ .

During steady state conditions there is no change in DC voltage, which implies that current  $i_{c,dc}$  equals  $i_{dc-link}$ . From expression 6.10, the expression for steady state conditions can be obtained. The resulting expression becomes,

$$i_{c,ac}^d = \frac{v_{dc}}{v_c^d} i_{dc-link} \quad (6.23)$$

In per unit, the ratio of  $v_{dc}$  and  $v_c^d$  is assumed to be close to one. The resulting block diagram is given in figure 6.9.

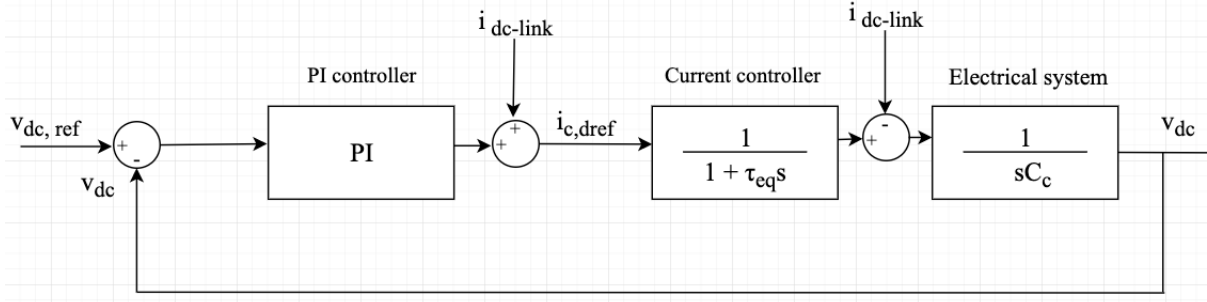


**Figure 6.9:** Block diagram of DC voltage controller

### Tuning of outer controller

Unlike the fast tracking desired for the current controller, the outer controller aims to achieve optimum regulation, while ensuring stability during disturbances. In order to accomplish the desired response, the symmetrical optimum method is applied. The advantage of the method is that it maximizes the phase margin. A large phase margin improves how well the system tolerates delays and its ability to handle disturbances. The symmetrical optimum of the DC voltage controller method returns the following control parameters,

$$\tau_{iv} = \alpha^2 \tau_{eq} \quad , \quad K_{pv} = \frac{\tau_c}{\frac{v_{cv}^d}{v_{dc}} \sqrt{T_{iv} \tau_{eq}}} = \frac{\tau_c}{\frac{v_{cv}^d}{v_{dc}} \alpha \tau_{eq}} \quad (6.24)$$

where factor  $\alpha$  is selected to obtain the maximum phase margin [56].

## 6.5 Squirrel cage machine

The model of the squirrel cage machines is based on the modelling of induction machines described in [40]. There are primarily three different types of modelling that can be made, depending on the choice of reference axis system. The model can be oriented along with the stator frequency, the rotor speed or the along one of the flux space vectors. The stator and the rotor oriented model are creating fictitious stator and rotor windings where the currents become alternating in steady-state operation. All the flux vectors rotate at synchronous frequency, making the inductances independent of rotor position. Consequently, making all the variables behave like DC-quantities in steady state conditions. In order to be consistent with the dq0 reference frame introduced for the topside system, a rotor flux oriented model is selected. As the name indicates the orientation of the system is aligned with the rotor flux vector. The rotation of the rotor flux vector is considered to be quite stable, which makes it suitable as a reference vector for the axis system. With the selected alignment the q-component of the rotor flux ( $\psi_r^q$ ) will be zero, hence  $\psi_r = \psi_r^d$ . Based on the reformulation derived in [40], the rotor flux oriented model can be expressed as,

$$\frac{x_\sigma}{\omega_n} \cdot \frac{di_m^d}{dt} = -r'_s \cdot i_m^d + f_{\psi_r} \cdot x_\sigma \cdot i_m^q + \frac{1}{\omega_n T_r} \cdot \psi_r + v_m^d \quad (6.25)$$

$$\frac{x_\sigma}{\omega_n} \cdot \frac{di_m^q}{dt} = -r'_s \cdot i_m^q - f_{\psi_r} \cdot x_\sigma \cdot i_m^d - n \cdot \psi_r + v_m^q \quad (6.26)$$

$$\frac{d\psi_r}{dt} = -\frac{1}{T_r} \cdot \psi_r + \frac{x_M}{T_r} \cdot i_m^d \quad (6.27)$$

$$\frac{d\theta_{\psi_r}}{dt} = \omega_n \cdot f_{\psi_r} = \omega_n \cdot \left( \frac{r_R \cdot i_m^d}{\psi_R} + n \right) \quad (6.28)$$

where index  $m$  refers to the motor terminals and  $\psi_r$  to the rotor flux. A number of the constants are an aggregation of the basic parameters and are defined as,

$$r'_s = r_s + \left( \frac{x_m^2}{x_r} \right), \quad T_r = \frac{x_r}{\omega_n r_r}, \quad \sigma = 1 - \frac{x_m^2}{x_s \cdot x_r}, \quad x_\sigma = \sigma x_s, \quad r_R = \frac{x_m}{x_r} \cdot r_r$$

The basic parameters are referring to the resistances and reactances of the machine (table 4.5), where index  $s$  refers to the stator, index  $r$  refers to the rotor and index  $m$  to the magnetization of the machine.

The mechanical system is simply expressed as,

$$T_m \frac{d\omega_{mech}}{dt} = \tau_e - \tau_m \quad (6.29)$$

where the time constant of the machine  $T_m$ , the mechanical speed  $\omega_{mech}$ , the electrical torque  $\tau_e$  and the mechanical torque  $\tau_m$  are defined as,

$$T_m = \frac{J \cdot \Omega_n^2}{S_n}, \quad \omega_{mech} = p \cdot \omega_r, \quad \tau_e = \psi_r \cdot i_m^q, \quad \tau_m = K_m \cdot \omega_{mech}$$

$\Omega_n$  is defined as the rated speed in revolutions per second,  $\omega_{mech}$  as the angular velocity of the mechanical shaft,  $\omega_r$  is the electrical angular velocity of the rotor and  $S_n$  is the rated power of the machine.  $K_m$  is defined as the machine constant and is determined based on the torque characteristic of the load. The SSLP can be considered as a massive displacement pump and is therefore assumed to behave like a constant torque load. The machine constant can hence be expressed as the relationship between the rated speed (in rpm) and the maximum torque (in Nm) of the machine,

$$K_m = \tau_{max} / n_{mech}^2$$



It can be noted that pumps usually have low inertia, therefore  $J$  is assumed to be equal to the rotor inertia of the machine.

### 6.5.1 Power balance

As for the conversion from AC to DC, the converter is assumed to be a constant power device. The power balance can thus be given in per unit as,

$$i_{dc,m} \cdot v_{dc,m} = v_m^d \cdot i_m^d + v_m^q \cdot i_m^q \quad (6.30)$$

## 6.6 Motor drive - VSD

The general outline for the variable speed drive of the squirrel cage machine in figure 6.10 is similar to the dual-loop structure presented for the topside VSC. The control principle is known as the rotor flux oriented control, which is a well-established technique for controlling induction machines [40]. In order for the control to operate properly, the position and magnitude of the rotor flux have to be known, however, it is not possible to measure these variables in a squirrel cage machine. Thus, estimation techniques are required. One can perform the estimation with fairly high accuracy down to frequencies of 3-10Hz. Yet, around zero stator frequency, the estimation technique has difficulties. Since the scope of this study primarily on the rated operating point, the low-frequency issue is disregarded. Moreover, an ideal estimator is considered to be a reasonable assumption due to the high precision estimators provide at rated conditions. Dynamics related to the estimator is hence neglected. In order to achieve an adaptive controller, the output signal of the controller is divided by the DC voltage  $v_{dc}$ .

The dual-loop structure refers to an inner and an outer loop, where the inner loop controls the stator currents. The q-component of the stator current can be used to control the torque and the rotor speed. Hence, a speed controller is used to provide the reference signal for the q-component. On the other hand, the d-component determines the magnitude of the rotor flux  $\psi_r$ . In this study the rotor flux will be kept constant up to rated conditions, hence the use of a flux controller is disregarded.

### 6.6.1 Inner loop

The inner loop of the drive is operated as a current controller. Like the topside VSC, the drive utilizes a model inversion method to create the control structure, which means it inverts the dynamic expressions for the stator currents expressed in 6.25 and 6.26. By inspection of these expressions, there is a coupling between the two axes in the model. Therefore, a decoupling

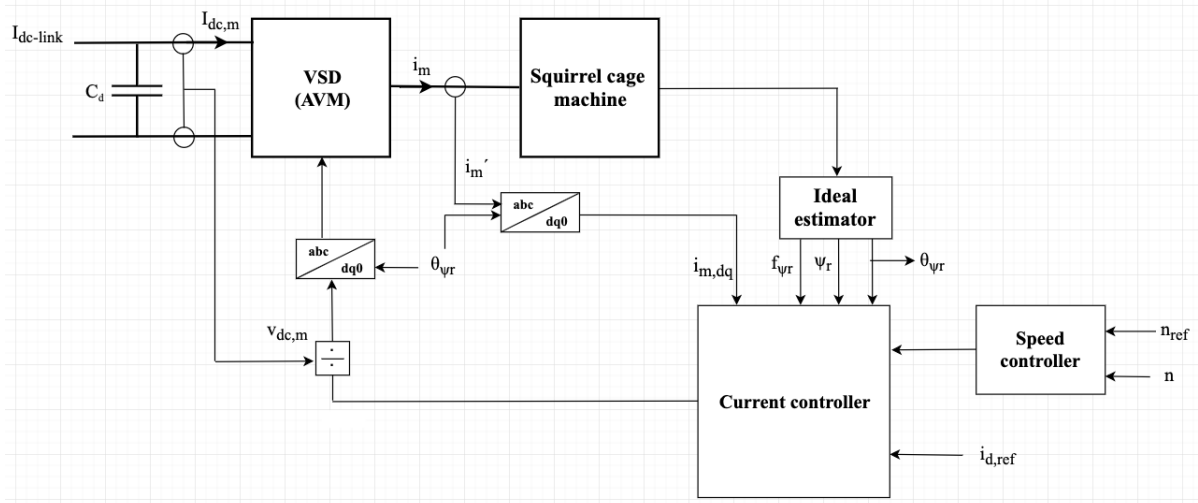


**Figure 6.10:** Block diagram of VSD

is performed by feed-forwarding these terms. The controller can in general be divided into two parts, a PI-based part controlling the dynamics of the current and a feed-forwarding part. Combined they constitute the current controller presented in the block diagram in 6.11.

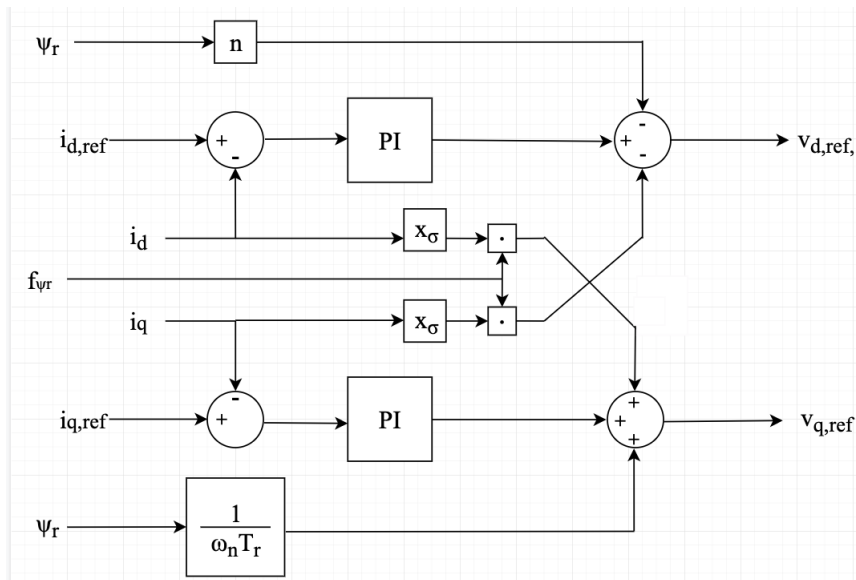


**Figure 6.11:** Block diagram of current controller in the motor drive

### Tuning of inner loop

As for the topside VSC the inner loop of the motor drive can be tuned based on the modulus optimum method. According to [40] the control parameters become,

$$K_{m,p} = \frac{x_\sigma}{2 \cdot \omega_n \cdot T_{delay}} \quad , \quad T_{m,i} = \frac{x_\sigma}{\omega_n \cdot r'_s} \quad (6.31)$$

where the PWM modulation delay  $T_{delay}$  is assumed to be  $T_{sw}/2$ . As previously mentioned this delay is not represented in an AVM, but has to be determined in order to obtain an indication on the control parameters.

### 6.6.2 Outer loop

The outer loop is designed as a speed controller and has the objective of maintaining the desired speed of the machine. The structure of the controller is given in figure 6.12, where the PI controller provides the torque reference, based on the error in mechanical speed. Finally, the current reference is obtained by dividing the signal with the rotor flux.

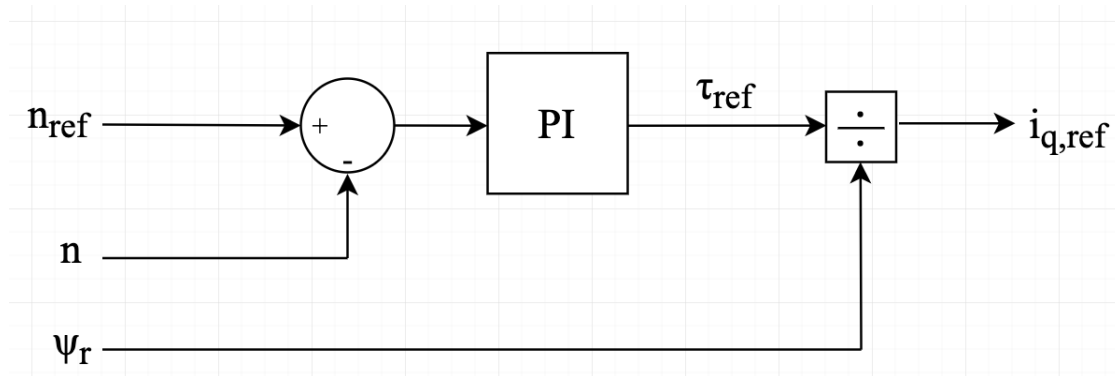


Figure 6.12: Block diagram of speed controller in the motor drive

#### Tuning of outer loop

Similar to the outer loop of the topside VSC, the speed controller can be tuned based on the symmetrical optimum method. Based on this method the values for the control parameters becomes,

$$K_{sp,p} = \frac{T_m}{\sqrt{\beta} \cdot T_{eq,m}} \quad , \quad T_{sp,i} = \beta \cdot T_{eq} \quad (6.32)$$

where the  $T_m$  is the machine constant,  $T_{eq,m}$  is the time constant of the first order equivalent of the current controller and factor  $\beta$  is selected to obtain the maximum phase margin.

The full elaboration of the tuning principles is described in [40].

## 6.7 Dynamics of DC link

Due to the short cable length of about three km, the resonance of the DC-link is assumed to be adequately captured using a lumped  $\Pi$  equivalent model. The simplicity of the model

also allows for analytical derivations. An equivalent capacitance is created to simplify the further analysis, where lower index "c" and "d" are referring to the smoothing capacitance of the converter and speed drive respectively, and "L" for the capacitance of the dc-link.

$$\frac{dv_{dc1}}{dt} = -\frac{1}{C_{eq1}}i_{dc12} + \frac{1}{C_{eq1}}i_{dc1} \quad (6.33)$$

$$\frac{dv_{dc2}}{dt} = \frac{1}{C_{eq2}}i_{dc12} - \frac{1}{C_{eq2}}i_{dc2} \quad (6.34)$$

$$\frac{di_{dc12}}{dt} = -\frac{R_L}{L_L}i_{dc12} + \frac{1}{L_L}v_{dc1} - \frac{1}{L_L}v_{dc2} \quad (6.35)$$

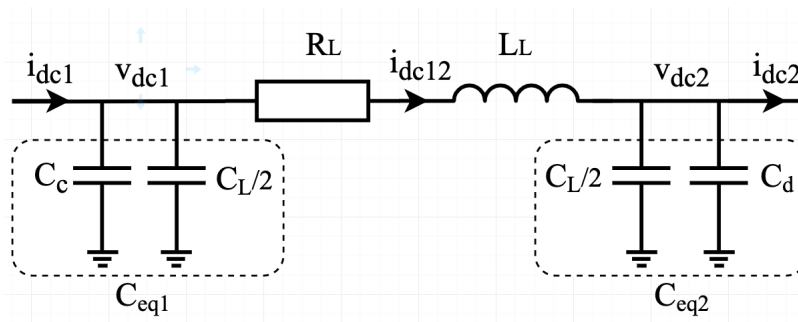


Figure 6.13:  $\Pi$  equivalent of the dc cable

## 6.8 MATLAB/SIMULINK models

From the mathematical modelling provided in this chapter, a linearized model and a time-domain model are developed. The linearized model is developed in a MATLAB environment for the purpose of small-signal analysis. The model utilizes the symbolic math toolbox to obtain the Jacobian matrix of the system, which ultimately forms the base of the eigenvalue analysis. Based on the number of first order expressions, the full system will contain 21 state variables. If the dynamics of the PLL are neglected, the state space will be reduced to 15 variables. The reduction in states is a result of eliminating the need for a measuring point for the PLL. The SIMULINK model is built with blocks from the Simscape library. Due to some simulation issues, a set of SIMULINK specific notes has been added to appendix I, with the intention of providing the necessary explanations and details to replicate the simulations performed with the SIMULINK model.

# Chapter 7

## Stability analysis of DSM power system

This chapter aims to perform systematic simulation analyses of relevant test cases to get an overview of the stability issues related to the developed system. The intention is to investigate which system parameters have most significance on the system stability and to identify the stability limits of the system. Initially, a preliminary study is performed to verify that the system is stable at rated operation. The stability analysis will focus on four different aspects. Firstly, the impact of the various controller gains is analyzed. Secondly, the influence of the strength of the onboard system. Thirdly, the impact of introducing the dynamics of the PLL, and finally the impact of the loading conditions. Participation factors (PFs) are used to identify the influence of the different state variables. All the PF tables are located in appendix D.

### 7.1 Preliminary study of the tuning of the system models

The objective of this section is to verify that the linearized model and the time-domain model are stable at rated operation. Stability is determined based on the definition of stability described in section 5.2.1. The onboard system is assumed to be infinite strong ( $Z_{th} = 0$ ) and the PLL is considered to be ideal. The initial gain parameters are obtained from the tuning principles introduced in section 6.4 and 6.6. For the respective outer loops, an  $\alpha$  of  $\sqrt{6}$  and a  $\beta$  of 4 are initially selected.

**Table 7.1:** Initial gain parameters obtained from tuning principles

Gain Parameters VSC:		Gain Parameters VSD:	
$Kp_{c,c}$	1.59	$Kp_{c,m}$	3.44
$Ki_{c,c}$	33.33	$Ki_{c,m}$	40.06
$Kp_v$	0.20	$Kp_{sp}$	5862.70
$Ki_v$	113.40	$Ki_{sp}$	9771189.54

The first index used in table 7.1 is referring to the controllers, where  $c$  is the current controller,  $v$  is the DC voltage controller and the  $sp$  is the speed controller. The second index distinguishes

the current controller in the topside converter ( $c$ ) and the current controller in the machine drive ( $m$ ). The parameter set results in the pole placement depicted in figure 7.1.

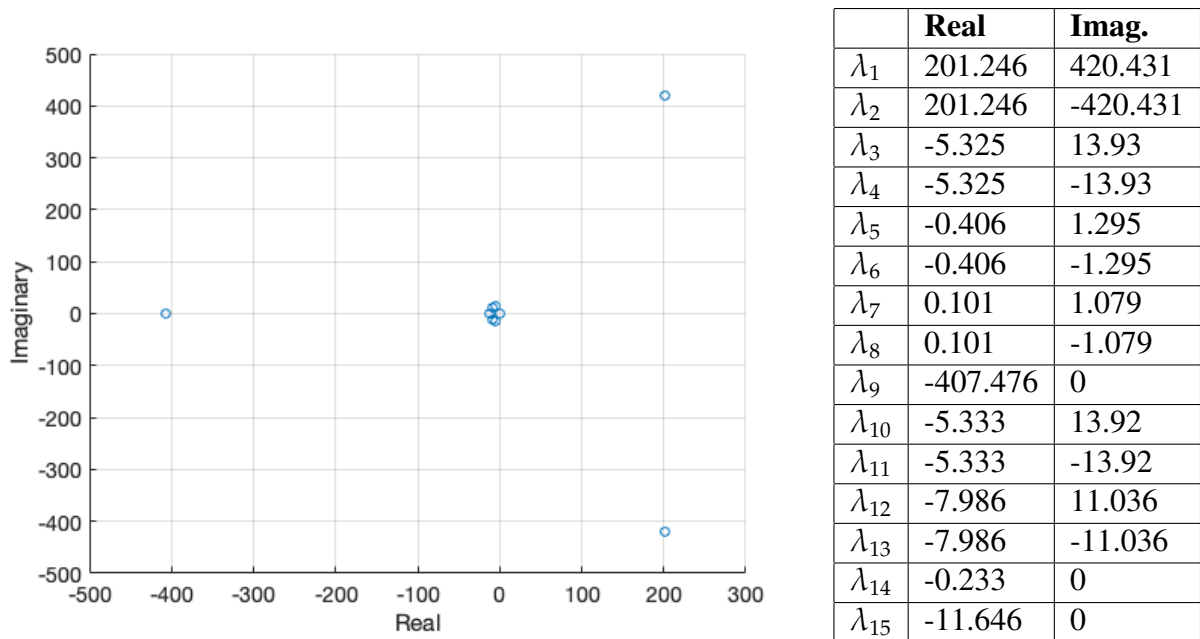
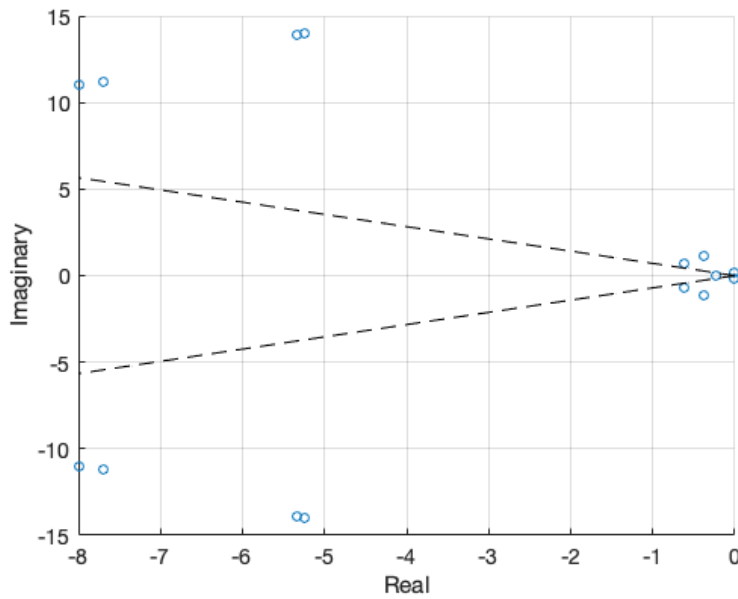


**Figure 7.1:** Poles of system with gain parameters based on the tuning principles

Figure 7.1 shows that there are two conjugate pole pairs with positive real parts, one pair far into right-hand plane and one pair close to the origin, respectively referred to as  $\lambda_{1,2}$  and  $\lambda_{7,8}$ <sup>1</sup>. The PFs are computed to determine the contribution from the state variables. According to the PFs,  $\lambda_{1,2}$  is primarily affected by the state variables  $i_{q2}$ ,  $\xi_{sp}$  and  $n_{mech}$ . Remember that state  $i_{q2}$  is controlled based on the current reference provided by the speed controller,  $\xi_{sp}$  is the error in speed and  $n_{mech}$  is the speed of the machine shaft. Thus, all these state variables are somehow related to the speed controller in the VSD. It is therefore reasonable to believe that the instability of  $\lambda_{1,2}$  is related to the tuning parameters of the speed controller. The pole pair close to the origin is foremost affected by the states  $\xi_v$  and  $v_{dc1}$ . Both these states are clearly related to the DC voltage, thus the instability of  $\lambda_{7,8}$  is considered to be related to the DC voltage controller of the VSC.

As displayed in table 7.1 the gains of the speed controller are of great magnitude. Such high gains will result in considerable overshoot and lead to serious oscillation, which is likely to cause instability. In the DC voltage controller,  $Ki_v$  is considered to be of significant magnitude. Hence, the initial action is to reduce the integral gain in both the outer loops as well as the proportional gain in the speed controller. The adjustment in gains results in the pole placement depicted in figure 7.2.

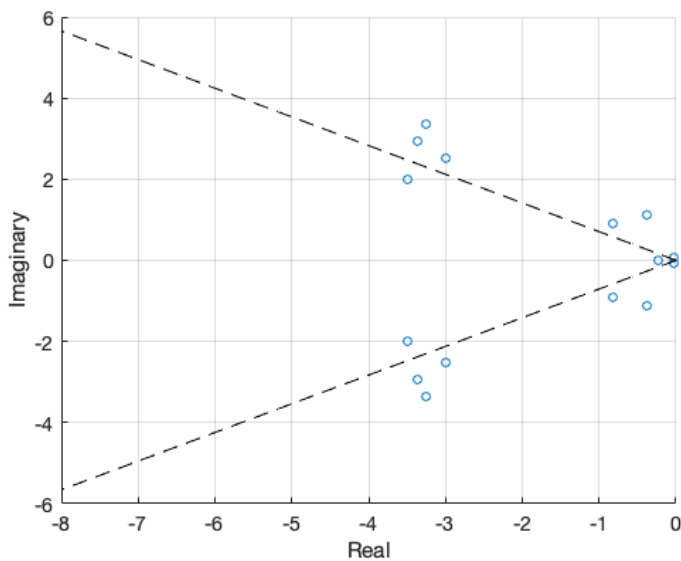
<sup>1</sup>The indices of  $\lambda_{xx}$  are referring to the pole numbers in the table in figure 7.1



	<b>Real</b>	<b>Imag.</b>	<b>Damp.</b>
$\lambda_1$	-5.24	14.01	0.35
$\lambda_2$	-5.24	-14.0	0.35
$\lambda_3$	-0.38	1.2	0.31
$\lambda_4$	-0.38	-1.2	0.31
$\lambda_5$	-5.33	13.92	0.36
$\lambda_6$	-5.33	-13.92	0.36
$\lambda_7$	-0.005	0.11	0.04
$\lambda_8$	-0.005	-0.11	0.04
$\lambda_9$	-7.99	11.04	0.59
$\lambda_{10}$	-7.99	-11.04	0.59
$\lambda_{11}$	-7.70	11.23	0.57
$\lambda_{12}$	-7.70	-11.23	0.57
$\lambda_{13}$	-0.61	0.69	0.66
$\lambda_{14}$	-0.61	-0.69	0.66
$\lambda_{15}$	-0.23	0	1

**Figure 7.2:** Poles of system with adjusted gains in the outer loops

It can be observed that the unstable pole pairs have been moved into the left-hand plane. The result coincides well with the indication obtained from the PFs. Though the system is stable, the damping of a couple of the poles is considered as poor. In figure 7.3 two dotted lines have been introduced to indicate damping of 0.7. Through trial-and-error tuning refinement, a less oscillating system is obtained. A parameter set considered to provide an adequate system performance is given referred to as the well-damped system in table 7.2. As depicted in figure 7.3, most of the poles are now shifted towards the well-damped area.



	<b>Damping</b>
$\lambda_1$	0.7
$\lambda_2$	0.7
$\lambda_3$	0.32
$\lambda_4$	0.32
$\lambda_5$	0.29
$\lambda_6$	0.29
$\lambda_7$	0.75
$\lambda_8$	0.75
$\lambda_9$	0.87
$\lambda_{10}$	0.87
$\lambda_{11}$	0.77
$\lambda_{12}$	0.77
$\lambda_{13}$	0.67
$\lambda_{14}$	0.67
$\lambda_{15}$	1

**Figure 7.3:** Poles of well damped system

A time-domain simulation is performed with the improved gain parameters. Through trial-and-error tuning, a stable time-domain model was achieved. The adjustment from the well-damped gains used in figure 7.3 are given in table 7.2. As displayed in the figures in 7.5, stable voltages and frequencies are obtained throughout the system. A full overview of the system signals under stable conditions can be located in appendix E.

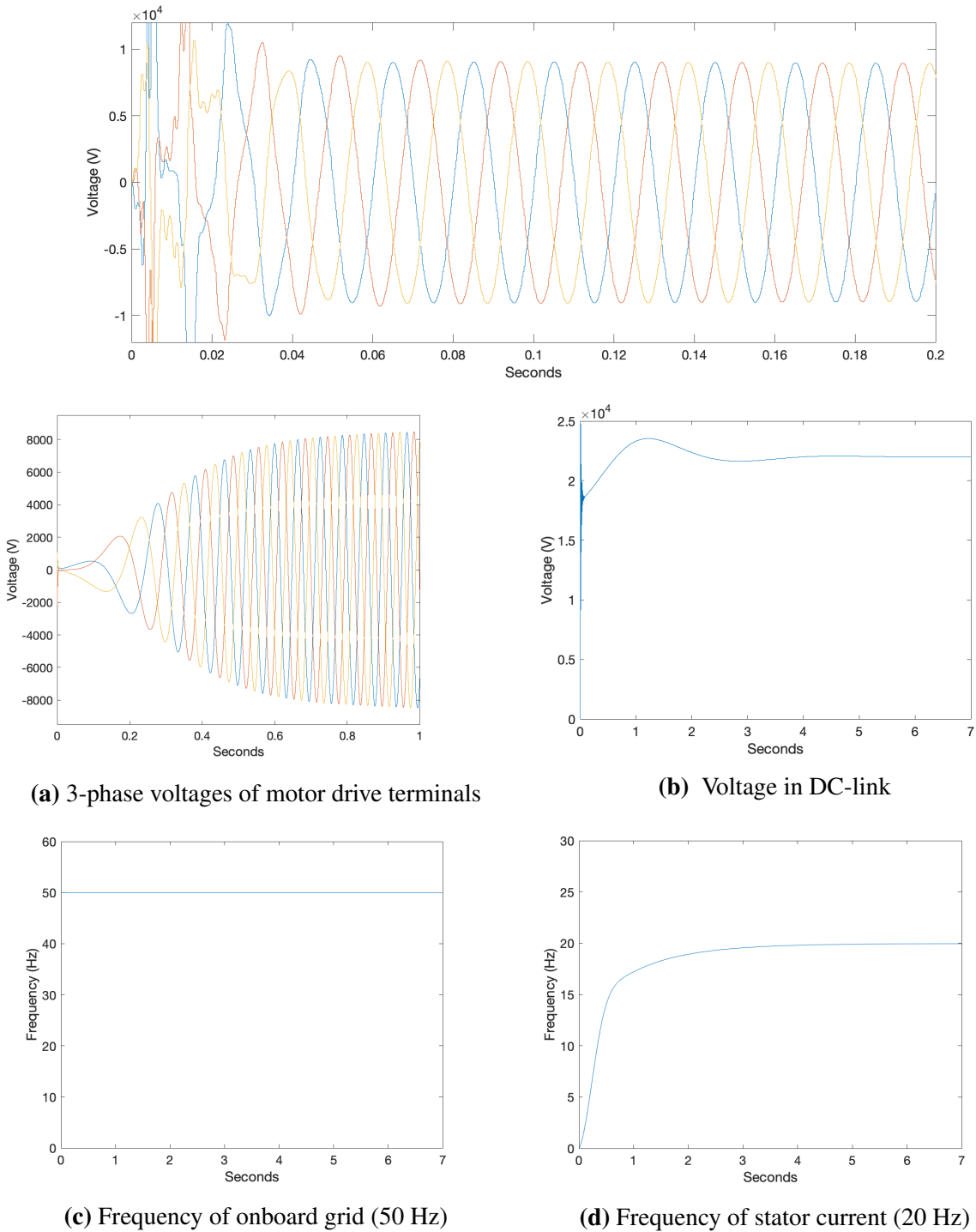
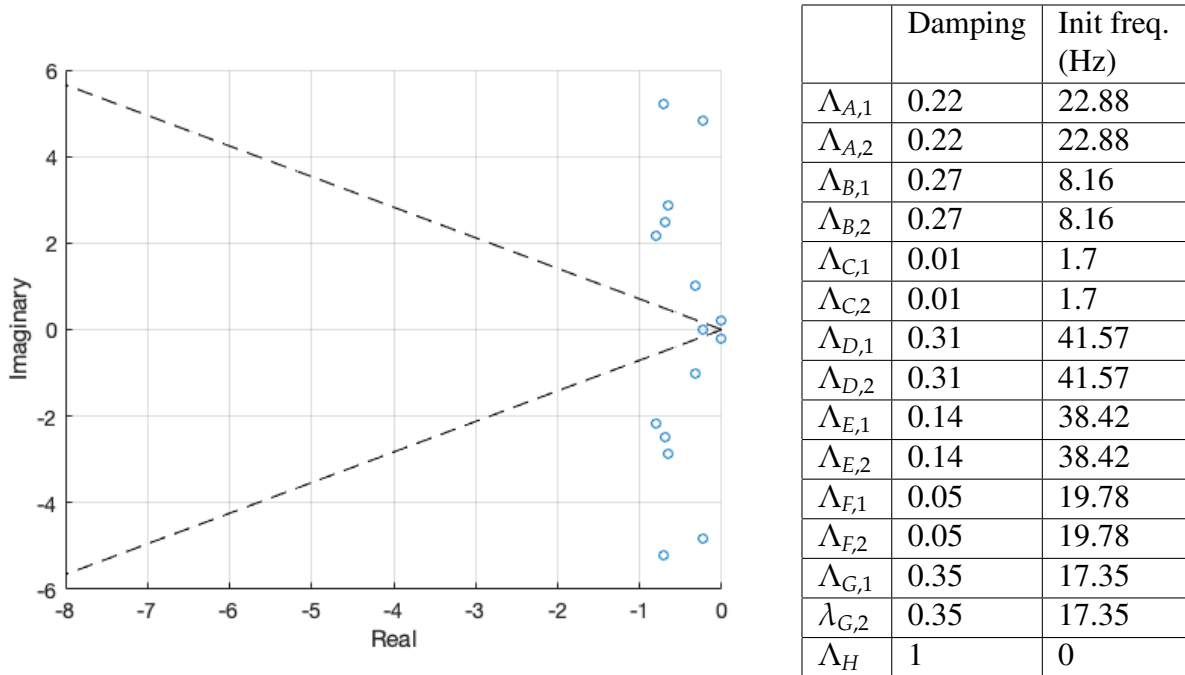


Figure 7.5: Time-domain model - Stable conditions



The gains verified in the time-domain simulation are again fed into the linearized model for a cross-check verification.



**Figure 7.6:** Pole placement with gains from time-domain model

Figure 7.6 shows that all the poles corresponding to the gains of the time-domain model are present in the left-hand plane, which indicates a stable system. It can be noted that this has been a verification process going in both directions, where the steady-state values in the time-domain model have been used to set the point of linearization (loading level) used in the linearized model. The initial frequencies of the base case pole pairs are obtained for the upcoming stability analysis. In order to make the two models complement each other, a common gain parameter set needs to be selected. Due to difficulties in making the time-domain model stable, the selection of base case gain parameters is determined by the time-domain model. In figure 7.6 it can be seen that the selection of gains results in a poorly damped set of poles.

**Table 7.2:** Comparison of the gain parameters of the well damped system and the time domain model

Gain parameter:	Well damped system	Time domain model
$Kp_{c,c}$	1.0	0.2
$Ki_{c,c}$	3.0	1.0
$Kp_v$	3.0	0.3
$Ki_v$	0.5	4.0
$Kp_{c,m}$	1.5	0.3
$Ki_{c,m}$	3.5	6.0
$Kp_{sp}$	1.5	1.0
$Ki_{sp}$	2.5	8.0

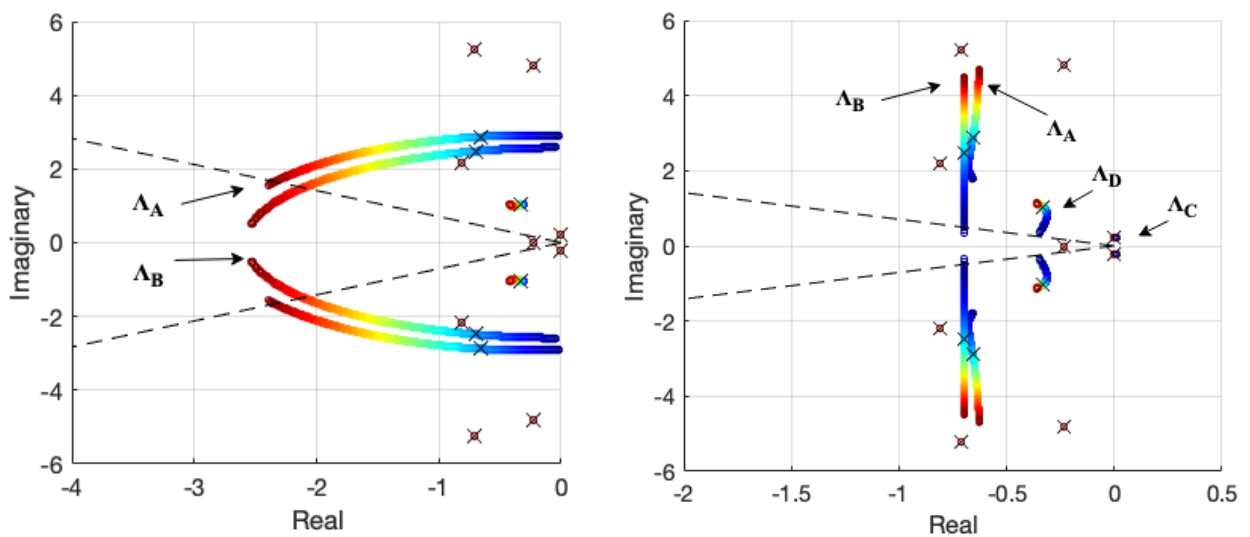
In this section, the tuning process of the models has been presented. The process has been a demonstration of how the pole placement and the use of PFs can be used as a tuning tool. It has been observed that the initial gains obtained from the tuning principles made the system over-sensitive, which resulted in instability. The gains of most significance were identified to be the gains in the outer loops. Remember that both these gains are depending on the choice of equivalent time delays, which are not accurately determined in this study. In order to obtain a similar magnitude for the computed gains as for the ones obtained through trial-and-error tuning in the time domain model, the equivalent time delays of the respective controllers need to be increased. Calculations based on the tuning expressions presented in chapter 6 shows that the equivalent gain used in the voltage controller has to be about twice as large. In the speed controller the equivalent delay needs to be increased with a factor of about 1000. This is considered as significant and should be noted. However, since an evaluation of the tuning concepts is not within the scope of this study, this observation will not be discussed any further. Ultimately, it has been seen that a set of parameters referred to as the "base case parameters" ensures stable operation in both respective models. Thus the stability of the system is considered to be verified.

## 7.2 Sensitivity analysis of the gain parameters

The aim of this section is to give an indication of how the different gain parameters in the respective controllers affect the system stability. The analysis is performed as a sensitivity analysis of the base case presented in the introductory section. Each gain parameter is changed separately, while the rest is fixed. The change in pole placement is tracked for the gains in the respective controllers, where the smallest gains are represented by the blue coloured poles and the shadings towards dark red indicate an increase in controller gain. Moreover, the poles associated with the base case are marked with a cross for reference purposes. Note that the onboard system is assumed as infinitely strong ( $z_{th} = 0$ ) and the PLL is considered to be ideal. Hence, the unstable cases found are not related to the strength of the onboard system, neither the dynamics of the PLL. Through the study, all the pole pairs will be identified in terms of their relation to the state variables. Time domain simulations will be supporting the results where the system becomes unstable due to increasing gains.

### 7.2.1 Gains of VSC current controller

With the intention of isolating the impact of the different gain parameters in the VSC current controller, the proportional gain  $Kp_{c,c}$  and the integral gain  $Ki_{c,c}$  are separately evaluated within a certain range. The  $Kp_{c,c}$  gain is evaluated in the range between 0.014 and 4.29, while the  $Ki_{c,c}$  is evaluated from 1.01 to 4. The intervals have been selected based on the illustrative trajectories they provide.



(a) Pole trajectories for change in  $Kp_{c,c}$

(b) Pole trajectories for change in  $Ki_{c,c}$

**Figure 7.7:** Pole trajectories - Current controller VSC

The trajectories depicted in figure 7.7a indicate that there are two specific pole pairs affected by the change in  $Kp_{c,c}$ , referred to as  $\Lambda_A$  and  $\Lambda_B$ . Clearly, an increase in  $Kp_{c,c}$  improves the damping of both pole pairs, ultimately making them move into the well-damped area. According to the PFs,  $\Lambda_A$  and  $\Lambda_B$  are closely related to the d-component and the q-component of the onboard current.

From the trajectories in figure 7.7b it can be seen that a variation in  $Ki_{c,c}$  results in a quite different characteristic. Based on the reference crosses of the base case,  $\Lambda_A$  and  $\Lambda_B$  are identified to oscillate with an increasing trend as the  $Ki_{c,c}$  increases. There is also observed movement in two other pole pairs, referred to as  $\Lambda_C$  and  $\Lambda_D$ , where  $\Lambda_C$  is the pair closest to the origin. The PFs indicate a similar relationship for  $\Lambda_A$  and  $\Lambda_B$  as seen for the  $Kp_{c,c}$ . Pole pair  $\Lambda_C$  and  $\Lambda_D$  is identified to be mainly related to the DC voltage at the topside terminal.

In both cases, there is a trend that the pole pair related to  $i_d$  is influenced by the states related to the DC-link and vice versa. Considering the power balance equation, where the d-component of the current controls the current flowing into DC-link, the correlation between  $i_{d1}$  and the states associated with the DC-link seems reasonable.

## 7.2.2 Gains of DC voltage controller

Similarly, the gains of the DC voltage controller are evaluated by changing them separately, while holding the rest fixed.  $Kp_v$  is evaluated in the range between 0.45 and 135, while  $Ki_v$  is evaluated from 0.5 to 300.

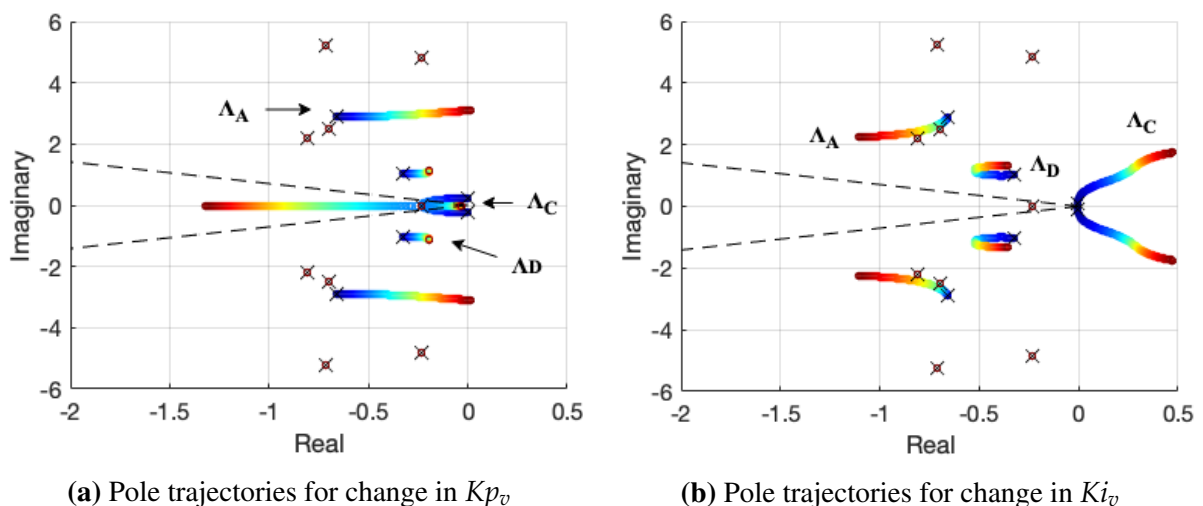


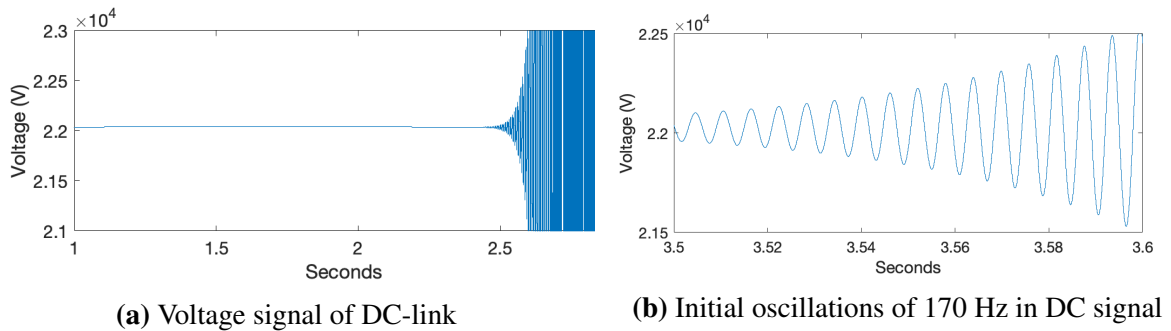
**Figure 7.8:** Pole trajectories - DC voltage controller VSC

As expected the trajectories in figure 7.8a indicate that an increase in the proportional gain  $Kp_v$  primarily affects the poles  $\Lambda_A$ ,  $\Lambda_C$  and  $\Lambda_D$ , which are associated with the active power balance

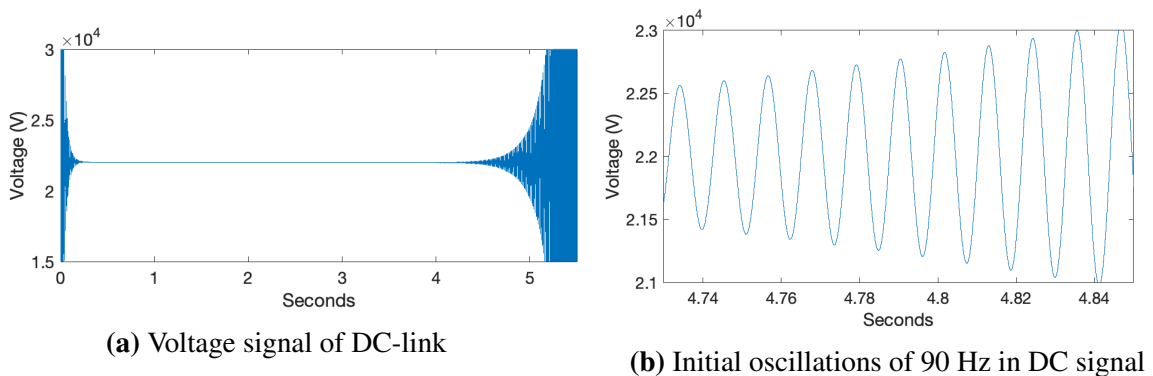
in the VSC. This is reasonable considering the cascade structure found in the controller. As  $Kp_v$  increases  $\Lambda_A$  becomes more oscillatory, which ultimately results in an unstable system. The cross over is identified at a  $Kp_v$  of 130. There is also movement in  $\Lambda_C$ , however the pole pair does not contribute to instability.  $\Lambda_D$  is observed moving towards the unstable region without having a significant impact.

Figure 7.8b indicates that a change in the integral gain  $Ki_v$  mainly has an impact on pole pair  $\Lambda_C$ , which becomes unstable as the gain increases. The cross-over is identified to occur at a  $Kp_v$  of 6. According to the PFs, the contribution from the state variables are essentially the same as observed in the case of the current controller.

The same test is performed in the time-domain model. Figure 7.9a shows that the system becomes unstable at a  $Kp_v$  of 15. In figure 7.9b the initial oscillations in the DC voltage signal is displayed, measured to have a frequency of 170 Hz. In terms of the integral gain, the domain model becomes unstable when  $Ki_v$  is increased to 900. The signal displayed in 7.10b is measured to oscillate at a frequency of 90 Hz. Considering the pole trajectories in 7.8, the two observed oscillations were expected to coincide with the computed initial frequencies of  $\Lambda_A$  and  $\Lambda_C$  given in 7.6, at respectively 23 Hz and 1.7 Hz.



**Figure 7.9:** DC voltage at a  $Kp_v$  of 15



**Figure 7.10:** DC voltage at a  $Ki_v$  of 900

### 7.2.3 Gains of VSD current controller

In this case, the impact of the gain parameters of the VSD current controller in the drive will be evaluated. The  $Kp_m$  gain will be evaluated in the range between 0.007 and 2.0, while  $Ki_m$  will range between 0.05 and 15.

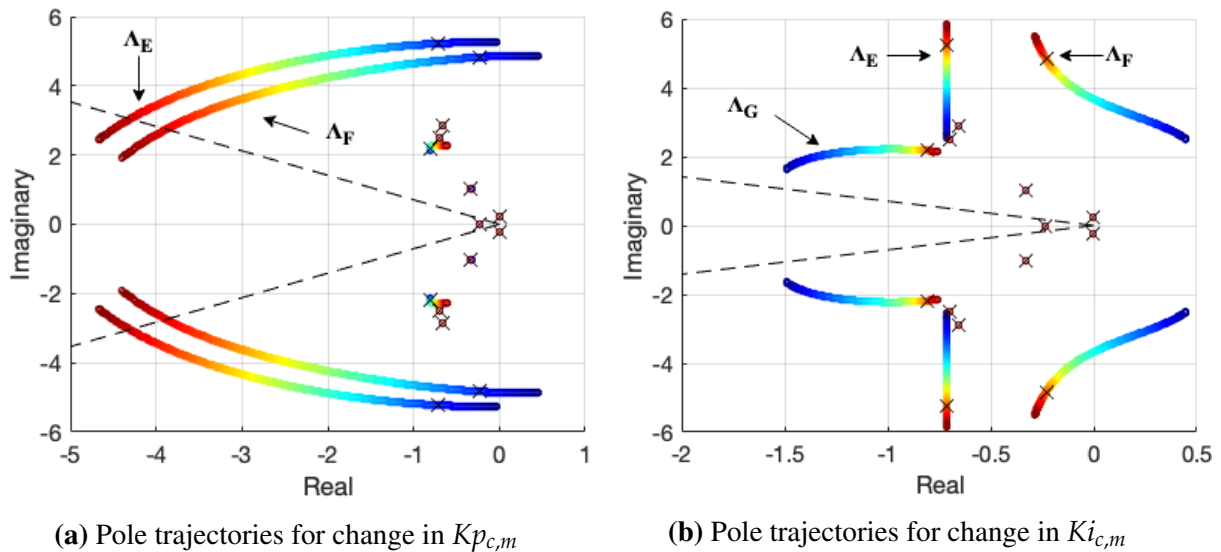


**Figure 7.11:** Pole trajectories - Current controller VSD

The trajectories in figure 7.11a show similar behaviour as observed for the current controller of the VSC. There are also, in this case, two pole pairs affected by the change in gain. They will be referred to as  $\Lambda_E$  and  $\Lambda_F$ . An increase in  $Kp_{c,m}$  has a mitigating effect on the two pole pairs, moving them into the well-damped area. The moving poles are mainly associated with the d and q-component of the stator current of the machine, where  $\Lambda_E$  and  $\Lambda_F$  is related to  $i_{d2}$  and  $\Lambda_{q2}$  respectively.  $\Lambda_F$  has also some contribution from the state variables related to the speed of the machine,  $n_{mech}$  and  $\xi_{sp}$ . Since the error in speed is used as torque reference and the q-component of the current is controlling the torque of the machine, this relationship is expected.

Figure 7.11b shows the trajectories for a changing  $Ki_m$ . It can be observed that  $\Lambda_F$  is located in the unstable region when the gain is low. As the gain increases the  $\Lambda_F$  is moved into the stable region. A pole pair not yet identified is also moving, referred to as  $\Lambda_G$ . According to the PFs  $\Lambda_G$  can be related to the mechanical speed of the machine. Considering the stable region, an increasing  $Ki_v$  seems to intensify the oscillations in state variables of the machine.

### 7.2.4 Speed controller

In order to evaluate the impact of the speed controller the proportional gain  $Kp_{sp}$  is changed in the range between 0.008 and 2.4, while  $Ki_{sp}$  is changed between 0.13 and 15.

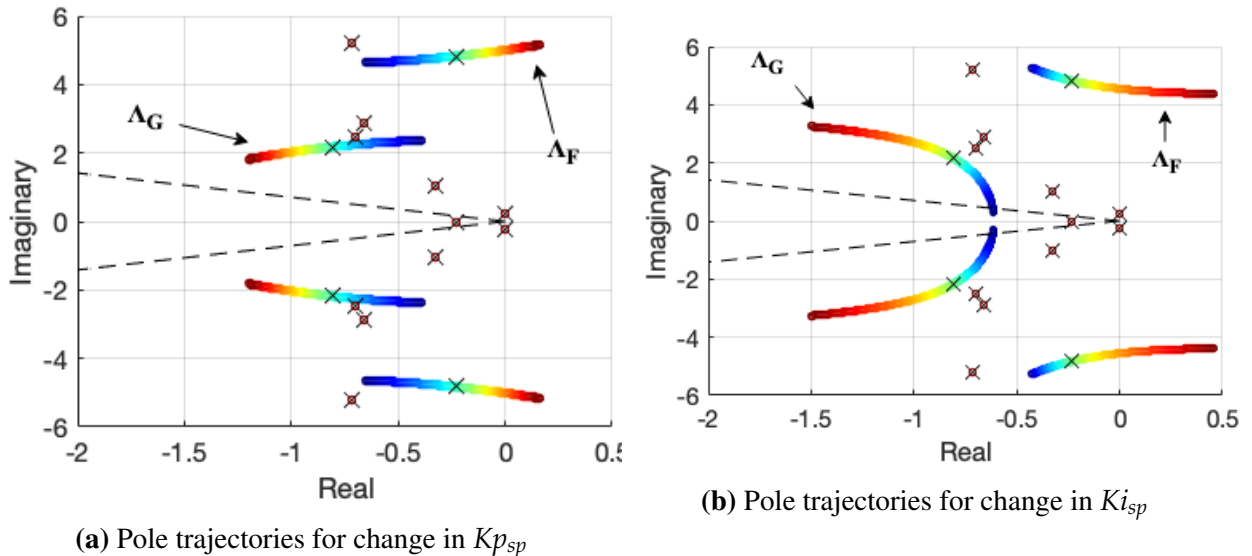


**Figure 7.12:** Pole trajectories - Speed controller VSD

As expected, the trajectories in figure 7.12a show that the change in proportional gain  $Kp_{sp}$  mainly affects  $\Lambda_F$  and  $\Lambda_G$ , which are related to the torque generating current and the speed of the machine. As the  $Kp_{sp}$  rises,  $\Lambda_F$  moves towards the unstable region and will dominate the stabilizing effect of  $\Lambda_G$ . The system becomes unstable when  $Kp_{sp}$  is 1.7.

The trajectories in figure 7.12b indicate an almost identical trend as seen for the proportional gain. An increase in the integral gain makes  $\Lambda_F$  move rightwards, ultimately making the system unstable. The cross over is detected to occur at a  $Ki_{sp}$  of about 12.

The same study performed in the time domain model results in a critical  $Kp_{sp}$  of 35. As displayed in 7.13 the signal distortion is of a character where no oscillation frequency can be determined. Figure 7.14b shows the DC link voltage when the  $Ki_{sp}$  is increased to 70. The initial oscillation in figure 7.14b is identified to be 90 Hz. The frequency was expected to coincide with the initial frequency computed for  $\Lambda_F$  at 20 Hz.

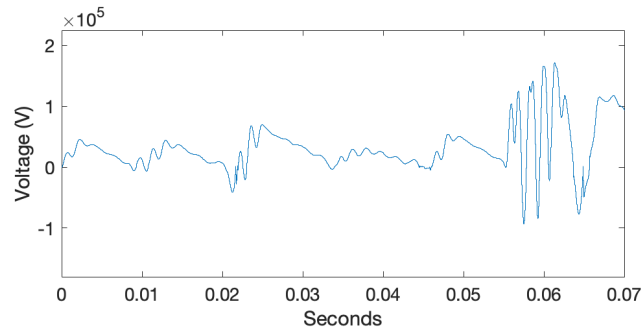


**Figure 7.13:** Voltage signal of DC-link with at a  $Kp_{sp}$  of 35

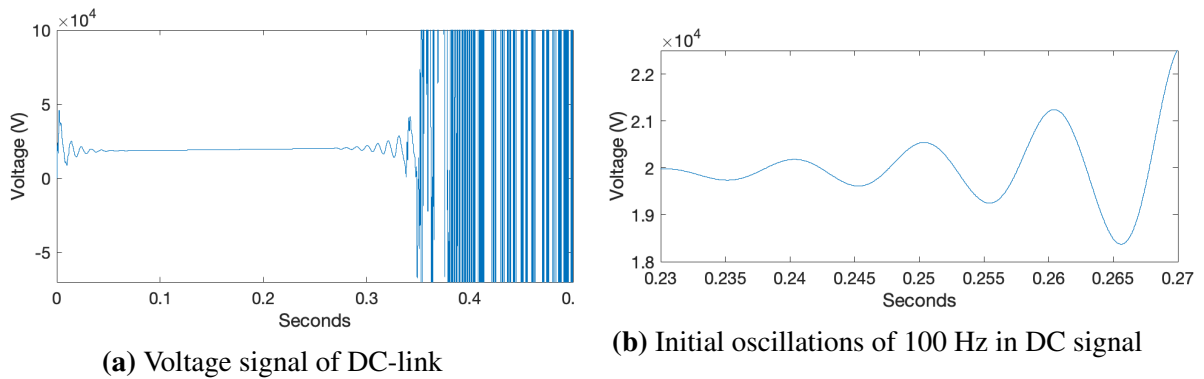


**Figure 7.14:**  $Ki_{sp}$  of 70

## 7.2.5 Observations

In this section, the different controller gains have been evaluated separately in order to identify their impact on the system stability. Some general observations can be made:

- A general observation made from the trajectories of the current controllers is the mitigating effect of the proportional gain and the increased oscillating behaviour introduced by the integral gain. The observed phenomenon can be supported by the error accumulation in the integral gain. Even though the error is zero, the integrator could still be influenced by the error history and thus amplify the system. Another observation is that none of the gains in the current controller contributes significantly in moving the poles rightwards as the gains increase. Based on the assumption that a fast-acting controller is desirable, it might be proposed that the gains of the current controllers are of less importance when analyzing the system stability.
- The trajectories obtained for the outer loops show that both gains are capable of moving the system into instability. In the DC voltage controller, the results indicate that the system is notably sensitive to increments in the integral gain  $Ki_v$ , making the system unstable at fairly low gain values. Consequently, making the DC-link prone to instability. Yet, the time domain model indicates the system to be noteworthy more tolerant to gain change in the outer loops.



- A general observation for all the gain parameters in the VSD is their lack of impact on the state variables of to the DC-link. According to the PFs the only gain with a significant contribution to the DC stability, are the gains related to the DC voltage controller. Based on these results a simplification of the sub-sea load system can be proposed when the stability of the DC link is investigated.
- The majority of the results provided in this section coincide well with how the different controller gains are expected to influence the system. Yet, there is also observed a discrepancy between the results obtained from the two models. The root cause of the discrepancy is discussed at the end of the chapter.

### 7.3 Analysis of the cable resonance

The cable supplying the sub-sea system is the only part of the system containing a resonant circuit. Thus, the resonance frequency of the cable needs to be determined. Remember that the cable supplying the sub-sea system is a bi-polar link, meaning that the equivalent reactive components seen from the source side are twice as big compared to a monopolar link. The resonance frequency of a bipolar link becomes,

$$f_0 = \frac{1}{2\pi \sqrt{L_L \frac{C_{eq}}{2} \cdot 2}} \quad (7.1)$$

From the expression above the resonance frequency of the DC-link is determined to be 517 Hz. For further verification, an impedance-frequency plot has been obtained from the time domain model. Figure 7.15 shows that the impedance spikes at a frequency of 518 Hz. The resonance frequency is considered to be in a frequency range possibly easily excitable by the system, due to the many fast-acting components in the system.

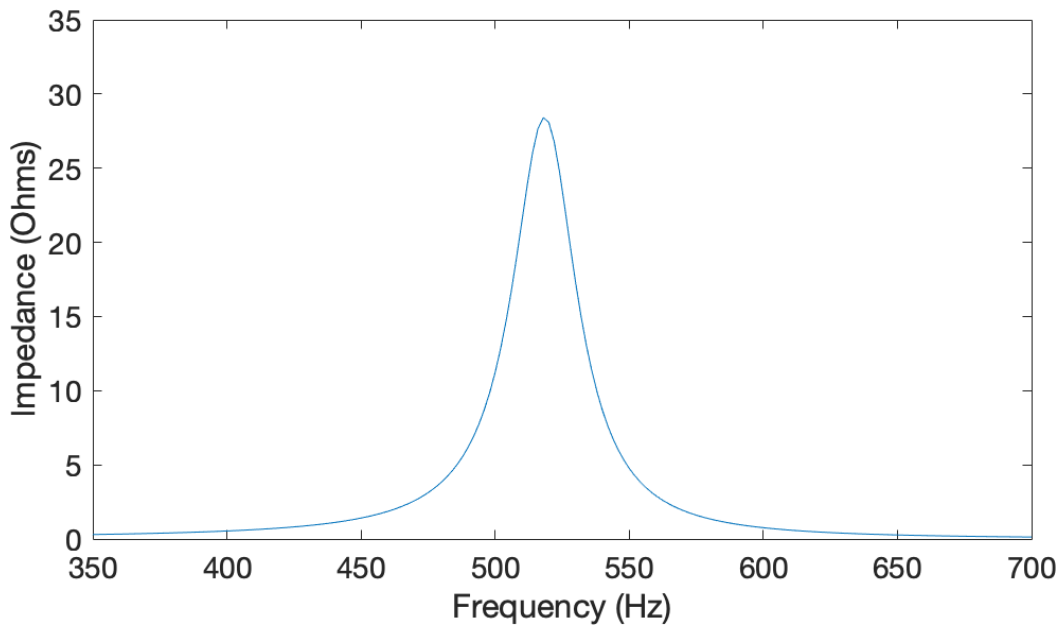


**Figure 7.15:** Impedance-frequency plot of the DC link

## 7.4 Finite strength of onboard system

So far the onboard system has been assumed infinitely strong. As the AC system of the vessel is an isolated system, where the system loads are large compared to the size and number of generating units, the system is likely to be categorized as weak. In this section, the impact of the strength of the onboard system is evaluated. In order to identify the impact of the system strength, the SCR is changed within a certain range. This is accomplished by varying the Thevenin impedance of the onboard system with different X/R ratios. The participation factor tables used in this section can be located in appendix D.

### 7.4.1 SCR with an X/R ratio of 1

The trajectories in figure 7.16 are obtained by changing the SCR ratio of the onboard grid in a range between 47 and 0.47. In this case, a unity X/R ratio is selected. Figure 7.16 shows four pole pairs being affected by the change in SCR, but only  $\Lambda_A$  and  $\Lambda_C$  are considered as dominant. From previous studies,  $\Lambda_A$  is recognized to be related to the d-component of the current, while  $\Lambda_C$  is related to the DC voltage and the DC voltage regulation of the VSC.

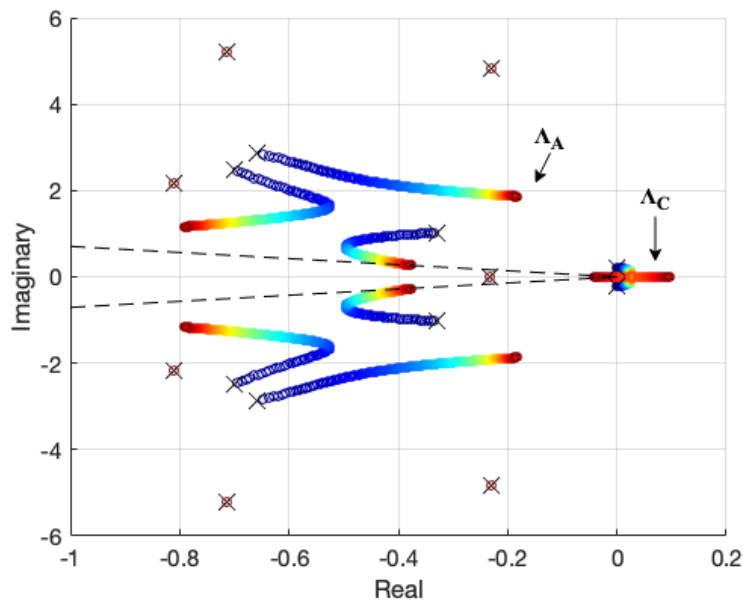


**Figure 7.16:** Pole trajectories for change in SCR between 47 and 0.47 with an X/R ratio of 1

By observing the trajectories made by  $\Lambda_A$  and  $\Lambda_C$ , it becomes clear that the reduction of the SCR has a destabilizing effect on the system, making  $\Lambda_C$  move into the unstable region.  $\Lambda_C$  is identified to become unstable at an SCR of 14.

The same analysis has also been performed in the time-domain model. Here the critical SCR has been detected to be in the range between 3 and 2.8. The stable and the unstable signals are respectively displayed in figure 7.17 and 7.18. Figure 7.18c shows the initial oscillation observed in the DC voltage signal. Measurements indicate an oscillation frequency of 580 Hz.

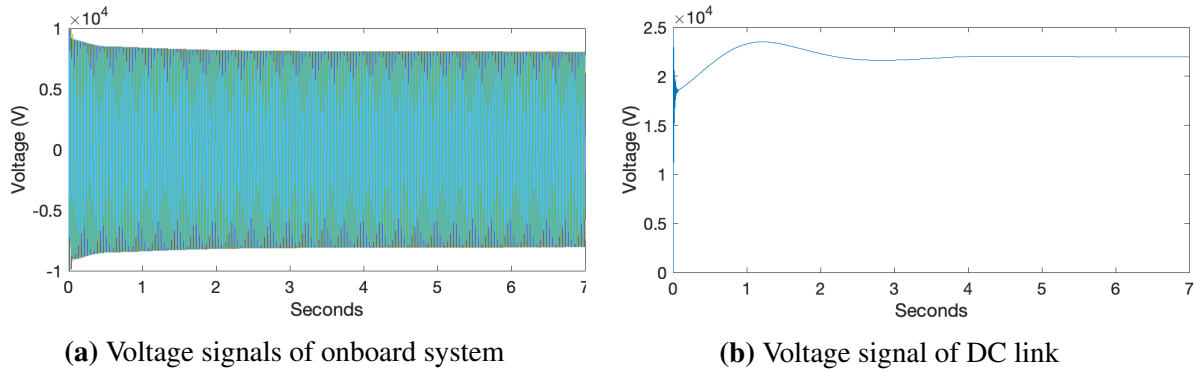


**Figure 7.17:** Voltage signals with a SCR of 3

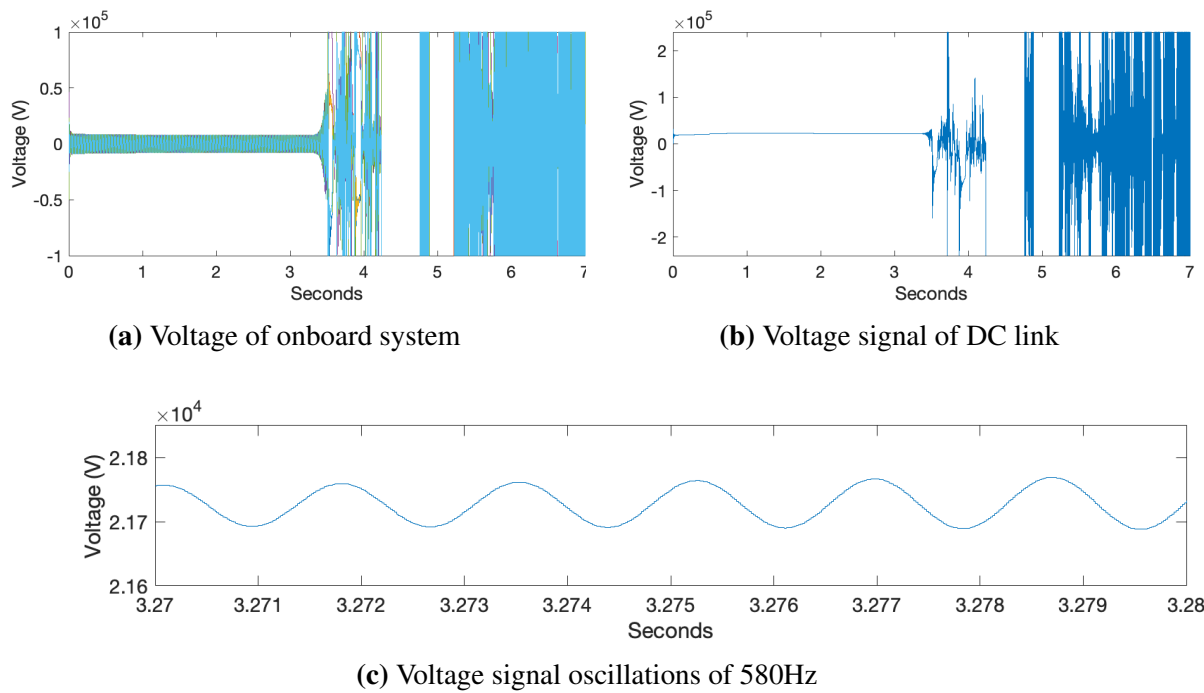


**Figure 7.18:** Initial voltage oscillations with a SCR of 2.8

### 7.4.2 SCR with an X/R ratio of 0.2

A similar operation is performed with an X/R ratio of 0.2. The trajectories in figure 7.19 are obtained by changing SCR in the range between 40 and 1.

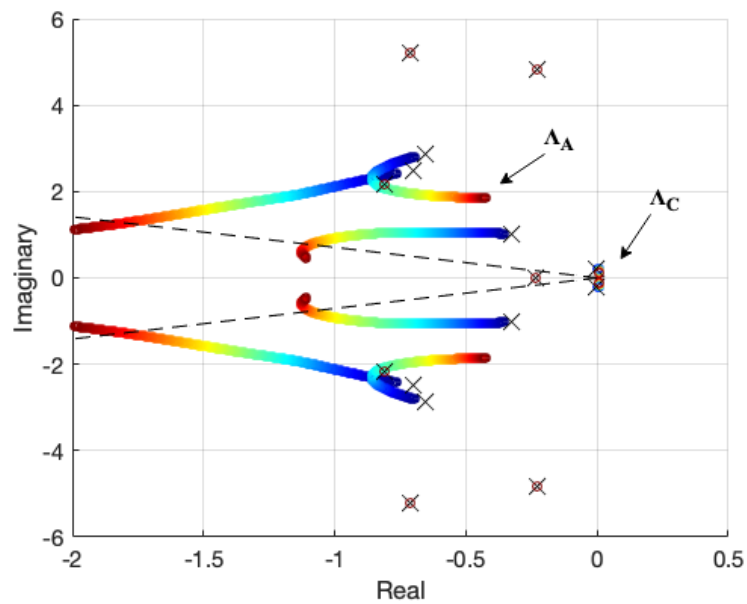
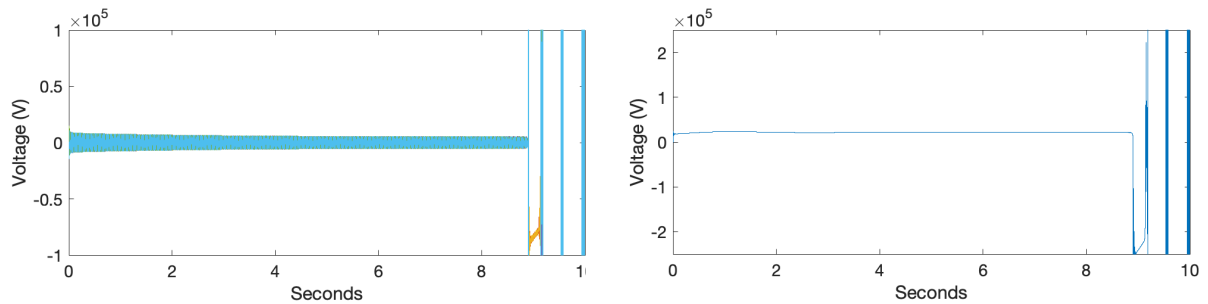


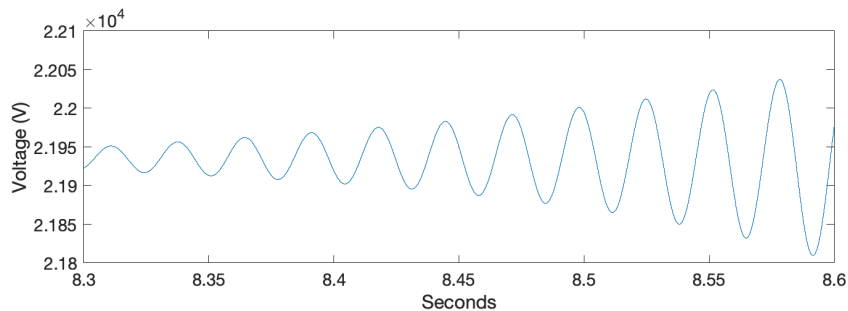
**Figure 7.19:** Pole trajectories for change in SCR between 40 and 1 at with an X/R ratio of 0.2

The trajectories (figure 7.19) show a similar trend as observed with unity X/R ratio, where  $\Lambda_C$  is the pole pair causing the system to become unstable. The instability is identified to occur at an SCR of 14.  $\Lambda_A$  and  $\Lambda_C$  are strongly associated with state variables of the DC-link as the system becomes unstable. In order to support the results, a time domain simulation is performed. The simulation results for the respective terminal voltages of VSC is displayed in 7.21.



**(a)** Voltage signals of onboard system

**(b)** Voltage signal of DC link



**(a)** Voltage signal oscillations of 36 Hz

**Figure 7.21:** Voltage signals with an SCR of 2

The oscillating behaviour of the signals occurs when the SCR of the time-domain model is close to 2. This is significantly lower than what was observed for the unity X/R ratio, which implies a much less sensitive system. In this case, the initial oscillations have been measured at a frequency of 36Hz.

### 7.4.3 SCR with an X/R ratio of 5

In the last case, the X/R ratio is increased to 5, which means the inductive part now becomes more significant. The trajectories in 7.22 are obtained by ranging the SCR from 50 to 0.1.

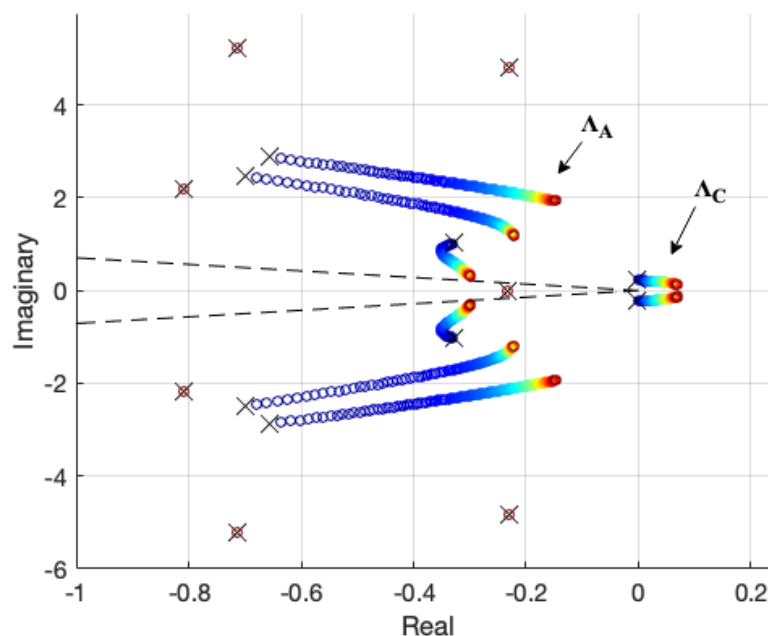


**Figure 7.22:** Pole trajectories for change in SCR between 50 and 0.1 at with an X/R ratio of 5

In this case  $\Lambda_C$  becomes unstable at an SCR of 13, which is approximately the same as identified for the two other cases. Compared to the case with a higher resistive share, it can be observed that all trajectories move rightwards. The higher inductive share of  $z_{th}$  seemingly have a destabilizing effect all the involved poles.

Like the previous cases, a time-domain simulation is conducted. The signals displayed in figure 7.23 are identified to become unstable at an SCR of 4.7. Figure 7.24 shows the initial voltage oscillation, which is measured to be 590 Hz.

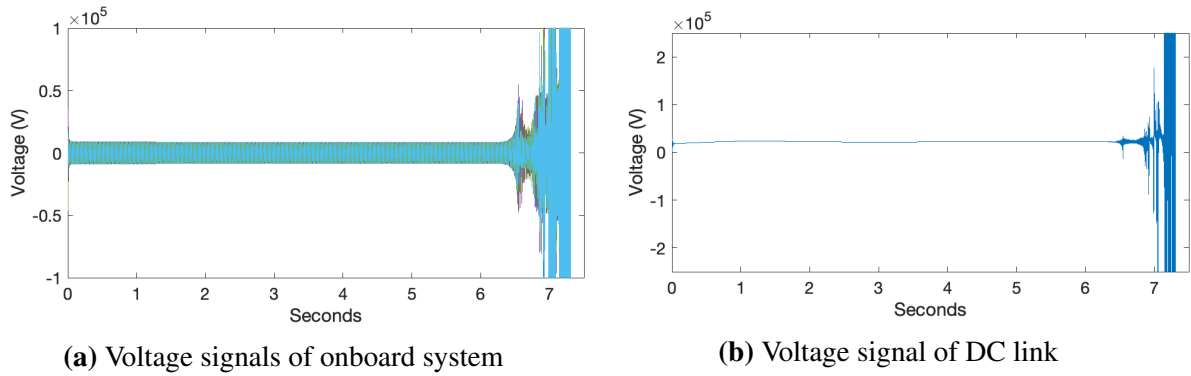


**Figure 7.23:** SCR 4.7 - DC voltage instability event

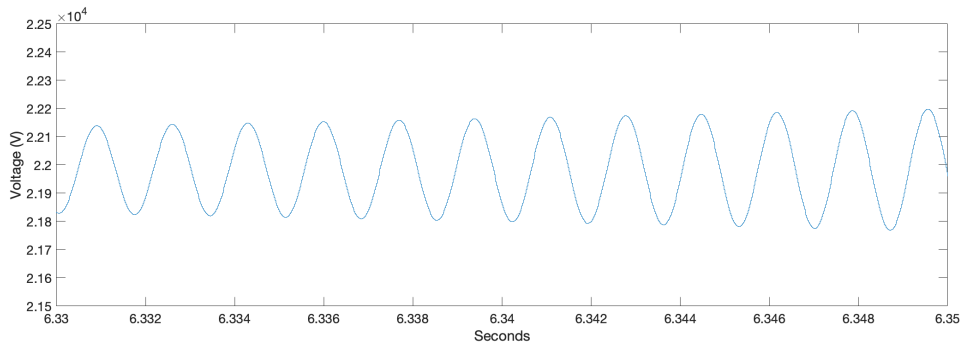


**Figure 7.24:** SCR 4.7 - Voltage signal oscillations of 590Hz

#### 7.4.4 Observations

Based on the three case studies performed in this section, some general observations can be made:

- Based on the results from the linearized model, the destabilization of the DC-link is not related to the  $X/R$  ratio of the onboard system, rather the magnitude of the equivalent impedance. However, this contradicts the results from the time-domain model, where there is a clear trend between the  $X/R$  ratio and the critical SCR. Another observation made is that the critical SCR obtained from the linearized model seems unreasonably large. The results from the linearized model cannot be considered as reliable in this test.
- In the time domain model, it has been observed that a low  $X/R$  ratio has a stabilizing effect on the system. Contrarily, a mainly  $X/R$  ratio seems to have a destabilizing effect, making the system more sensitive to the weakness of the grid. The result is found reasonable due to the damping provided by the resistance in  $Z_{th}$ .
- Under large  $X/R$  ratios conditions, an initial frequency of 580 Hz and 590 Hz has been identified. However, at low  $X/R$  ratios, a lower oscillation at 36 Hz has been identified. Considering the shape of the frequency impedance-frequency plot in figure 7.15, a direct correlation with the DC-link cannot be established.

## 7.5 System stability with PLL dynamics

As the system no longer is infinitely strong, the PLL can no longer be considered as ideal. As introduced in chapter 6 the PLL provides the reference angle for the dq0 transformation used in the grid-connected VSC. This is achieved by using a PI controller to track the phase angle of the grid voltage vector. The controller introduces additional dynamics in the system. In this section, the impact of introducing the dynamics of the PLL will be investigated in the linearized model. A sensitivity analysis of the gain parameters of the PI controller will be performed.

The PLL is introduced by including the dynamic expressions given in section 6.4.2 and replace the actual angular velocity  $\omega_s$  with the estimated angular velocity  $\omega_{pll}$  into the current controller of the VSC. Moreover, in order to obtain  $v_g^q$ , the AC side is split into two sections, as illustrated in 6.3. In total this will introduce six additional states. How the dynamics of the PLL affect the dq0 transformation will not be considered in this study.

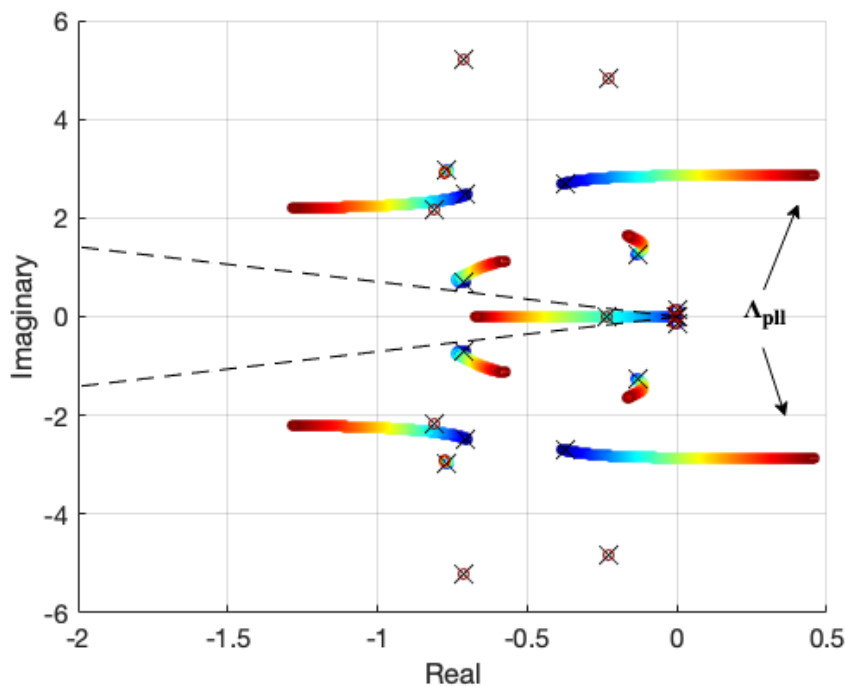


**Figure 7.25:** Pole plot of system with bandwidth  $a_{PLL}$  ranging from 0.04 to 36 at a SCR of 2.5

The plot in figure 7.25 is obtained by changing the bandwidth  $a_{pll}$  from 0.04 to 12 at an SCR of 2.5. As the gain increases it can be seen that one of the pole pairs moves into the unstable region. This pole pair will be referred to as  $\Lambda_{pll}$ . The cross over into the unstable region is detected to occur at a bandwidth  $a_{pll}$  of 10.7. According to the corresponding PFs <sup>2</sup>,  $\Lambda_{pll}$  is

<sup>2</sup>The participation factors can be located in appendix D



mainly associated with state variable  $v_g^q$ ,  $\omega_{pll}$  and  $\xi_{pll}$ . Recall that  $v_g^q$  is used as a substitute for the input error  $\Delta v_g^d$  in small-signal analysis. As expected, all associated states are related to the operation of the PLL. In order to identify the significance of the contribution from the onboard system, the same analysis is performed with an SCR of 5 and an SCR of 0.5.

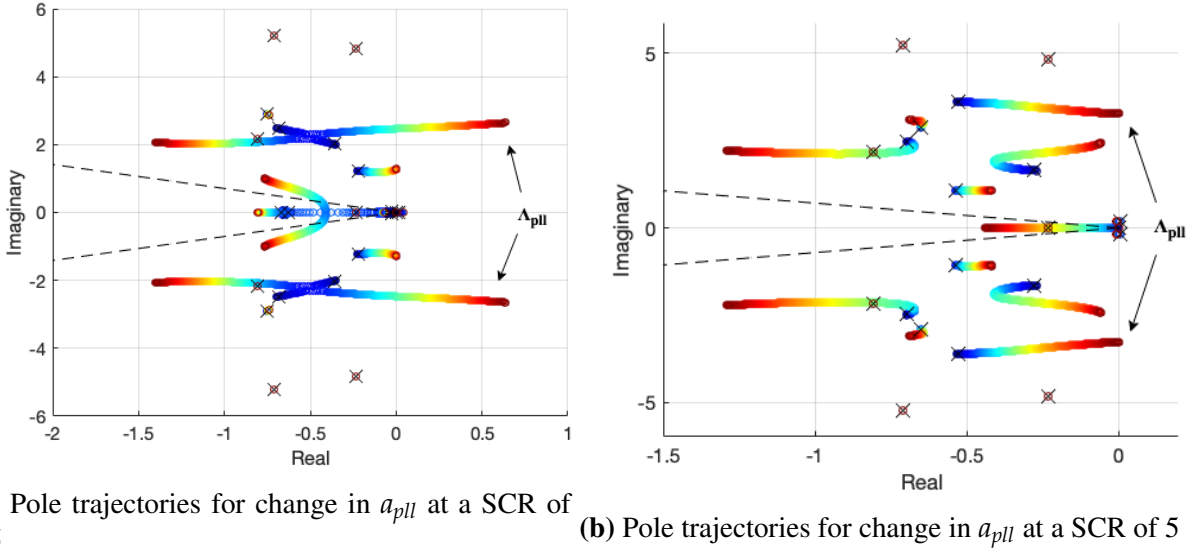


**Figure 7.26:** Pole trajectories of  $\Lambda_{pll}$  at different SCR

From figure 7.26a it can be observed that the reduction in SCR moves  $\Lambda_{pll}$  into the unstable region at an earlier stage. When the grid is weaker (SCR=0.5) the system becomes unstable already at a bandwidth of  $\alpha = 7.68\text{Hz}$ . Contrarily, when the SCR is increased, implying a stronger grid,  $\Lambda_{pll}$  is kept within the stable region at all tested SCR values. The results imply that the strength of the onboard grid plays a significant role in the gain sensitivity of the PLL. As previously stated the PLL can be considered as ideal when the grid is assumed infinitely strong. However, when the grid is weaker, the PLL is subjected to a larger variation in grid voltage. Based on the obtained results, such variations requires the bandwidth of the PLL to be reduced in order to maintain stable operation.

It can be noted that the weakness of the grid is also related to the stability of the frequency, which again is related to the inertia in the system. However, since the dynamics of the onboard generating unit is disregarded, this will not be affecting the stability picture in this study.

## 7.6 Study of maximum power transfer capability

The aim of this section is to analyze how the loading level impacts the stability of the system. The study will be performed by increasing the mechanical load of the machine gradually until instability occurs. The intention of this approach is to identify the maximum power transfer capability of the system. Firstly, in order to identify the impact of the strength of the onboard grid, the study will be performed under three different SCR conditions. Secondly, a test will be performed to identify the contribution from the sub-sea induction motor and drive, the DC-link and the topside system (onboard system and VSC) respectively. The tests are conducted by replacing the sections with an ideal equivalent. In order to identify the contribution of the machine, the cable impedance is removed, essentially making an ideal cable. The test of the cable is performed by replacing the machine and the drive with a controllable DC current source. Finally, the test of the onboard system is conducted by replacing the onboard grid and the VSC with an ideal DC voltage source. An SCR of 5 is selected for the cases considering the onboard system.

In the first case, the onboard grid is considered as strong, represented by an SCR of 10. Figure 7.27a shows that under these conditions the instability occurs when the loading level reaches about 13.3 MW. From the close-up picture of the signal displayed in 7.27b, the initial oscillation of the power signal has been measured to have a frequency of 83 Hz.

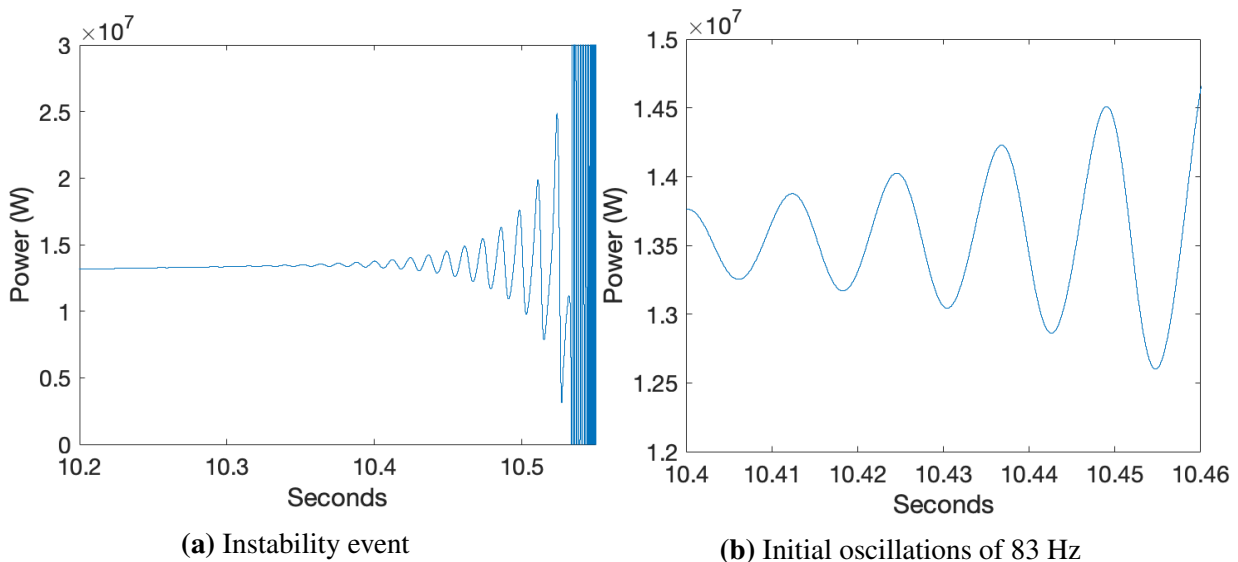


**Figure 7.27:** Maximum power transfer capability of DC-link at a SCR of 10

In the second case, the strength of the grid has been reduced, represented by an SCR of 5. Figure 7.28a shows that the system becomes unstable at a loading level of 10.7 MW. The initial oscillation of the power signal given in figure 7.28b has been measured at a frequency of 590 Hz.

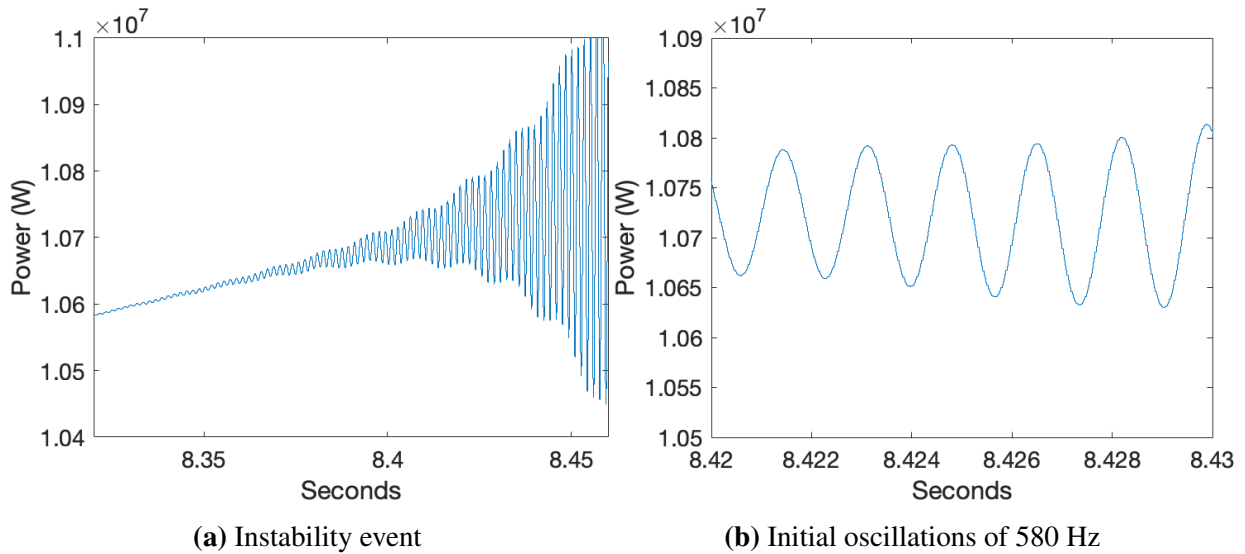


**Figure 7.28:** Maximum power transfer capability of DC-link at a SCR of 5

In the third case, the strength of the grid is reduced even further, represented with an SCR of 2.5. Figure 7.29a indicates that the system gets unstable at a loading level of about 5 MW. From the close-up picture of the signal in figure 7.29b the oscillating frequency of the power signal has been measured to be around 580 Hz.

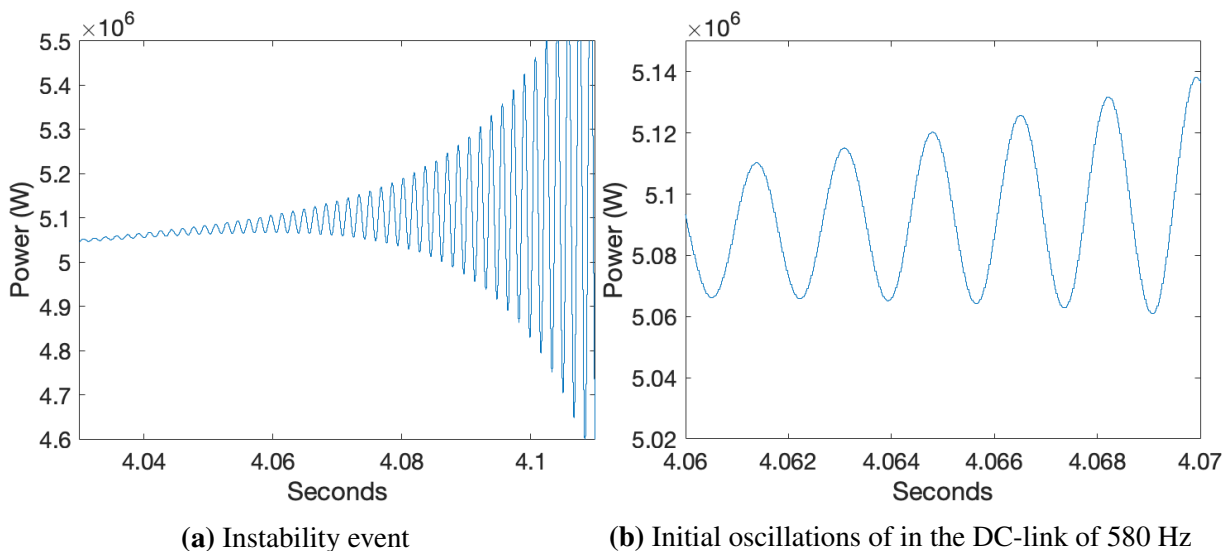


**Figure 7.29:** Maximum power transfer capability of DC-link at a SCR of 2.5

Furthermore, a case study of the contribution from the cable, the induction machine and the onboard system respectively is performed. The signal in figure 7.31 shows that a system with an ideal DC-link cause the system to become unstable at a loading level of 10.8 MW. In this

case, the oscillating frequency has been measured to be 75 Hz.

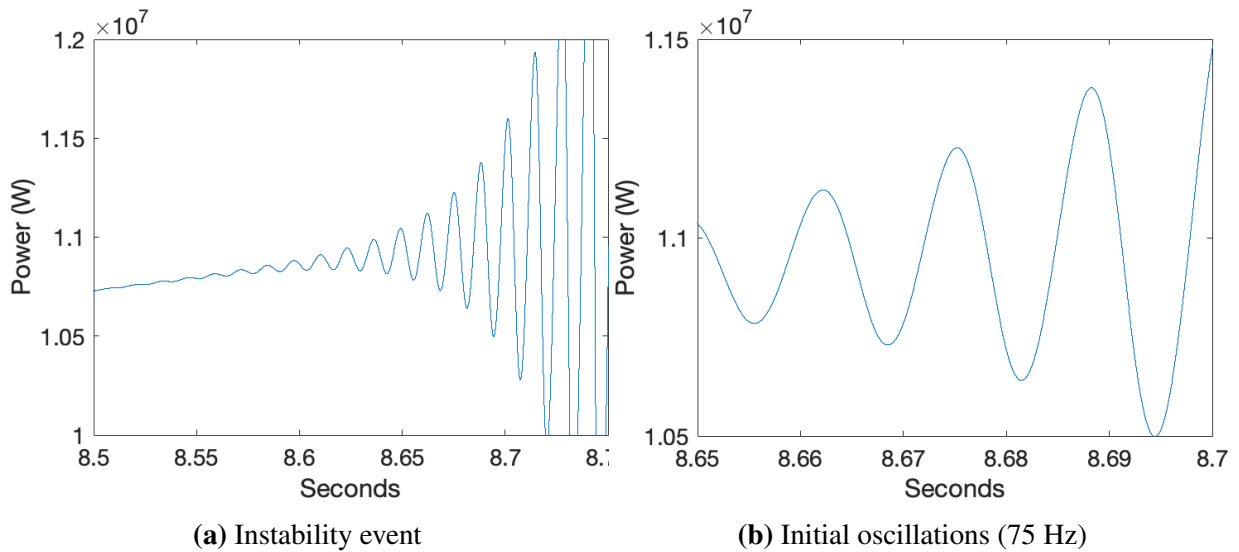


**Figure 7.31:** Power signal excluding dynamics of DC-link

The signal in 7.33 is the result of neglecting the dynamics of the induction machine and the drive. The maximum power transfer capability is observed to be approximately 14.5 MW. In this case, the signal oscillations are identified to be 110 Hz.

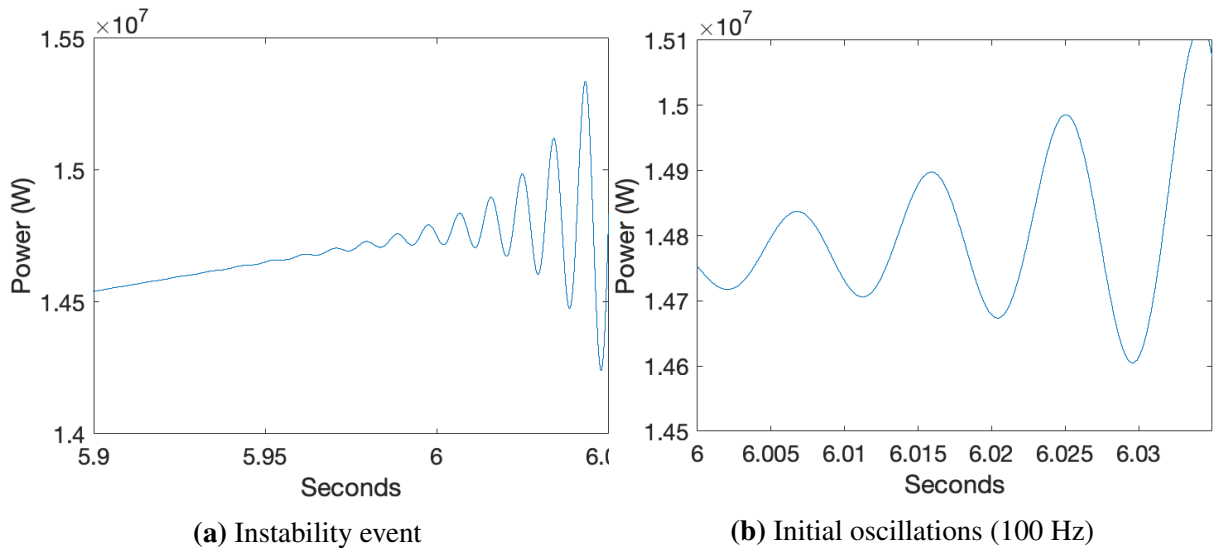


**Figure 7.33:** Power signal excluding dynamics of drive and induction machine

Finally, the signal in 7.35 is the result of excluding the dynamics of the onboard system and the VSC. Here the maximum power transfer capability is observed at 10 MW, with a power signal oscillating at a frequency of 360 Hz.

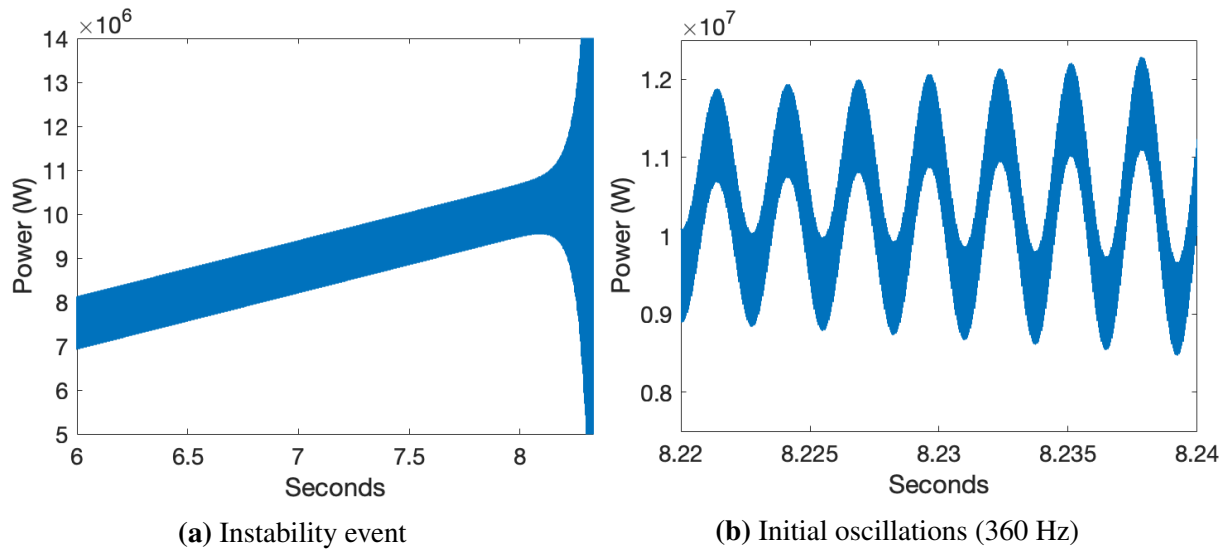


**Figure 7.35:** Power signal excluding dynamics of the onboard system and the VSC

### 7.6.1 Observations

- Based on the cases analyzed in this section a clear relationship between the maximum power transfer capability and the SCR of the onboard grid has been detected.
- The removal of the dynamics associated with the DC-link showed no impact on the maximum power transfer capability, where the critical loading level remained at 10.8 MW.
- The removal of the dynamics related to the induction machine showed a noteworthy increase in the maximum power transfer capability and resulted in an initial frequency of 110 Hz. Remember that the resonance frequency of the DC-link was determined to be 518 Hz. As the oscillations are way smaller than the resonance frequency of the cable, a correlation to the DC-link cannot be established.
- The removal of the dynamics of the onboard system and the VSC showed no significant impact on the power transfer capability.

## 7.7 Discussion

The stability analysis performed in this chapter has revealed that the weakness of the grid has a significant impact on the stability limits of the system. As the strength of the onboard system is reduced the power transfer capability deteriorates. It has been observed that when the SCR ratio is reduced to 2, the system will no longer be capable of accommodating the power demand of the SSLP at 7.8 MW. Considering the power demand from the whole DSM system at 12.8 MW, even a strong system, with an SCR of 5, will have difficulties in maintaining a stable system. Under these weak system conditions seemingly simple load changes or faults might trigger instability. Hence, in the design process of a DSM system, an adequately strong onboard system will be of uppermost importance.

By neglecting the dynamics of induction machine, the power transfer capability of the system was observed to be enhanced significantly. The results imply that the drive has a destabilizing effect on the system. The root cause of this destabilizing effect is yet not completely clarified. However, it is reason to believe that the constant power load behaviour of the drive reduces the power stability limit. Due to time restrictions, this has not yet been confirmed through simulations. In a modelling perspective, the results indicate that a simplification of the sub-sea load system cannot be performed without compromising the accuracy of the stability analysis.

It should be noted that none of the observed oscillating frequencies coincide with the resonance frequency of the DC-link, thus cable resonance is not identified as a stability issue. Moreover, there was no noteworthy impact on the maximum power transfer capability in the case with an ideal DC-link. Thus, no clear correlation to the DC-link dynamics have been identified.

Even the highest frequencies observed in this analysis is considered to be in a range which is easily excitable by the system. Low-frequency oscillations can be critical to the system due to the similar frequencies as what is found during stable conditions. Undesirable oscillations in the system might therefore be difficult to detect. The root cause of the oscillations will be needed in order to suggest appropriate mitigating measures in the system.

The stability analysis has revealed that the results provided by the linearized model and the time-domain model are not fully consistent. The time-domain model is easily verified and is considered as reliable. The linearized model seems to be highly sensitive to changes in SCRs. Yet, the variation in X/R ratios does not show any significant impact on the critical SCR. Thus, it might be reason to believe that system dynamics are of such a non-linear character that the linearized model is unable to capture the dynamic behaviour sufficiently. Yet, similar studies of HVDC systems performed in [43] and [43] show that the non-linearities introduced by con-

verters normally are small. Non-linearities are hence not considered to be the root cause of the discrepancy. Inaccuracies in the modelling also need to be addressed as a cause. From participation factor tables obtained for the test cases in section 7.2, an expected correlation between the controller gains and the affected state variables was found. This was also observed in the participation factors obtained in section 7.4, where the contribution from the state variables on the moving poles was as expected, considering the change in parameters. The structure of the linearized model therefore seems correct. A broad mapping of the discrepancy has not yet been conducted, which makes the cause incompletely understood. Despite the discrepancy in the models, the analysis performed in 7.2, 7.5 and 7.4 are considered as a proper demonstration of the methodology using pole trajectories and participation factors.

# Chapter 8

## Conclusion and further work

### 8.1 Concluding remarks

The deep sea is expected to hide locations with massive mineral deposits rich in rare minerals, such as gold, silver, copper and cobalt. Numerous locations have been discovered along Mohn's ridge between Svalbard and Jan Mayen, where Loki's castle at 2400 meters depth has been recognized as one of the most promising locations for the extraction of minerals.

This thesis has investigated different stability aspects of a power system designed for deep-sea mining applications in Norwegian territories. Existing deep-sea mining production concepts have been presented and R&D on the field has been discussed. Based on available literature a system design for operation in Norwegian waters has been proposed. The proposed system is designed for operation at sites located at depths similar to Loki's Castle in the Norwegian Sea, and a production system, inspired by the one developed by the company Nautilus Minerals, is applied. Due to the power requirements associated with mining operations at such depths, a DC distributed system with a centralized submersed power hub is proposed. A time-domain model and a linearized model for small-signal stability analysis have been developed in a MATLAB/SIMULINK environment for stability analysis purposes. For the sake of decreasing system complexity a simplification of the onboard system and the sub-sea system has been applied, where the onboard system is replaced with a Thevenin equivalent and the sub-sea system is represented by the most dominant load (the SSLP). The final model configuration is a point-to-point DC-link supplying a variable speed drive connected to a large induction machine, where a rotor flux oriented machine model has been applied.

The stability analysis has shown that instability is determined by the magnitude of power transfer and the characteristics of the AC system. As the strength of the onboard system is reduced the power transfer capability deteriorates, ultimately making the system incapable of providing



the required power. High X/R ratios of the onboard equivalent impedance have been recognized to have a destabilizing effect on the system, implying a system more sensitive to disturbances. The initial oscillations of the instability events have been documented, yet without investigating the root source of the phenomenon.

---

## 8.2 Future work

First of all, a further investigation of the discrepancy between the two models is encouraged.

To the best of author's knowledge, one of the main contributions of this thesis has been the identification of a number of low-frequency oscillations related to unstable events. The oscillations are considered to be easily excitable by the system and might pose a significant threat to the stability of the system. Yet, the mechanisms that trigger this poor performance has not been clearly identified. The development of a SISO (signal in-signal out) model of the system is proposed as a next step in the process. The advantage of this method that it allows the system to be divided into several subsystems in a transfer function form, consequently making it possible to detect their individual impact on the system. The model will also provide additional verification of the two models developed in this thesis. The stability of the SISO model can be determined by applying the Nyquist stability criterion. A SISO approach, applied to an HVDC system in [43], can be used as a starting point. It has been detected that the impact of the PLL is strictly related to the strength of the grid. Since the weakness of the grid also is related to the stability of the frequency, an introduction of the dynamics of the onboard system should be considered.

Both models developed in this thesis can easily be augmented to a more complete representation of the system. As a first step in the augmentation of the models, a second machine can be connected to the DC link, representing the aggregated power demand of the SPTs. Introduction of time delays in the control systems and non-ideal measurements should also be considered, due to their potential impact on the system stability.

# Bibliography

- [1] J. Gjevre. Stability in power systems for deep sea mining applications. *Specialization project - NTNU*, 2018.
- [2] PWC. The Long View. How will the global economic order change by 2050. *Price Waterhouse and Coopers*, February(February):1–72, 2017.
- [3] United Nations. *World Economic Situation and prospect 2018*. United Nations, 2018.
- [4] H. Lin B.W. Schipper and R. Heijungs E. van der Voet M.A. Meloni, K. Wansleben. Estimating global copper demand until 2100 with regression and stock dynamics. *Resources, Conservation and Recycling*, 132(January):28–36, 2018. ISSN 18790658. doi: 10.1016/j.resconrec.2018.01.004. URL <https://doi.org/10.1016/j.resconrec.2018.01.004>.
- [5] The World Bank Group. The Growing Role of Minerals and Metals for a Low Carbon Future. *The Growing Role of Minerals and Metals for a Low Carbon Future*, June 2017.
- [6] A. King. Battery builders get the cobalt blues. <https://www.chemistryworld.com/news/battery-builders-get-the-cobalt-blues/3008738.article>. Accessed: 2019-06-06.
- [7] Blue Mining consortium. Blue Mining - Breakthrough Solutions for Mineral Extraction and Processing in Extreme Environments. *Public Report*, 2018. URL <http://www.bluemining.eu/download/project{ }results/public{ }reports/Blue-mining-Public-Report-2018.pdf>.
- [8] A. Månberger and B. Stenqvist. Global metal flows in the renewable energy transition: Exploring the effects of substitutes, technological mix and development. *Energy Policy*, 119:226–241, 2018.
- [9] J. Desjardins. China’s staggering demand for commodities. *Visual Capitalist*, 3 2018.
- [10] G. M. Mudd. Global trends in gold mining: Towards quantifying environmental and resource sustainability. *Resources Policy*, 32(1-2):42–56, 2007. ISSN 03014207. doi: 10.1016/j.resourpol.2007.05.002.

- 
- [11] A. Valero G. Calvo, G. Mudd and A. Valero. Decreasing Ore Grades in Global Metallic Mining: A Theoretical Issue or a Global Reality? *Resources*, 5(4):36, 2016. ISSN 2079-9276. doi: 10.3390/resources5040036.
- [12] J.Copley. Just how little do we know about the ocean floor. *The Conversation*, 9, 2014.
- [13] E.K.T. Frimanslund. Feasibility of deep-sea mining operation within norwegian jurisdiction. Master's thesis, NTNU, 2016.
- [14] J.R. Hein. Cobalt-rich ferromanganese crusts: global distribution, composition, origin and research activities. *International Seabed Authority, Technical Study*, 2:36–89, 2002.
- [15] R. Sharma. Environmental Issues of Deep-Sea Mining. *Procedia Earth and Planetary Science*, 11:204–211, 2015. ISSN 18785220. doi: 10.1016/j.proeps.2015.06.026.
- [16] M. Henriques. Japan's grand plans to mine deep-sea vents. *BBC - Future*, 2019. URL <http://www.bbc.com/future/story/20181221-japans-grand-plans-to-mine-deep-sea-vents>.
- [17] P. Johnston K.A. Miller, K.F. Thompson and D. Santillo. An overview of seabed mining including the current state of development, environmental impacts, and knowledge gaps. *Frontiers in Marine Science*, 4:418, 2018.
- [18] E. Escobar M. Gianni K.M Gjerde A Jaeckel D.O.B. Jones L. A. Levin H. J. Niner L. Pendleton C.R. Smith T. Thiele P.J. Turner L. Watling P.P.E. Weaver C. L. Van Dover, J. A. Ardron. Biodiversity loss from deep-sea mining. *Nature Geoscience*, 10:464, jun 2017. URL <https://doi.org/10.1038/ngeo2983><http://10.0.4.14/ngeo2983>.
- [19] P. Chwastiak A. See P. Munro P. Jankowski, E. Heymann and I. Lipton. Offshore Production System Definition and Cost Study. *Nautilus Minerals*, 1(June):81, 2010.
- [20] Nautilus Minerals Niugini Ltd. Preliminary Economic Assessment of the Solwara Project, Bismarck Sea, PNG. *Technical Report compiled under NI 43-101 AMC*, February 2018.
- [21] K. Aasly. Ntnu utvider sin satsing på havbunnsmineraler. *NTNU Tech-Zone*, June 2015. URL <https://www.ntnutechzone.no/2015/06/ntnu-utvider-sin-satsing-pa-havbunnsmineraler/>.
- [22] S.F.Q Williksen. A Study of Deep Sea Mining Electrical Power System Topologies, 2017.
- [23] G. Smith and Nautilus Minerals. OTC 21646 Deepwater Seafloor Resource Production – The Bismarck Sea Development Project Hydrothermal Vent Systems / SMS Deposits. pages 1–14, 2011.

- 
- [24] R.N. Fard and E. Tedeschi. Investigation of AC and DC power distributions to seafloor mining equipment. *OCEANS 2017 - Aberdeen*, 2017-October:1–7, 2017.
- [25] R.N. Fard and E. Tedeschi. Power system design considerations for a seafloor mining vehicle. *2018 IEEE Energy Conversion Congress and Exposition (ECCE), Portland, OR*, pages 164–1171, 09 2018.
- [26] B. Zahedi. Shipboard dc hybrid power systems. *Modeling, efficiency analysis and stability control [dissertation]. Trondheim, Norway: Norwegian University of Science and Technology*, 2014.
- [27] E. Tedeschi. Lecture 2 - hvdc technology - power electronics in future power systems, September 2018.
- [28] K. Rajashekara and B.S. Naik H.S. Krishnamoorthy. Electrification of subsea systems: requirements and challenges in power distribution and conversion. *CPSS Transactions on Power Electronics and Applications*, 2(4):259–266, 2017.
- [29] Å.M.H. Kjørholt. Hvdc transmission using a bipolar configuration composed of an lcc and mmc: operating characteristics of skagerrak 3 and skagerrak 4. Master’s thesis, Institutt for elkraftteknikk, 2014.
- [30] G. Pinares. On the Analysis of DC Network Dynamics of VSC-based HVDC Systems. 2014.
- [31] A. Yu and P. Espinasse. Extending deepwater technology to seafloor mining. *presented at the OTC*, 2009.
- [32] A. Benbia B. Waquet, D. Faulds. Understanding the effects of deep-sea conditions on seafloor massive sulfide deposits crushing process. *Offshore Technology Conference*, 2014.
- [33] C. Herrmann J. Rongau L. Weixler G. Spagnoli, Giovanni S.A. Miedema and Julien J. Denegre. Preliminary design of a trench cutter system for deep-sea mining applications under hyperbaric conditions. *IEEE Journal of Oceanic Engineering*, 41(4):930–943, 2016.
- [34] Norwegian Technology Industry. Norsok standard electrical systems. *NORSOK STANDARD, Drilling facilities, E-001, Rev.4, 2*, 2001.
- [35] Lars Øyvind Moen. Private phone call, Nexans, 7. May 2019.
-

- 
- [36] Andrew A. Burstein, V. Čuk, and E. de Jong. Determining potential capacity gains when repurposing MVAC cables for DC power transportation. *CIREN - Open Access Proceedings Journal*, 2017(1):1691–1694, 2017. doi: 10.1049/oap-cired.2017.0142.
- [37] E. Tedeschi R.N. Fard, O.A. Eidsvik and I. Schølberg. Cable selection considerations for subsea vehicles. *2018 OCEANS - MTS/IEEE Kobe Techno-Oceans, OCEANS - Kobe 2018*, 2018. doi: 10.1109/OCEANSKOB.2018.8559225.
- [38] J. Andrews S. Demmig and R. Klug. Control of subsea motors on multi-km cable lengths by variable frequency drives. In *Petroleum and Chemical Industry Conference Europe Electrical and Instrumentation Applications*, pages 1–10. IEEE, 2011.
- [39] Thore Linn. Private e-mail correspondence, ABB, 9. May 2019.
- [40] R. Nilsen. Tet4120 - electric drives, January 2018.
- [41] IEEE/CIGRE. Definition and classification of power system stability. 19(June):1387–1401, 2003.
- [42] M.G Lauby P. Kundur, N.J. Balu. *Power system stability and control*, volume 7. McGraw-hill New York, 1994.
- [43] G. Pinares. *Analysis of dc-network stability of VSC-based HVDC grids*. Number September. 2016. ISBN 9789175974392.
- [44] J. A. Suul S. D’Arco. Small signal modelling and eigenvalue analysis of multiterminal hvdc grids, 2018. URL [https://www.sintef.no/globalassets/project/eera-deepwind-2018/presentations/b2\\_darco\\_small-signal.pdf](https://www.sintef.no/globalassets/project/eera-deepwind-2018/presentations/b2_darco_small-signal.pdf).
- [45] A.Abdulkarim I.S.Madugu, B.J.Olufeagba. Control of hvdc power system oscillation using eigenvalue techniques. *Journal of Research Information in Civil Engineering*, 14(1), 2017.
- [46] T. Roskilly and Rikard R. Mikalsen. *Marine systems identification, modeling and control*. Butterworth-Heinemann, 2015.
- [47] S.M. Shinnars. *Modern control system theory and design*. John Wiley & Sons, 1998.
- [48] N. Mithulananthan K. Prasertwong and D. Thakur. Understanding Low-Frequency Oscillation in Power Systems. *International Journal of Electrical Engineering & Education*, 47(3):248–262, 2013. ISSN 0020-7209. doi: 10.7227/ijeee.47.3.2.
- [49] D. Gan D. Wu H. Xin, W. Dong and X. Yuan. Generalized short circuit ratio for multi power electronic based devices infeed systems: Definition and theoretical analysis. *arXiv preprint arXiv:1708.08046*, 2017.

- 
- [50] M.H. Nawir. Integration of Wind Farms Into Weak AC Grids. *School of Engineering - Cardiff University*, 2017.
- [51] C. Ozansoy M. Alizadeh and T. Alpcan. The impact of x/r ratio on voltage stability in a distribution network penetrated by wind farms. *Australasian Universities Power Engineering Conference (AUPEC), Brisbane, QLD, 2016*, (1–6), 2016. doi: 10.1109/AUPEC.2016.7749289.
- [52] S. Chiniforoosh, V. Sood V. Dinavahi J.A. Martinez J. Jatskevich, A. Yazdani, and A. Ramirez. Definitions and applications of dynamic average models for analysis of power systems. *IEEE Transactions on Power Delivery*, 25(4):2655–2669, 2010. ISSN 08858977. doi: 10.1109/TPWRD.2010.2043859.
- [53] M. Mitra S. Chattopadhyay and S. Sengupta. Electric power quality. In *Electric Power Quality*, pages 5–12. Springer, 2011.
- [54] S.A. Sanchez. Lecture 6 - practical example on control of a vsc, September 2018.
- [55] K. Vogel and A.J. Rossa. Improving efficiency in AC drives: Comparison of topologies and device technologies. *PCIM Europe Conference Proceedings*, (May):509–516, 2014. ISSN 21913358.
- [56] C. Bajracharya. Control of vsc-hvdc for wind power. Master’s thesis, Institutt for elkraftteknikk, 2008.
- [57] E. Tedeschi. Lecture 4 - current controller - power electronics in future power systems, September 2018.





---

# Appendix

## A Per-unit calculations

- $S_b$ : Nominal 3-phase apparent power of the AC supply side.
- $V_{ll,rms}$ : Nominal line-to-line rms voltage of the supply side.
- $V_b$ : Nominal peak phase-to-ground voltage of the AC supply side.
- $I_b$ : Nominal peak phase current of the AC supply side.
- $Z_b$ : Base impedance.
- $\omega_b$ : Base angular velocity.

$$V_b = \frac{\sqrt{2}}{\sqrt{3}} V_{ll,rms} \quad (8.1)$$

$$I_b = \frac{2 S_b}{3 V_b} \quad (8.2)$$

$$Z_b = \frac{V_b}{I_b} \quad (8.3)$$

- $R_{ac}$ : Resistance.
- $L_{ac}$ : Inductance.
- $C_{ac}$ : Capacitance.

$$R_{pu} = \frac{R_{ac}}{Z_b} \quad (8.4)$$

$$L_{pu} = \frac{\omega_b L_{ac}}{Z_b} \quad (8.5)$$

$$C_{pu} = \frac{1}{\omega_b C_{ac} Z_b} \quad (8.6)$$

## B ABC to dq transformation

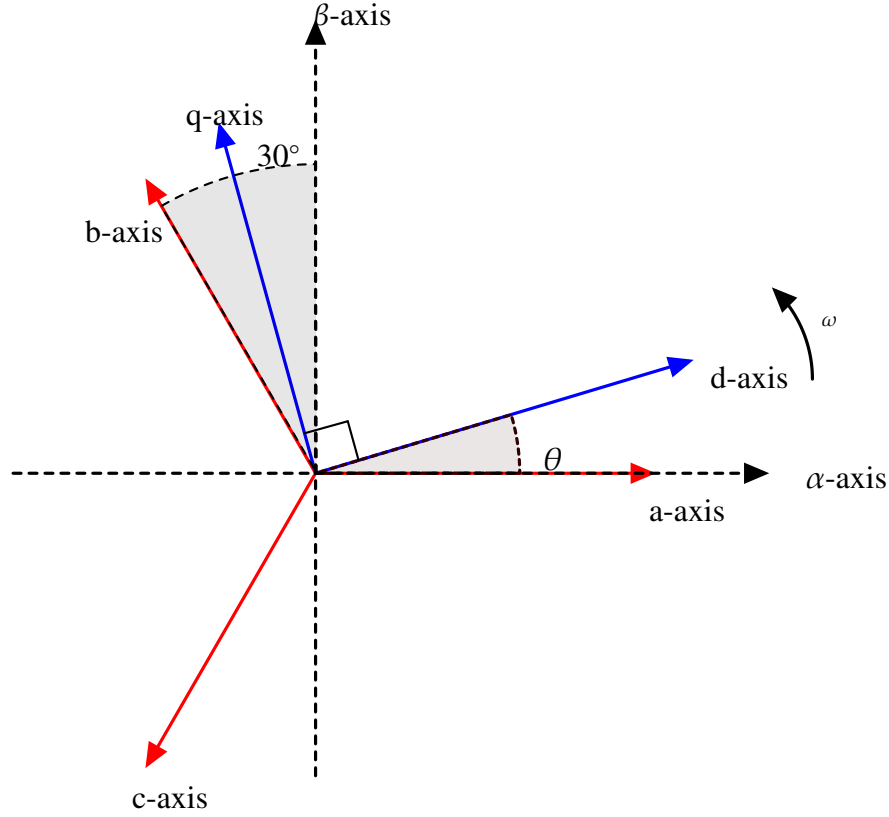


**Figure B1:** Transformation of axes for vector control

The first step of the transformation from the abc-reference frame to the  $dq$  rotating reference frame is a transformation to a fixed  $\alpha\beta$  reference frame. The transformation is simply the sum of the vector components of the abc-axes.

$$X_\alpha = K_\alpha(X_a \cdot \cos(0) - X_b \cdot \sin(30) - X_c \cdot \sin(30)) = K_\alpha(X_a - \frac{1}{2}X_b - \frac{1}{2}X_c) \quad (8.7)$$

$$X_\beta = K_\beta(X_a \cdot \sin(0) + X_b \cdot \cos(30) - X_c \cdot \cos(30)) = K_\beta(\frac{\sqrt{3}}{2}X_b - \frac{\sqrt{3}}{2}X_c) \quad (8.8)$$

The constants  $K_\alpha$  and  $K_\beta$  can be determined by assuming the faces to be

$$X_a = X \cdot \cos(\omega t)$$

$$X_b = X \cdot \cos(\omega t + \frac{2\pi}{3})$$

$$X_c = X \cdot \cos(\omega t - \frac{2\pi}{3})$$

and substitute the expressions into equation 8.7 and 8.8.

$$\begin{aligned}
X_\alpha &= K_\alpha \left( X \cdot \cos(\omega t) - \frac{1}{2} X \cdot \cos\left(\omega t + \frac{2\pi}{3}\right) - \frac{1}{2} X \cdot \cos\left(\omega t - \frac{2\pi}{3}\right) \right) \\
&= K_\alpha \left( X \cdot \cos(\omega t) - \frac{X}{2} \cos(\omega t) \cos\left(\frac{2\pi}{3}\right) - \frac{X}{2} \sin(\omega t) \sin\left(\frac{2\pi}{3}\right) - \frac{X}{2} \cos(\omega t) \cos\left(-\frac{2\pi}{3}\right) - \frac{X}{2} \sin(\omega t) \sin\left(-\frac{2\pi}{3}\right) \right) \\
&= K_\alpha \left( X \cdot \cos(\omega t) + \frac{X}{4} \cos(\omega t) - \frac{\sqrt{3}X}{2} \sin(\omega t) + \frac{X}{4} \cos(\omega t) + \frac{\sqrt{3}X}{2} \sin(\omega t) \right) \\
&= K_\alpha \frac{3X}{2} \cos(\omega t)
\end{aligned}$$

In order to keep the vector amplitude constant  $K_\alpha$  has to be  $\frac{2}{3}$ . The constant  $K_\beta$  can be determined with a similar approach.

$$\begin{aligned}
X_\beta &= K_\beta \left( \frac{\sqrt{3}}{2} X \cdot \cos\left(\omega t + \frac{2\pi}{3}\right) - \frac{\sqrt{3}}{2} X \cdot \cos\left(\omega t - \frac{2\pi}{3}\right) \right) \\
&= K_\beta \left( \frac{\sqrt{3}X}{2} \cos(\omega t) \cos\left(\frac{2\pi}{3}\right) - \frac{\sqrt{3}X}{2} \sin(\omega t) \sin\left(\frac{2\pi}{3}\right) - \frac{\sqrt{3}X}{2} \cos(\omega t) \cos\left(-\frac{2\pi}{3}\right) + \frac{\sqrt{3}X}{2} \sin(\omega t) \sin\left(-\frac{2\pi}{3}\right) \right) \\
&= K_\beta \left( \frac{\sqrt{3}X}{2} \cos(\omega t) \cos\left(\frac{2\pi}{3}\right) - \frac{\sqrt{3}X}{2} \sin(\omega t) \sin\left(\frac{2\pi}{3}\right) - \frac{\sqrt{3}X}{2} \cos(\omega t) \cos\left(-\frac{2\pi}{3}\right) + \frac{\sqrt{3}X}{2} \sin(\omega t) \sin\left(-\frac{2\pi}{3}\right) \right) \\
&= K_\beta \left( -\frac{\sqrt{3}X}{4} \cos(\omega t) - \frac{3X}{4} \sin(\omega t) + \frac{\sqrt{3}X}{4} \cos(\omega t) - \frac{3X}{4} \sin(\omega t) \right) \\
&= -K_\beta \frac{3X}{2} \sin(\omega t)
\end{aligned}$$

The amplitude of the vector  $X_b$  is kept constant if  $K_\beta = \frac{2}{3}$ .

The final abc- $\alpha\beta$  transformation can be expressed as,

$$X_\alpha = \frac{1}{3}(2X_a - X_b - X_c) \quad (8.9)$$

$$X_\beta = \frac{1}{\sqrt{3}}(X_b - X_c) \quad (8.10)$$

and the inverse as,

$$X_a = X_\alpha \quad (8.11)$$

$$X_b = -\frac{1}{2}X_\alpha + \frac{\sqrt{3}}{2}X_\beta \quad (8.12)$$

$$X_c = -\frac{1}{2}X_\alpha - \frac{\sqrt{3}}{2}X_\beta \quad (8.13)$$

The next step is to do the  $\alpha\beta$  to dq transformation. The  $\alpha\beta$  vector can be given as,

---

$$\bar{X}_{\alpha\beta} = X_{\alpha} + jX_{\beta} \quad (8.14)$$

The fixed  $\alpha\beta$ -frame is made to rotate by including the rotating term  $e^{j\omega t}$ , which results in the  $\alpha\beta - dq$  transformation,

$$\bar{X}_{dq}^R = \bar{X}_{\alpha\beta} \cdot e^{j\omega t} = \bar{X}_{dq} \cdot e^{j\omega t} \quad (8.15)$$

## C Dq0-transformation of VSC system equations

Based on the transformation steps presented in appendix B the system equations of a VSC can be derived.

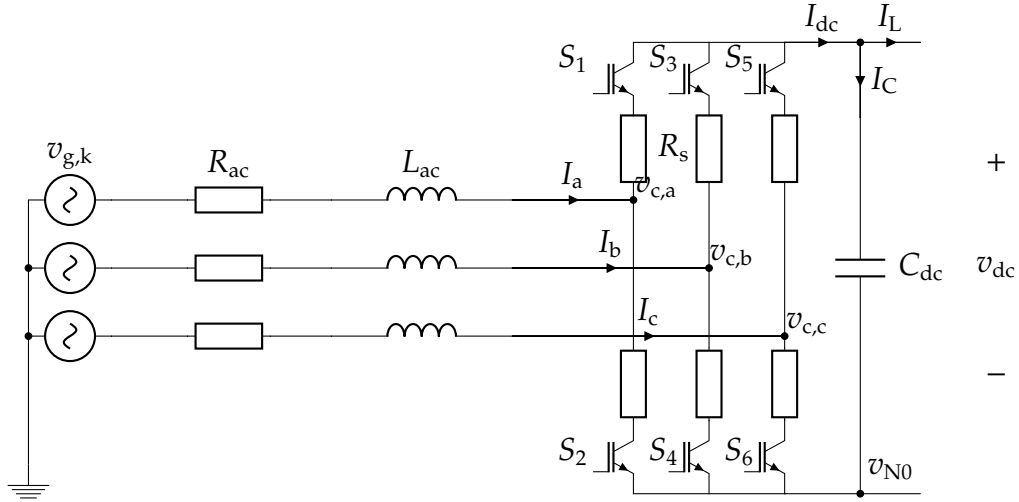


**Figure C1:** Circuit diagram of a 2-level VSC

Based on KVL phase  $a$  can be expressed as,

$$L_{ac} \frac{di_a}{dt} + R_{ac} i_a = v_{g,a} - v_{c,a} - v_{N0} \quad (8.16)$$

where,

- $L_{ac}$ : Inductive component of converter impedance.
- $R_{ac}$ : Resistive component of converter impedance.
- $v_{g,k}$ : Voltage at PCC in phase  $k$ .
- $v_{c,k}$ : Converter terminal voltage in phase  $k$ .
- $v_{N0}$ : Voltage from node  $N$  to ground.

The dc side expression can be derived by using KCL, which gives,

$$i_{dc} = i_a \cdot d_a^* + i_b \cdot d_b^* + i_c \cdot d_c^* = C_{dc} \frac{dv_{dc}}{dt} + i_L \quad (8.17)$$

where,

- $C_{dc}$ : Smoothing capacitor.
- $i_{dc}$ : Current flowing out from the converter terminals.

- $i_C$ : Current flowing through from the smoothing capacitor.
- $i_L$ : Current flowing through the dc link.
- $d_k^*$ : Switching state of converter arm  $k$ .

The terminal voltage of the converter depends on the conduction state of the switches. There are two different states,

- $S_1$  on  $S_4$  off  $\rightarrow d_a^* = 1, d_a'^* = 0 \rightarrow v_{c,a} = R_{ac}i_a + v_{dc}$
- $S_1$  on  $S_4$  off  $\rightarrow d_a^* = 0, d_a'^* = 1 \rightarrow v_{c,a} = R_s i_a$

The states combined can be expressed as:

$$v_{c,a} = d_a^*(R_s i_a + v_{dc}) + d_a'^*(R_s i_a) = R_{ac}(d_a^* i_a + d_a'^* i_a) + d_a^* v_{dc} \quad (8.18)$$

so 8.16 becomes,

$$L_{ac} \frac{di_a}{dt} + R_{ac} i_a = v_{g,a} - (R_{ac}(d_a^* i_a + d_a'^* i_a) + d_a^* v_{dc}) - v_{N0} \quad (8.19)$$

$S_1$  and  $S_4$  are complementary, therefore  $d_1^* + d_1'^* = 1$ .

$$L_{ac} \frac{di_a}{dt} + R_{ac} i_a = v_{g,a} - (R_{ac} i_a + d_a^* v_{dc}) - v_{N0} \quad (8.20)$$

The two other phases can be represented similarly. The sum of the phases is given by the expression,

$$L_{ac} \left( \frac{di_a}{dt} + \frac{di_b}{dt} + \frac{di_c}{dt} \right) + R_{ac}(i_a + i_b + i_c) = (v_{g,a} + v_{g,b} + v_{g,c}) - R_s(i_a + i_b + i_c) - v_{dc}(d_a^* + d_b^* + d_c^*) - 3v_{N0} \quad (8.21)$$

Assuming the 3-phase system is in balance, the sum of the voltages and the currents equals zero. This is also the case for the sum of the derivatives. Thus, the term  $v_{N0}$  can be expressed as,

$$v_{N0} = -\frac{1}{3} v_{dc}(d_a^* + d_b^* + d_c^*) \quad (8.22)$$

The generic expression for one of the phases is given by,

$$L_{ac} \frac{di_k}{dt} + R_{ac} i_k = v_{g,k} - d_k^* v_{dc} + \frac{v_{dc}}{3} \sum_{k=1}^3 d_k^* \quad (8.23)$$

## Abc to Alpha-Beta

By using the abc- $\alpha\beta$  transformation given in expression 8.11, 8.12 and 8.13, the system equation can be transformed into a fixed two-phase reference frame. Note the relationship  $v_{c,k} = d_k^* v_{dc}$ . The term  $v_{N0}$  becomes,

$$v_{N0} = -\frac{1}{3}v_{dc}(d_\alpha^* - \frac{1}{2}d_\alpha^* + \frac{\sqrt{3}}{2}d_\beta^* - \frac{1}{2}d_\alpha^* - \frac{\sqrt{3}}{2}d_\beta^*) = 0 \quad (8.24)$$

Phase  $a$  is transformed into,

$$L_{ac} \frac{di_\alpha}{dt} + R_{ac}i_\alpha = v_{g,\alpha} - v_{c,\alpha} \quad (8.25)$$

and phase  $b$  into,

$$L_{ac} \frac{d}{dt}(-\frac{1}{2}i_\alpha + j\frac{\sqrt{3}}{2}i_\beta) + R_{ac}(-\frac{1}{2}i_\alpha + j\frac{\sqrt{3}}{2}i_\beta) = (-\frac{1}{2}v_{g,\alpha} + j\frac{\sqrt{3}}{2}v_{g,\beta}) - (-\frac{1}{2}v_{c,\alpha} + j\frac{\sqrt{3}}{2}v_{g,\beta})$$

The different components can be expressed with the equations,

$$-L_{ac} \frac{d}{dt} \frac{1}{2}i_\alpha - R_{ac} \frac{1}{2}i_\alpha = -\frac{1}{2}v_{g,\alpha} + \frac{1}{2}v_{c,\alpha} \quad (8.26)$$

$$L_{ac} \frac{d}{dt} \frac{\sqrt{3}}{2}i_\beta + R_{ac} \frac{\sqrt{3}}{2}i_\beta = \frac{\sqrt{3}}{2}v_{g,\beta} - \frac{\sqrt{3}}{2}v_{g,\beta} \quad (8.27)$$

The expressions can further be simplified into,

$$L_{ac} \frac{d}{dt}i_\alpha + R_{ac}i_\alpha = v_{g,\alpha} - v_{c,\alpha} \quad (8.28)$$

$$L_{ac} \frac{d}{dt}i_\beta + R_{ac}i_\beta = v_{g,\beta} - v_{g,\beta} \quad (8.29)$$

Similar expressions can be derived from phase  $c$  and is therefore not derived. Expression 8.17 is transformed accordingly,

$$C_{dc} \frac{dv_{dc}}{dt} = i_\alpha \cdot d_\alpha^* + (-\frac{1}{2}i_\alpha + \frac{\sqrt{3}}{2}i_\beta)(-\frac{1}{2}d_\alpha^* + \frac{\sqrt{3}}{2}d_\beta^*) + (-\frac{1}{2}i_\alpha - \frac{\sqrt{3}}{2}i_\beta)(-\frac{1}{2}d_\alpha^* - \frac{\sqrt{3}}{2}d_\beta^*) - i_L \quad (8.30)$$

$$C_{dc} \frac{dv_{dc}}{dt} = i_\alpha \cdot d_\alpha^* + \frac{1}{4}i_\alpha d_\alpha^* - \frac{\sqrt{3}}{4}i_\alpha d_\beta^* - \frac{\sqrt{3}}{4}i_\beta d_\alpha^* + \frac{3}{4}i_\beta d_\beta^* + \frac{1}{4}i_\alpha d_\alpha^* + \frac{\sqrt{3}}{4}i_\alpha d_\beta^* + \frac{\sqrt{3}}{4}i_\beta d_\alpha^* + \frac{3}{4}i_\beta d_\beta^* - i_L \quad (8.31)$$

---


$$C_{dc} \frac{dv_{dc}}{dt} = \frac{6}{4} i_{\alpha} d_{\alpha}^* + \frac{6}{4} i_{\beta} d_{\beta}^* - i_L = \frac{3}{2} (i_{\alpha} d_{\alpha}^* + i_{\beta} d_{\beta}^*) - i_L \quad (8.32)$$

### Alpha-Beta to dq0

The expression 8.15 is substituted in to transform the system equations into a dq0 reference frame (Appendix B).

$$L_{ac} \frac{d}{dt} (\bar{i}_{dq} \cdot e^{j\omega t}) + R_{ac} (\bar{i}_{dq} \cdot e^{j\omega t}) = (\bar{v}_{g,dq} \cdot e^{j\omega t}) - (\bar{v}_{c,dq} \cdot e^{j\omega t}) \quad (8.33)$$

$$L_{ac} \frac{d}{dt} (\bar{i}_{dq} \cdot e^{j\omega t}) + (j\omega L_{ac} \bar{i}_{dq}) \cdot e^{j\omega t} + R_{ac} (\bar{i}_{dq} \cdot e^{j\omega t}) = (\bar{v}_{g,dq} \cdot e^{j\omega t}) - (\bar{v}_{c,dq} \cdot e^{j\omega t}) \quad (8.34)$$

The different components can be separated and expressed with the equations,

$$L_{ac} \frac{d}{dt} i_d - \omega L_{ac} i_q + R_{ac} i_d = v_{g,d} - v_{c,d} \quad (8.35)$$

$$L_{ac} \frac{d}{dt} i_q + \omega L_{ac} i_d + R_{ac} i_q = v_{g,q} - v_{c,q} \quad (8.36)$$

The expression for the dc currents becomes,

$$C_{dc} \frac{dv_{dc}}{dt} = \frac{2}{3} \cdot \text{Re}(i_{dq} e^{j\omega t} \cdot d_{dq}^* e^{j\omega t}) - i_L \quad (8.37)$$

$$= \frac{2}{3} (i_d \cdot d_d^* + i_q \cdot d_q^*) - i_L \quad (8.38)$$

Assuming there the power loss in the converter to be negligible, the power balance can be expressed as,

$$P = \frac{2}{3} (i_d \cdot v_d + i_q \cdot v_q) = v_{dc} \cdot i_{dc} \quad (8.39)$$

As the voltage vector is defined to be aligned with the d-axis, the q-component of the voltage is zero, hence the expression for the active power can be written as,

$$P = \frac{2}{3} (i_d \cdot v_d) \quad (8.40)$$

$I_{dc}$  can therefore be expressed as,

$$I_{dc} = \frac{3}{2} \frac{v_d}{v_{dc} i_d} \quad (8.41)$$



## D Participation factor tables

Participation factors of system with gains based on tuning principles

**Table D1:** Participation factors of tuning principle obtained gains

	$\lambda_1$	$\lambda_2$	$\lambda_3$	$\lambda_4$	$\lambda_5$	$\lambda_6$	$\lambda_7$	$\lambda_8$	$\lambda_9$	$\lambda_{10}$	$\lambda_{11}$	$\lambda_{12}$	$\lambda_{13}$	$\lambda_{14}$	$\lambda_{15}$
$i_{d1}$	0	0	0.535	0.535	0.082	0.082	0.108	0.108	0	0	0	0	0	0	0
$i_{q1}$	0	0	0	0	0	0	0	0	0	0.535	0.535	0	0	0	0
$\xi_{d1}$	0	0	0.535	0.535	0.005	0.005	0.004	0.004	0	0	0	0	0	0	0
$\xi_{q1}$	0	0	0	0	0	0	0	0	0	0.535	0.535	0	0	0	0
$\xi_v$	0	0	0.008	0.008	0.116	0.116	0.432	0.432	0	0	0	0	0	0	0
$i_{d2}$	0	0	0	0	0	0	0	0	0	0	0	0.617	0.617	0	0
$i_{q2}$	0.346	0.346	0	0	0	0	0	0	0.312	0	0	0	0	0	0
$\psi_r$	0	0	0	0	0	0	0	0	0	0	0	0	0	1	0
$\xi_{sp}$	0.305	0.305	0	0	0	0	0	0	0.397	0	0	0	0	0	0
$\xi_{d2}$	0	0	0	0	0	0	0	0	0	0	0	0.617	0.617	0	0
$\xi_{q2}$	0.009	0.009	0	0	0	0	0	0	0.009	0	0	0	0	0	1
$n_{mech}$	0.351	0.351	0	0	0	0	0	0	0.3	0	0	0	0	0	0
$v_{dc1}$	0	0	0.001	0.001	0.142	0.142	0.36	0.36	0	0	0	0	0	0	0
$v_{dc2}$	0	0	0	0	0.409	0.409	0.122	0.122	0	0	0	0	0	0	0
$i_{dc12}$	0	0	0.009	0.009	0.49	0.49	0.094	0.094	0	0	0	0	0	0	0

---

## Participation factors related to change in VSC current controller

**Table D2:** Participation factors of moving poles at the extremities of the proportional gain  $Kp_{c,c}$

	$Kp_{c,c} = 0.0025$				$Kp_{c,c} = 0.75$			
	$\Lambda_A$		$\Lambda_B$		$\Lambda_A$		$\Lambda_B$	
$\dot{i}_{d1}$	0.373	0.373	0	0	1.202	1.202	0	0
$\dot{i}_{q1}$	0	0	0.5	0.5	0	0	2.588	2.588
$\xi_{d1}$	0.38	0.38	0	0	0.78	0.78	0	0
$\xi_{q1}$	0	0	0.5	0.5	0	0	2.588	2.588
$\xi_v$	0.002	0.002	0	0	0.009	0.009	0	0
$\dot{i}_{d2}$	0	0	0	0	0	0	0	0
$\dot{i}_{q2}$	0	0	0	0	0	0	0	0
$\psi_r$	0	0	0	0	0	0	0	0
$\xi_{sp}$	0	0	0	0	0	0	0	0
$\xi_{d2}$	0	0	0	0	0	0	0	0
$\xi_{q2}$	0	0	0	0	0	0	0	0
$n_{mech}$	0	0	0	0	0	0	0	0
$v_{dc1}$	0.104	0.104	0	0	0.28	0.28	0	0
$v_{dc2}$	0.023	0.023	0	0	0.058	0.058	0	0
$\dot{i}_{dc12}$	0.127	0.127	0	0	0.314	0.314	0	0

**Table D3:** Participation factors of moving poles at the extremities of the proportional gain  $Ki_{c,c}$

	$Ki_{c,c} = 0.09$						$Ki_{c,c} = 3.08$						
	$\Lambda_A$	$\Lambda_B$	$\Lambda_C$	$\Lambda_D$	$\Lambda_A$	$\Lambda_B$	$\Lambda_C$	$\Lambda_D$	$\Lambda_A$	$\Lambda_B$	$\Lambda_C$	$\Lambda_D$	
$i_{d1}$	0.232	0.232	0	0.112	0.112	0	0.624	0.624	0.466	0.466	0	0.028	0.088
$i_{q1}$	0	1.168	1.168	0	0	0	0	0	0	0	0.506	0	0
$\xi_{d1}$	0.055	0.055	0	0.083	0.083	0	0.71	0.71	0.462	0.462	0	0.003	0.045
$\xi_{q1}$	0	1.168	1.168	0	0	0	0	0	0	0	0.506	0	0
$\xi_v$	0.004	0.004	0	0.521	0.521	0	0.125	0.125	0.001	0.001	0	0.501	0.003
$i_{d2}$	0	0	0	0	0	0	0	0	0	0	0	0	0
$i_{q2}$	0	0	0	0	0	0	0	0	0	0	0	0	0
$\psi_r$	0	0	0	0	0	0	0	0	0	0	0	0	0
$\xi_{sp}$	0	0	0	0	0	0	0	0	0	0	0	0	0
$x_{d2}$	0	0	0	0	0	0	0	0	0	0	0	0	0
$x_{d2}$	0	0	0	0	0	0	0	0	0	0	0	0	0
$n_{mech}$	0	0	0	0	0	0	0	0	0	0	0	0	0
$v_{dc1}$	0.297	0.297	0	0.54	0.54	0	0.32	0.32	0.044	0.044	0	0.499	0.084
$v_{dc2}$	0.223	0.223	0	0.061	0.061	0	0.357	0.357	0.003	0.003	0	0.015	0.517
$i_{dc12}$	0.523	0.523	0	0.002	0.002	0	0.057	0.057	0.049	0.049	0	0	0.479

## Participation factors related to change in dc voltage controller

**Table D4:** Participation factors of moving poles at the extremities of the proportional gain  $Kp_v$

	$Kp_v = 0.045$						$Kp_v = 135$					
	$\Lambda_A$		$\Lambda_C$		$\Lambda_D$		$\Lambda_A$		$\Lambda_C$		$\Lambda_D$	
$i_{d1}$	0.392	0.392	0.03	0.03	0.162	0.162	0.42	0.42	0.119	0	0.091	0.091
$i_{q1}$	0	0	0	0	0	0	0	0	0	0	0	0
$\xi_{d1}$	0.373	0.373	0.008	0.008	0.147	0.147	0.316	0.316	0.319	0	0.075	0.075
$\xi_{q1}$	0	0	0	0	0	0	0	0	0	0	0	0
$\xi_v$	0.003	0.003	0.506	0.506	0.007	0.007	0.002	0.002	0.014	1.018	0.002	0.002
$i_{d2}$	0	0	0	0	0	0	0	0	0	0	0	0
$i_{q2}$	0	0	0	0	0	0	0	0	0	0	0	0
$\psi_r$	0	0	0	0	0	0	0	0	0	0	0	0
$\xi_{sp}$	0	0	0	0	0	0	0	0	0	0	0	0
$x\dot{i}_{d2}$	0	0	0	0	0	0	0	0	0	0	0	0
$x\dot{i}_{q2}$	0	0	0	0	0	0	0	0	0	0	0	0
$n_{mech}$	0	0	0	0	0	0	0	0	0	0	0	0
$v_{dc1}$	0.119	0.119	0.506	0.506	0.138	0.138	0.252	0.252	0.581	0.018	0.045	0.045
$v_{dc2}$	0.026	0.026	0.016	0.016	0.494	0.494	0.018	0.018	0.03	0	0.488	0.488
$i_{dc12}$	0.151	0.151	0.001	0.001	0.377	0.377	0.115	0.115	0.035	0	0.422	0.422

**Table D5:** Participation factors of moving poles at the extremities of the integral gain  $Ki_v$

	$Kp_v = 0.5$						$Kp_v = 300$					
	$\Lambda_A$		$\Lambda_C$		$\Lambda_D$		$\Lambda_A$		$\Lambda_C$		$\Lambda_D$	
$i_{d1}$	0.392	0.392	0.01	0.01	0.156	0.156	0.402	0.402	0.307	0.307	0.104	0.104
$i_{q1}$	0	0	0	0	0	0	0	0	0	0	0	0
$\xi_{d1}$	0.372	0.372	0.001	0.001	0.142	0.142	0.484	0.484	0.192	0.192	0.096	0.096
$\xi_{q1}$	0	0	0	0	0	0	0	0	0	0	0	0
$\xi_v$	0	0	0.504	0.504	0.001	0.001	0.35	0.35	0.579	0.579	0.171	0.171
$i_{d2}$	0	0	0	0	0	0	0	0	0	0	0	0
$i_{q2}$	0	0	0	0	0	0	0	0	0	0	0	0
$\psi_r$	0	0	0	0	0	0	0	0	0	0	0	0
$\xi_{sp}$	0	0	0	0	0	0	0	0	0	0	0	0
$x\dot{i}_{d2}$	0	0	0	0	0	0	0	0	0	0	0	0
$x\dot{i}_{q2}$	0	0	0	0	0	0	0	0	0	0	0	0
$n_{mech}$	0	0	0	0	0	0	0	0	0	0	0	0
$v_{dc1}$	0.12	0.12	0.502	0.502	0.129	0.129	0.19	0.19	0.423	0.423	0.058	0.058
$v_{dc2}$	0.026	0.026	0.006	0.006	0.493	0.493	0.059	0.059	0.089	0.089	0.622	0.622
$i_{dc12}$	0.149	0.149	0	0	0.378	0.378	0.241	0.241	0.192	0.192	0.745	0.745

## Participation factors related to change in VSD current controller

**Table D6:** Participation factors of moving poles at the extremities of the proportional gain  $Kp_{c,m}$

	$Kp_m = 0.007$				$Kp_m = 2.1$			
	$\lambda_E$		$\lambda_F$		$\lambda_E$		$\lambda_F$	
$i_{d1}$	0	0	0	0	0	0	0	0
$i_{q1}$	0	0	0	0	0	0	0	0
$\xi_{d1}$	0	0	0	0	0	0	0	0
$\xi_{q1}$	0	0	0	0	0	0	0	0
$\xi_v$	0	0	0	0	0	0	0	0
$i_{d2}$	0.5	0.5	0	0	1.081	1.081	0	0
$i_{q2}$	0	0	0.573	0.573	0	0	1.171	1.171
$\psi_r$	0	0	0	0	0	0	0	0
$\xi_{sp}$	0	0	0.123	0.123	0	0	0.255	0.255
$xi_{d2}$	0.5	0.5	0	0	1.081	1.081	0	0
$xi_{q2}$	0	0	0.573	0.573	0	0	1.456	1.456
$n_{mech}$	0	0	0.147	0.147	0	0	0.149	0.149
$v_{dc1}$	0	0	0	0	0	0	0	0
$v_{dc2}$	0	0	0	0	0	0	0	0
$i_{dc12}$	0	0	0	0	0	0	0	0

**Table D7:** Participation factors of moving poles at the extremities of the integral gain  $Ki_{c,m}$

	$Ki_m = 1.5$						$Ki_m = 7.5$					
	$\Lambda_E$		$\Lambda_F$		$\Lambda_G$		$\Lambda_E$		$\Lambda_F$		$\Lambda_G$	
$i_{d1}$	0	0	0	0	0	0	0	0	0	0	0	0
$i_{q1}$	0	0	0	0	0	0	0	0	0	0	0	0
$\xi_{d1}$	0	0	0	0	0	0	0	0	0	0	0	0
$\xi_{q1}$	0	0	0	0	0	0	0	0	0	0	0	0
$\xi_v$	0	0	0	0	0	0	0	0	0	0	0	0
$i_{d2}$	0.519	0.519	0	0	0	0	0.504	0.504	0	0	0	0
$i_{q2}$	0	0	0.364	0.364	0.284	0.284	0	0	0.586	0.586	0.1	0.1
$\psi_r$	0	0	0	0	0	0	0	0	0	0	0	0
$\xi_{sp}$	0	0	0.308	0.308	0.348	0.348	0	0	0.101	0.101	0.603	0.603
$xi_{d2}$	0.519	0.519	0	0	0	0	0.504	0.504	0	0	0	0
$xi_{q2}$	0	0	0.304	0.304	0.362	0.362	0	0	0.579	0.579	0.102	0.102
$n_{mech}$	0	0	0.315	0.315	0.352	0.352	0	0	0.12	0.12	0.604	0.604
$v_{dc1}$	0	0	0	0	0	0	0	0	0	0	0	0
$v_{dc2}$	0	0	0	0	0	0	0	0	0	0	0	0
$i_{dc12}$	0	0	0	0	0	0	0	0	0	0	0	0

---

## Participation factors related to change in speed controller

**Table D8:** Participation factors of moving poles at the extremities of the proportional gain  $Kp_{sp}$

	$Kp_{sp} = 0.008$				$Kp_{sp} = 2.4$			
	$\Lambda_F$		$\Lambda_G$		$\Lambda_F$		$\Lambda_G$	
$i_{d1}$	0	0	0	0	0	0	0	0
$i_{q1}$	0	0	0	0	0	0	0	0
$\xi_{d1}$	0	0	0	0	0	0	0	0
$\xi_{q1}$	0	0	0	0	0	0	0	0
$\xi_v$	0	0	0	0	0	0	0	0
$i_{d2}$	0	0	0	0	0	0	0	0
$i_{q2}$	0.684	0.684	0.18	0.18	0.526	0.526	0.097	0.097
$\psi_r$	0	0	0	0	0	0	0	0
$\xi_{sp}$	0.18	0.18	0.685	0.685	0.096	0.096	0.588	0.588
$xi_{d2}$	0	0	0	0	0	0	0	0
$xi_{q2}$	0.687	0.687	0.182	0.182	0.506	0.506	0.101	0.101
$n_{mech}$	0.182	0.182	0.69	0.69	0.178	0.178	0.567	0.567
$v_{dc1}$	0	0	0	0	0	0	0	0
$v_{dc2}$	0	0	0	0	0	0	0	0
$i_{dc12}$	0	0	0	0	0	0	0	0

**Table D9:** Participation factors of moving poles at the extremities of the integral gain  $Ki_{sp}$

	$Ki_{sp} = 0.13$				$Kp_v = 15.08$			
	$\Lambda_F$		$\Lambda_G$		$\Lambda_F$		$\Lambda_G$	
$i_{d1}$	0	0	0	0	0	0	0	0
$i_{q1}$	0	0	0	0	0	0	0	0
$\xi_{d1}$	0	0	0	0	0	0	0	0
$\xi_{q1}$	0	0	0	0	0	0	0	0
$\xi_v$	0	0	0	0	0	0	0	0
$i_{d2}$	0	0	0	0	0	0	0	0
$i_{q2}$	0.507	0.507	0.01	0.01	0.591	0.591	0.374	0.374
$\psi_r$	0	0	0	0	0	0	0	0
$\xi_{sp}$	0.01	0.01	0.852	0.852	0.38	0.38	0.594	0.594
$\xi_{d2}$	0	0	0	0	0	0	0	0
$\xi_{q2}$	0.5	0.5	0.01	0.01	0.568	0.568	0.395	0.395
$n_{mech}$	0.055	0.055	0.854	0.854	0.396	0.396	0.588	0.588
$v_{dc1}$	0	0	0	0	0	0	0	0
$v_{dc2}$	0	0	0	0	0	0	0	0
$i_{dc12}$	0	0	0	0	0	0	0	0

---

## Participation factors of SCR sensitivity analysis

**Table D10:** Participation factors of the moving poles at SCR with a X/R ratio of 1

	SCR = 47				SCR = 0.47			
	$\Lambda_A$		$\Lambda_C$		$\Lambda_A$		$\Lambda_C$	
$i_{d1}$	0.388	0.388	0.03	0.03	0.065	0.065	0.124	0.191
$i_{q1}$	0.001	0.001	0	0	0.017	0.017	0.002	0.001
$\xi_{d1}$	0.369	0.369	0.009	0.009	0.093	0.093	0.072	0.015
$\xi_{q1}$	0.001	0.001	0	0	0.003	0.003	0.121	0.3
$\xi_v$	0.003	0.003	0.506	0.506	0.002	0.002	0.571	0.275
$i_{d2}$	0	0	0	0	0	0	0	0
$i_{q2}$	0	0	0	0	0	0	0	0
$\psi_r$	0	0	0	0	0	0	0	0
$\xi_{sp}$	0	0	0	0	0	0	0	0
$xi_{d2}$	0	0	0	0	0	0	0	0
$xi_{q2}$	0	0	0	0	0	0	0	0
$n_{mech}$	0	0	0	0	0	0	0	0
$v_{dc1}$	0.122	0.122	0.504	0.504	0.279	0.279	0.26	0.118
$v_{dc2}$	0.028	0.028	0.017	0.017	0.208	0.208	0.342	0.133
$i_{dc12}$	0.155	0.155	0.001	0.001	0.478	0.478	0.001	0

**Table D11:** Participation factors of the moving poles at SCR with a X/R ratio of 0.2

	SCR = 40						SCR = 1					
	$\Lambda_A$	$\Lambda_B$	$\Lambda_C$	$\Lambda_G$	$\Lambda_A$	$\Lambda_B$	$\Lambda_C$	$\Lambda_G$	$\Lambda_A$	$\Lambda_B$	$\Lambda_C$	$\Lambda_G$
$i_{d1}$	0.835	0.05	0.01	0.12	0.509	0.006	0.001	0.12	0.509	0.001	0.001	0.007
$i_{q1}$	0.042	0.826	0	0	0.509	0.826	0	0	0.509	0	0	0
$\xi_{d1}$	0.71	0.045	0.003	0.056	0.009	0.045	0.003	0.056	0.009	0.833	0.044	0.167
$\xi_{q1}$	0.039	0.828	0	0	0.01	0.828	0	0	0.01	0	0	0
$\xi_v$	0	0	0.522	0	0	0	0.522	0	0	0.005	0.359	0.001
$i_{d2}$	0	0	0	0	0	0	0	0	0	0	0	0
$i_{q2}$	0	0	0	0	0	0	0	0	0	0	0	0
$\psi_r$	0	0	0	0	0	0	0	0	0	0	0	0
$\xi_{sp}$	0	0	0	0	0	0	0	0	0	0	0	0
$\xi_{d2}$	0	0	0	0	0	0	0	0	0	0	0	0
$\xi_{q2}$	0	0	0	0	0	0	0	0	0	0	0	0
$n_{mech}$	0	0	0	0	0	0	0	0	0	0	0	0
$v_{dc1}$	0.1	0.006	0.483	0.107	0.001	0.006	0.483	0.107	0.001	0.289	0.002	0.334
$v_{dc2}$	0.008	0	0.042	0.49	0	0	0.042	0.49	0	0.225	0.003	0.162
$i_{dc12}$	0.103	0.006	0	0.495	0.001	0.006	0	0.495	0.001	0.114	0	0.466



**Table D12:** Participation factors of moving poles at SCR with a X/R ratio of 5

	SCR = 49.0						SCR = 0.164						
	$\Lambda_A$	$\Lambda_B$	$\Lambda_C$	$\Lambda_G$	$\Lambda_A$	$\Lambda_G$	$\Lambda_A$	$\Lambda_B$	$\Lambda_C$	$\Lambda_G$	$\Lambda_B$	$\Lambda_C$	$\Lambda_G$
$i_{d1}$	0.716	0.03	0.011	0.118	0.068	0.118	0.068	0.322	0.05	0.243	0.322	0.05	0.295
$i_{q1}$	0.028	0.723	0	0	0.016	0	0.016	0.484	0.044	0.02	0.484	0.044	0.002
$\xi_{sd1}$	0.604	0.028	0	0.058	0.175	0.058	0.175	0.001	0.834	0.053	0.001	0.834	0.021
$\xi_{\eta 1}$	0.025	0.725	0	0	0.002	0	0.002	0.16	0.036	0.539	0.16	0.036	0.737
$\xi_v$	0	0	0.526	0.001	0.001	0.001	0.001	0	0.009	0.284	0	0.009	0.059
$i_{d2}$	0	0	0	0	0	0	0	0	0	0	0	0	0
$i_{q2}$	0	0	0	0	0	0	0	0	0	0	0	0	0
$\psi_r$	0	0	0	0	0	0	0	0	0	0	0	0	0
$\xi_{sp}$	0	0	0	0	0	0	0	0	0	0	0	0	0
$\xi_{sd2}$	0	0	0	0	0	0	0	0	0	0	0	0	0
$\xi_{\eta 2}$	0	0	0	0	0	0	0	0	0	0	0	0	0
$\eta_{mech}$	0	0	0	0	0	0	0	0	0	0	0	0	0
$v_{dc1}$	0.096	0.004	0.525	0.109	0.311	0.109	0.311	0.003	0.426	0.42	0.003	0.426	0.407
$v_{dc2}$	0.008	0	0.007	0.524	0.137	0.524	0.137	0.045	0.349	0.432	0.045	0.349	0.028
$i_{dc12}$	0.1	0.004	0	0.475	0.428	0.475	0.428	0.044	0.14	0.006	0.044	0.14	0

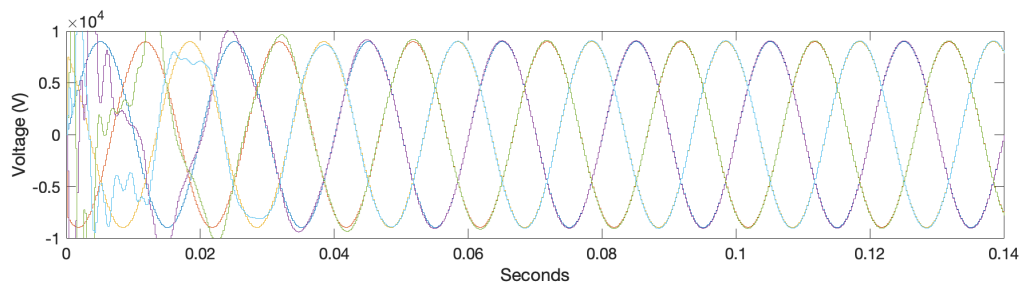
---

**Participation factors related to the bandwidth  $a_{pll}$  of the PLL**

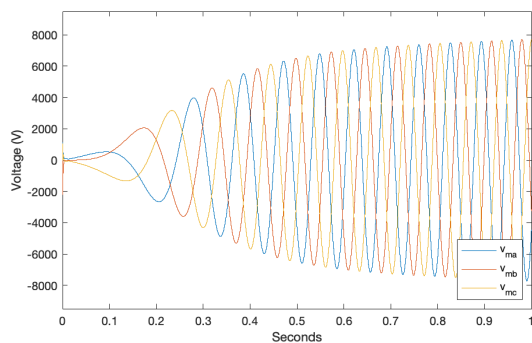
**Table D13:** Participation factors corresponding to bandwidth  $a_{pll} = 12$

	Bandwidth $a_{pll} = 12$	
$i_{d1}$	0.002	0.002
$i_{q1}$	0.088	0.088
$i_{sd}$	0.114	0.114
$i_{sq}$	0.184	0.184
$v_{gd}$	0.141	0.141
$v_{gq}$	0.398	0.398
$\xi_{d1}$	0.002	0.002
$\xi_{q1}$	0.184	0.184
$\xi_v$	0	0
$\xi_{pll}$	0.196	0.196
$\omega_{pll}$	0.225	0.225
$i_{d2}$	0	0
$i_{q2}$	0	0
$\psi_r$	0	0
$\xi_{sp}$	0	0
$\xi_{d2}$	0	0
$\xi_{q2}$	0	0
$n_{mech}$	0	0
$v_{dc1}$	0.007	0.007
$v_{dc2}$	0.001	0.001
$i_{dc12}$	0.008	0.008

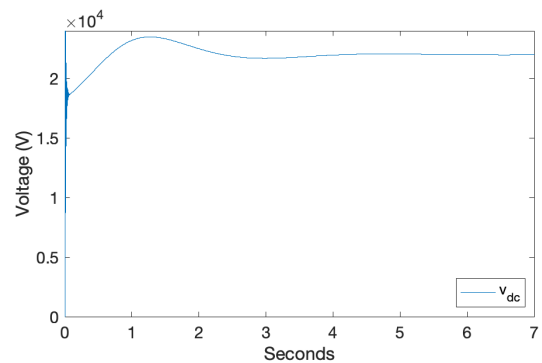
## E Time-domain simulations - Stable conditions



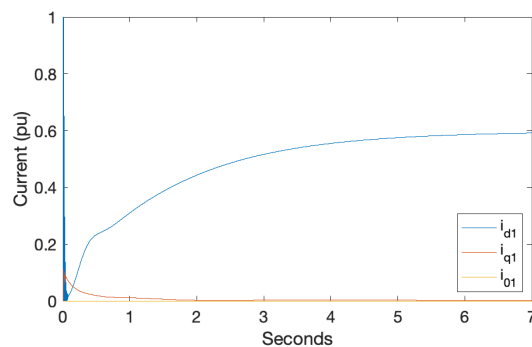
(a) 3-phase voltages of the on-board system



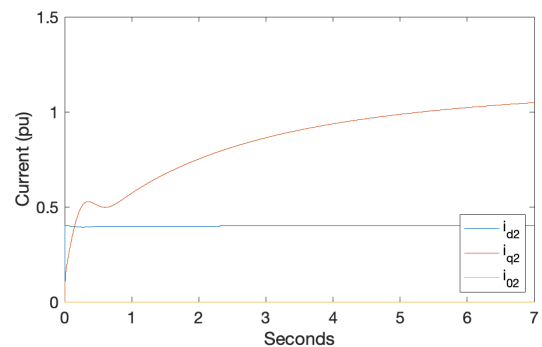
(b) 3-phase voltages of the terminals of the sub-sea system



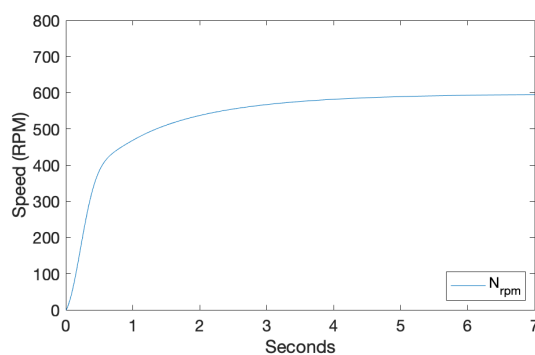
(c) Voltage in dc-link



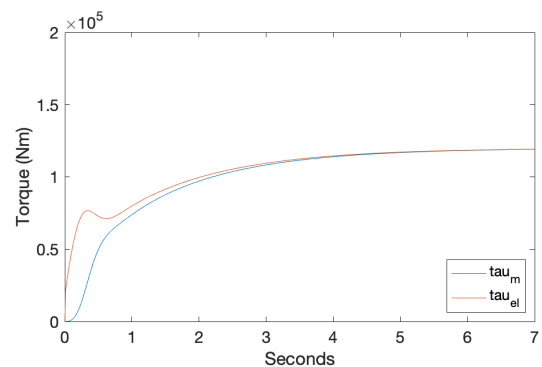
(d) Dq0 current of the on-board system



(e) Dq0 current of the sub-sea system



(f) Speed of the machine



(g) Torque balance in the machine

## F Calculation for cable selection

### Calculation for Cable Selection

#### Loading level P (MW):

- 17 Total installed load
- 12,8 Max contemporary load
- 7,8 Only SSLP

Datashheet voltages (kV):	Currents at diff. loading levels (P\Vdc):					Current limitations (300mm2):			Current limit violation (X=violation):		
	$V_n$ (line-line rms)	$V_{ph}$ (phase rms)	$V_{dc}$	$I$ (17MW) (A)	$I$ (12,8MW) (A)	$I$ (7,8MW) (A)	Current limit ac (from Nexans)	Current limit dc (120% of ac)	17MW	12,8 MW	7,8MW
10	5,77	14,14		1202,08	905,10	636,40	500	600	X	X	X
20	11,55	28,28		601,04	452,55	318,20	495	594	X		
30	17,32	42,43		400,69	301,70	212,13	490	588			

#### Proposed voltages (kV) with 20kV cable :

$V_n$ (line-line rms)	Currents at diff. loading levels (P\Vdc):					Current limitations (300mm2):			Current limit violation (X=violation):		
	$V_{ph}$ (phase rms)	$V_{dc}$	$I$ (17MW) (A)	$I$ (12,8MW) (A)	$I$ (7,8MW) (A)	Current limit ac (from Nexans)	Current limit dc (120% of ac)	17MW	12,8 MW	7,8MW	
11	6,35	15,56		1092,80	822,82	578,54	495	594	X	X	X
12	6,93	16,97		1001,73	754,25	530,33	495	594	X	X	X
13	7,51	18,38		924,68	696,23	489,54	495	594	X	X	X
14	8,08	19,80		858,63	646,50	454,57	495	594	X	X	X
15	8,66	21,21		801,39	603,40	424,26	495	594	X	X	X

#### Voltages on-board system:

$V_n$ (line-line rms) (kV)	$V$ (phase rms) (kV)	$V_{pp}$ (phase pk-pk) (kV)	Modulation index (at 15kV):
			AC/DC ratio ( $V_{pp}/V_{dc}$ )
11	6,35	17,96	0,85

#### Voltages motor system:

$V$ (line-line rms) (kV)	$V_{ph}$ rms (kV)	$V_{pp}$ (phase pk-pk) (kV)	Modulation index (at 15kV):
			AC/DC ratio ( $V_{pp}/V_{dc}$ )
6	3,46	9,80	0,46

# G Data-sheet of power cable (provided by NEXANS)

## 4.6.3 3-phase power cable, 6/10(12)kV, double armour

Conductor X-section [mm <sup>2</sup> ]	16	25	35	50	70	95	120	150	185	240	300
Conductor diameter [mm]	4,8	6,0	7,0	8,2	9,9	11,5	12,9	14,3	16,0	18,4	20,5
Phase diameter [mm]	19,4	20,8	21,2	22,6	24,3	26,1	27,6	29,3	30,9	33,6	36,8
Screen cross sectional area [mm <sup>2</sup> ]	12,7	13,6	13,9	14,9	16,2	17,5	18,7	19,8	21,1	23,1	25,4
Lay up diameter (3xUNIT-P) [mm]	42,6	45,7	46,5	49,5	53,2	57,1	60,3	64	67,4	73,3	80,1
Inner sheath diameter [mm]	46,6	49,7	50,5	53,5	57,2	61,1	64,3	68	71,4	77,3	84,1
Armour steel wires diameter [mm]	2,0/2,0	2,0/2,0	2,5/2,5	2,5/2,5	2,5/2,5	3,15/3,15	3,15/3,15	3,15/3,15	3,15/3,15	4,2/4,2	4,2/4,2
Diameter over armour [mm]	54,6	57,7	60,5	63,5	67,2	73,7	76,9	80,6	84,0	94,1	101,0
Nominal outer diameter [mm]	60,6	63,7	66,5	69,5	73,2	79,7	82,9	86,6	90,0	100,1	107,0
Outer diameter tolerance [mm]	± 2,0	± 2,1	± 2,2	± 2,3	± 2,4	± 2,6	± 2,7	± 2,9	± 3,0	± 3,3	± 3,5
Conductor DC resistance [Ω/km]	1,15	0,727	0,524	0,387	0,268	0,193	0,153	0,124	0,099	0,075	0,06
Screen DC resistance [Ω/km]	1,354	1,265	1,237	1,154	1,062	0,983	0,92	0,869	0,815	0,745	0,677
Armour DC resistance [Ω/km]	0,358	0,339	0,262	0,248	0,234	0,17	0,164	0,155	0,148	0,101	0,094
Max current rating [A]	103	133	161	190	232	276	312	348	390	448	499
Short circuit current for 1s, conductor [kA]	2,5	3,9	5,4	7,6	10,5	14,2	17,8	22,2	27,3	35,3	44
Short circuit current for 1s, screen [kA]	2,0	2,1	2,2	2,3	2,5	2,7	2,9	3,0	3,2	3,5	3,8
Capacitance per phase [μF/km]	0,205	0,231	0,240	0,265	0,302	0,336	0,366	0,396	0,432	0,483	0,527
Dielectrical loss [W/m]	0,009	0,010	0,011	0,012	0,014	0,015	0,017	0,018	0,020	0,022	0,024
Charging current [A/km]	0,39	0,44	0,45	0,50	0,57	0,63	0,69	0,75	0,81	0,91	0,99
AC resistance [Ω/km]	1,46	0,923	0,665	0,492	0,341	0,246	0,195	0,158	0,127	0,097	0,078
Inductance per phase [mH/km]	0,468	0,437	0,410	0,391	0,368	0,353	0,341	0,332	0,320	0,309	0,306
Reactance [Ω/km]	0,147	0,137	0,129	0,123	0,116	0,111	0,107	0,104	0,101	0,097	0,096
Impedance [Ω/km]	1,469+0,147i	0,933+0,137i	0,676+0,129i	0,503+0,123i	0,353+0,116i	0,256+0,111i	0,21+0,107i	0,174+0,104i	0,143+0,101i	0,114+0,097i	0,096+0,096i
Cable weight in air [kg/m]	6,2	6,9	8,4	9,2	10,3	13,5	14,7	16,2	17,8	24,2	27,5
Cable weight in water [kg/m]	3,8	4,2	5,4	5,9	6,7	9,2	10,0	11,0	12,1	17,1	19,3
Min bending diameter [m]	1,6	1,7	1,8	1,9	2,0	2,2	2,3	2,4	2,5	2,8	3,0
Safe handling load [kN]	126	137	178	193	214	294	316	345	374	537	600

CONFIDENTIAL

All rights reserved. Passing on or copying of this document, use and communication of its content are not permitted without prior written authorization from Nexans Norway AS.

#### 4.6.6 3-phase power cable, 12/20(24)kV, double armour

	16	25	35	50	70	95	120	150	185	240	300
Conductor X-section [mm <sup>2</sup> ]	4,8	6,0	7,0	8,2	9,9	11,5	12,9	14,3	16,0	18,4	20,5
Conductor diameter [mm]	23,7	24,9	25,5	26,7	28,6	30,2	31,9	33,4	35,0	37,7	40,9
Phase diameter [mm]	15,7	16,7	17,0	17,9	19,3	20,5	21,7	22,9	24,2	26,1	28,5
Screen cross sectional area [mm <sup>2</sup> ]	51,9	54,5	55,8	58,4	62,5	65,9	69,6	72,8	76,3	82,1	89,0
Lay up diameter (3XUNIT-P) [mm]	55,9	58,5	59,8	62,4	66,5	69,9	73,6	76,8	80,3	86,1	93,0
Inner sheath diameter [mm]	2,5/2,5	2,5/2,5	3,15/3,15	3,15/3,15	3,15/3,15	3,15/3,15	3,15/3,15	4,2/4,2	4,2/4,2	4,2/4,2	4,2/4,2
Armour steel wires diameter [mm]	65,9	68,5	72,4	75,0	79,1	82,5	86,2	93,6	97,1	102,9	109,8
Diameter over armour [mm]	71,9	74,5	78,4	81,0	85,1	88,5	92,2	99,6	103,1	108,9	115,8
Nominal outer diameter [mm]	± 2,4	± 2,5	± 2,6	± 2,7	± 2,8	± 2,9	± 3	± 3,3	± 3,4	± 3,6	± 3,8
Outer diameter tolerance [mm]	1,15	0,727	0,524	0,387	0,268	0,193	0,153	0,124	0,099	0,075	0,06
Conductor DC resistance [Ω/km]	1,096	1,03	1,012	0,981	0,891	0,839	0,793	0,751	0,711	0,659	0,604
Screen DC resistance [Ω/km]	0,239	0,229	0,175	0,168	0,159	0,152	0,144	0,102	0,097	0,091	0,085
Armour DC resistance [Ω/km]	100	130	157	186	229	273	308	346	388	444	495
Max current rating [A]	2,5	3,9	5,4	7,6	10,5	14,2	17,8	22,2	27,3	35,3	44,0
Short circuit current for 1s, conductor [kA]	2,5	2,7	2,7	2,8	3,0	3,2	3,3	3,5	3,7	4,0	4,3
Short circuit current for 1s, screen [kA]	0,149	0,166	0,171	0,188	0,211	0,233	0,252	0,271	0,294	0,326	0,355
Capacitance per phase [μF/km]	0,027	0,03	0,031	0,034	0,038	0,042	0,046	0,049	0,053	0,059	0,064
Dielectrical loss [W/m]	0,56	0,62	0,65	0,71	0,8	0,88	0,95	1,02	1,11	1,23	1,34
Charging current [A/km]	1,46	0,923	0,665	0,492	0,341	0,246	0,195	0,158	0,127	0,097	0,078
AC resistance [Ω/km]	0,508	0,473	0,447	0,425	0,401	0,382	0,37	0,358	0,345	0,332	0,327
Inductance per phase [mH/km]	0,16	0,149	0,14	0,133	0,126	0,12	0,116	0,113	0,108	0,104	0,103
Reactance [Ω/km]	1,472±0,16i	0,936±0,149i	0,679±0,14i	0,506±0,133i	0,356±0,126i	0,261±0,12i	0,211±0,116i	0,175±0,113i	0,144±0,108i	0,115±0,104i	0,096±0,103i
Impedance [Ω/km]	8,9	9,6	11,8	12,7	14	15,4	16,8	21,9	23,7	26,7	30,1
Cable weight in air [kg/m]	5,4	5,8	7,6	8,1	9	9,9	10,8	14,8	16,1	18,2	20,4
Cable weight in water [kg/m]	2	2,1	2,2	2,3	2,4	2,5	2,6	2,8	2,9	3,1	3,3
Min bending diameter [m]	184	197	259	275	300	325	351	488	523	581	643
Safe handling load [kN]											

CONFIDENTIAL.  
 All rights reserved. Passing on or copying of this document, use and communication of its content are not permitted without prior written authorization from Nexans Norway AS.

#### 4.6.8 3-phase power cable, 18/30(36)kV, double armour

Conductor X-section [mm <sup>2</sup> ]	50	70	95	120	150	185	240	300
Conductor diameter [mm]	8,2	9,9	11,5	12,9	14,3	16,0	18,4	20,5
Phase diameter [mm]	31,8	33,5	35,3	36,8	38,5	40,1	42,8	46,0
Screen cross sectional area [mm <sup>2</sup> ]	21,6	23,0	24,2	25,4	26,6	27,8	29,8	32,2
Lay up diameter (3XUNIT-P) [mm]	69,4	73	76,9	80,1	83,8	87,3	93,1	100
Inner sheath diameter [mm]	73,4	77	80,9	84,1	87,8	91,3	97,1	104
Armour steel wires diameter [mm]	3,15/3,15	4,2/4,2	4,2/4,2	4,2/4,2	4,2/4,2	4,2/4,2	4,2/4,2	4,2/4,2
Diameter over armour [mm]	86,0	93,8	97,7	101,0	104,6	108,1	113,9	120,8
Nominal outer diameter [mm]	92,0	99,8	103,7	107,0	110,6	114,1	119,9	126,8
Outer diameter tolerance [mm]	± 3,0	± 3,3	± 3,4	± 3,5	± 3,6	± 3,8	± 4,0	± 4,2
Conductor DC resistance [Ω/km]	0,387	0,288	0,193	0,153	0,124	0,099	0,075	0,060
Screen DC resistance [Ω/km]	0,796	0,748	0,711	0,677	0,647	0,619	0,577	0,534
Armour DC resistance [Ω/km]	0,144	0,101	0,097	0,094	0,090	0,087	0,082	0,077
Max current rating [A]	182	224	269	305	341	383	439	490
Short circuit current for 1s, conductor [kA]	7,6	10,5	14,2	17,8	22,2	27,3	35,3	44
Short circuit current for 1s, screen [kA]	3,4	3,6	3,8	4,0	4,1	4,3	4,6	4,9
Capacitance per phase [μF/km]	0,146	0,163	0,178	0,192	0,205	0,221	0,244	0,263
Dielectrical loss [W/m]	0,060	0,066	0,073	0,078	0,084	0,090	0,099	0,107
Charging current [A/km]	0,83	0,92	1,01	1,08	1,16	1,25	1,38	1,49
AC resistance [Ω/km]	0,492	0,341	0,246	0,195	0,158	0,127	0,097	0,078
Inductance per phase [mH/km]	0,460	0,432	0,413	0,398	0,387	0,372	0,357	0,350
Reactance [Ω/km]	0,144	0,136	0,130	0,125	0,121	0,117	0,112	0,110
Impedance [Ω/km]	0,508+0,144i	0,357+0,136i	0,262+0,13i	0,212+0,125i	0,176+0,121i	0,145+0,117i	0,115+0,112i	0,097+0,11i
Cable weight in air [kg/m]	15,1	20,2	21,8	23,3	24,9	26,8	29,8	33,4
Cable weight in water [kg/m]	9,1	13,1	14,2	15,0	16,1	17,4	19,4	21,6
Min bending diameter [m]	2,6	2,8	2,9	3,0	3,1	3,2	3,4	3,6
Safe handling load [kN]	316	452	483	510	542	577	631	697

All rights reserved. Passing on or copying of this document, use and communication of its content are not permitted without prior written authorization from Nexans Norway AS.

CONFIDENTIAL.

## H Data-sheet of induction machine (provided by ABB)

Customer: ABB  
 Project: 9MW motor  
 Your Ref:  
 Our Ref: 9MW motor



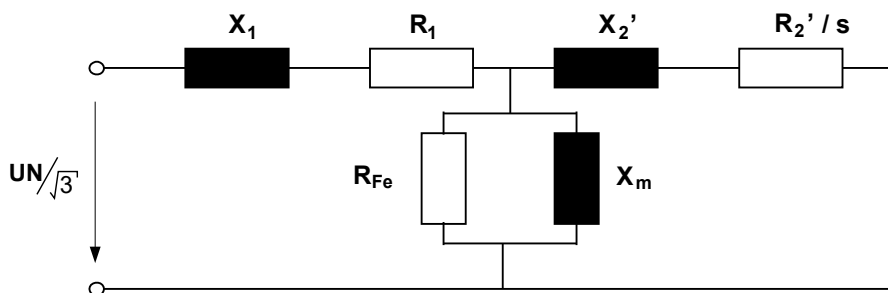
PRELIMINARY DATA OF MACHINE  
 Saving Ident : []  
 Page: 5(5)

Motor type code: AMI 800M4W BSV

Rated output	9000 kW	Power Factor	0,92
Voltage	6000 V $\pm 5$ %	Rated torque	57607 Nm
Frequency	50 Hz	Relat. starting current	4,3
Speed	1492 rpm	Relat. starting torque	0,29
Current	969 A	Relat. maximum torque	2,0

Equivalent circuit between phase and neutral (equivalent star)

Running		Rotor resistance $R_2'$ (95 °C)		0,01866 $\Omega$
Stator resistance $R_1$ (95 °C)	0,01887 $\Omega$	Rotor reactance $X_2'$	0,3748 $\Omega$	
Stator reactance $X_1$	0,6271 $\Omega$	Iron loss resistance $R_{Fe}$	1,18 k $\Omega$	
Magnetizing reactance $X_m$	24,82 $\Omega$			
Starting		Rotor resistance $R_2'$ (95 °C)		0,05235 $\Omega$
Stator resistance $R_1$ (95 °C)	0,01887 $\Omega$	Rotor reactance $X_2'$	0,2601 $\Omega$	
Stator reactance $X_1$	0,5779 $\Omega$			
Ambient condition		Rotor resistance $R_2'$ (40 °C)		0,04366 $\Omega$
Stator resistance $R_1$ (40 °C)	0,01568 $\Omega$			



Doc. kind	Technical Specification	Project	9MW motor		
Title	Technical Specification Induction Motor	Customer	ABB		
		Proj. no.			
	ABB AB	Doc. no.	3BSY200001-1	Lang.	en
		Rev. ind.	-	Page	5
				No. of p.	5



---

## I Modelling specific notes

This section has the intention of providing the necessary explanations and details to replicate the simulations performed with the SIMULINK model.

### SIMULINK - Additional components

In order to make the SIMULINK model work properly, some additional components have to be included. At the terminals of the squirrel cage machine, a series impedance and a parallel capacitor have been added. This is a measure to satisfy the solver, unless it will not run. The additional components are however made sure to be of a very small scale, which means their impact on the system dynamics is practically negligible. This has also been verified by measuring the voltage drop over the components. The parameters used for the additional components are given in table I1.

**Table I1:** Parameters of additional components

<b>Component:</b>	<b>Value:</b>
$R_f$	1 n $\Omega$
$L_f$	1 $\mu H$
$C_f$	1 nF

### SIMULINK - Initial conditions

During the start-up of the model, there is an issue with dividing zero-division. In order to overcome this issue an initial condition in the rotor flux is required. As the start up response is not of great interest, the initial rotor flux is selected to match the steady state operation. Thus, the initial rotor flux is set to be 2.45 pu.

### SIMULINK - Speed-voltage relationship

In order to match the rated voltage of the squirrel cage machine, the rated speed has to be divided by 2.5. Hence, there might be an issue with the relationship between the speed and the voltage of the machine. Since this is a mechanical issue, this issue is disregarded in the system analysis.

---

## Linearized model - operating point

**Table I2:** Operating point of linearized model

Variable:	Value:
$i_{d10}$	0.8
$i_{q10}$	0
$v_{gd0}$	1
$v_{gd0}$	0
$\omega_{os0}$	1
$v_{dc10}$	1
$v_{dc20}$	1
$i_{dc120}$	0.8
$i_{d20}$	0.7
$i_{q20}$	0.4
$\psi_{r0}$	2.5
$\omega_{ss0}$	1
$\xi_{d10}$	0
$\xi_{q10}$	0
$\xi_{d20}$	0
$\xi_{q20}$	0
$\xi_v$	0
$\xi_{sp}$	0
$v_{dc,ref}$	1
$Q_{ref}$	0
$n_{ref}$	1492
$i_{\psi_r,ref}$	0.4

